

Understanding phase transitions in carbonates by investigation of their lattice dynamics

Dissertation
zur Erlangung des Doktorgrades
der Naturwissenschaften

vorgelegt beim Fachbereich Geowissenschaften/Geographie
der Johann Wolfgang Goethe-Universität
Frankfurt am Main

von
Michał Stekiel
aus Warschau, Polen

Frankfurt 2019
(D30)

vom Fachbereich Geowissenschaften/Geographie der
Johann Wolfgang Goethe-Universität als Dissertation angenommen.

Dekan: Prof. Dr. Georg Rumpker

1. Gutachter: Prof. Dr. Björn Winkler
2. Gutachter: Dr. Alexei Bosak

Datum der Disputation: ???.?.2019

Contents

Zusammenfassung	V
Summary of the thesis	XI
Abbreviations	XV
1 Introduction	1
1.1 Why carbonates?	1
1.2 Why phase transitions?	2
1.3 Lattice dynamics	3
1.4 Scope of the thesis	4
2 Lattice dynamics, formalism and methods	5
2.1 Mathematical formalism of lattice dynamics	5
2.2 Methods for determining the lattice dynamics	8
2.2.1 Inelastic x-ray scattering	9
2.2.2 Thermal diffuse scattering	11
2.2.3 Density functional theory based calculations	14
2.3 Linear elasticity	15
3 High pressure elastic properties of (Mg,Fe)CO₃ carbonates	19
3.1 Introduction	20
3.2 Experimental methods	24
3.3 Computational details	25
3.4 High-pressure elasticity of FeCO ₃ and MgCO ₃ from experiment and calculations	26
3.5 High pressure elasticity of Mg _{1-x} Fe _x CO ₃	29
3.6 Geophysical implications	31
3.6.1 Effect of the spin transition on the detectability of Mg _{1-x} Fe _x CO ₃ in the mantle	32

3.6.2	Effect of the presence of $\text{Mg}_{1-x}\text{Fe}_x\text{CO}_3$ on the velocity profile of the mantle	33
3.6.3	Velocity anisotropies of $\text{Mg}_{1-x}\text{Fe}_x\text{CO}_3$	34
3.7	Conclusions	36
4	High-pressure F-point instabilities in carbonates	37
4.1	Introduction	38
4.2	Summary of the experimental methods	40
4.3	TDS and IXS measurements on carbonates at ambient conditions	43
4.4	Phonon-driven transitions to calcite-II and dolomite-II	47
4.5	F -point phonons in other carbonates	50
4.6	Crystal chemistry of the transition to the calcite-II structure	53
4.7	Conclusions	55
5	Phonon coupling to the high-temperature rotational disorder in calcite	57
5.1	Introduction	58
5.2	Diamond chamber sample environment	60
5.3	Sample preparation	63
5.4	Experimental details	63
5.5	Mapping the reciprocal space by thermal diffuse scattering	64
5.6	Anharmonicity of the Γ - F branch from inelastic x-ray scattering	66
5.7	Origin of the high temperature anharmonicity in calcite	69
5.8	Comparison of the CO_3 reorientation in calcite with other systems	75
5.9	Conclusions	77
6	Summary and outlook	79
A	Source code for determining the elastic tensor of $(\text{Mg,Fe})\text{CO}_3$	83
B	Dispersion relations of calcite, dolomite, and magnesite	87
C	Modeling the damping parameter for the high-temperature IXS data	93
	Bibliography	95
	List of Figures	107
	List of Tables	111
	Publications	113
	Acknowledgements	115

Zusammenfassung

Zum Verständnis von Phasenumwandlungen in Carbonaten durch Untersuchungen ihrer Gitterdynamik

In letzter Zeit haben Carbonate aufgrund der Entdeckung ihrer Bedeutung für den globalen Kohlenstoffkreislauf viel Aufmerksamkeit auf sich gezogen. Diese Entdeckung wurde durch Verbesserungen der experimentellen Techniken ermöglicht, die es erlauben, die Stabilität, Struktur und physikalischen Eigenschaften von Materialien unter hohem Druck und hohen Temperaturen zu untersuchen, d. h. Mineralien und geochemische Prozesse können unter den tief im Erdinneren auftretenden Bedingungen untersucht werden.

Obwohl sich viele Untersuchungen auf Carbonate bezogen haben, gibt es noch offene Fragen zu ihrer Struktur und ihren physikalischen Eigenschaften unter solch extremen Bedingungen. Das Ziel dieser Arbeit ist es, ein tieferes Verständnis der Natur von Phasenübergängen in Carbonaten zu erlangen, indem untersucht wird, wie die Atome, die die Kristallstruktur aufbauen, vibrieren, d. h. ihre Gitterdynamik. Die in dieser Studie verwendete Methodik ist eine Kombination von experimentellen und rechnerischen Methoden, was eine sehr gründliche Untersuchung des Problems ermöglicht. Einerseits ermöglichen die gemessenen Ergebnisse eine Evaluation der Modellrechnungen, andererseits liefert der rechnerische Ansatz Werte für Parameter, deren Messung schwierig oder langwierig ist.

Der Kohlenstoffkreislauf der Erde kann in einen Oberflächenzyklus und einen "tiefen Zyklus" unterteilt werden. Der Oberflächenzyklus bezieht sich auf die Atmosphäre, Ozeane und flache Krustenumgebungen, während der tiefe Kohlenstoffzyklus die Erde bis hinab zum äußeren Kern betrachtet, wo die typischen Prozesse auf geologischen Zeitskalen ablaufen, z. B. in Hunderttausenden oder Millionen von Jahren. Es ist nur wenig über die Menge und die Transportmechanik von Kohlenstoff in der Erde bekannt, da es unmöglich ist, Proben aus solchen Tie-

fen zu entnehmen und wir die Dynamik dieser Prozesse nicht direkt überwachen können.

Tatsächlich stammt der größte Teil unseres Wissens aus Rechenmodellen, die durch die Kenntnis der Zusammensetzung des Erdinneren und der physikalischen Eigenschaften der Mineralien unter gegebenen Bedingungen eingeschränkt sind. Für Kohlenstoff wurden von der geowissenschaftlichen Gemeinschaft zwei Hauptfragen aufgeworfen. Ist der tiefe Kohlenstoffkreislauf ausgeglichen? Und: in welcher Form wird der Kohlenstoff im Erdinneren transportiert und gespeichert? Für die zweite Frage kann eine genauere Antwort gegeben werden. Eine ganze Reihe möglicher kohlenstoffenthaltender Verbindungen kann auf die Bedingungen der jeweiligen Tiefe der Erde gebracht und ihre Stabilität getestet werden. Wenn sich eine bestimmte Verbindung zersetzt, wird das kohlenstoffhaltige Zerstellungsprodukt als der wahrscheinlichere Kandidat ausgewählt.

Solche Versuche haben gezeigt, dass elementarer Kohlenstoff in Form von Diamant und Carbonaten die stabilsten kohlenstoffenthaltenden Verbindungen sind. Um die Frage nach dem Gleichgewicht des Kohlenstoffkreislaufs zu beantworten, haben Wissenschaftler versucht, die Kohlenstoffflüsse zu schätzen, die zum oder vom Erdinneren transportiert werden. Der Hauptweg des Kohlenstofftransports ins Innere — der als positiver Fluss betrachtet wird — ist die Subduktion von kohlenstoffreichen ozeanischen Sedimenten aus organischen Stoffen, während die Prozesse, die Kohlenstoff an die Oberfläche transportieren und den negativen Fluss darstellen, Vulkanausbrüche und Ausgasungen vom Festland und ozeanischen Rücken sind.

Somit sind drei Szenarien möglich: entweder der Gesamtfluss ist negativ, positiv oder nahe Null. In der geowissenschaftlichen Gemeinschaft herrscht Einigkeit darüber, dass das erste Szenario unwahrscheinlich ist, sodass entweder mehr Kohlenstoff ins Erdinnere transportiert wird oder der Zyklus im Gleichgewicht ist. Durch den Vergleich der durchschnittlichen Zusammensetzung der Erdkruste mit Meteoriten wissen wir außerdem, dass das Erdinnere viel mehr Kohlenstoff enthält als die Erdoberfläche. Zusammenfassend lässt sich festhalten, dass im Erdinneren ein riesiger Kohlenstoffspeicher in Form von Karbonatmineral vorliegt, der uns zur Durchführung der aktuellen Studie motiviert hat.

Wir haben beschlossen, uns auf die Untersuchung der Gitterdynamik von Carbonaten bei hohen Drücken und Temperaturen zu konzentrieren, da diese umfassende Erkenntnisse über die physikalischen Eigenschaften des untersuchten Systems liefert. Sie ermöglicht die Bestimmung der atomaren Schwingungen, die wiederum Informationen über die strukturellen, elastischen und thermodynamischen Eigenschaften der Probe liefern. Diese ermöglichen, z. B. die Schallgeschwindigkeiten der Probe, die Wärmekapazität und die mögliche Struktur

ihrer Hochdruckpolymorphe zu bestimmen. Wie bereits erwähnt, können die Experimente jedoch nur eine kleine Anzahl von Parametern ermitteln, die die Gitterdynamik bestimmen. Es ist die Kombination aus experimentellem und rechnerischem Ansatz, mit dem die vollständige Gitterdynamik und alle interessanten physikalischen Eigenschaften identifiziert werden können.

Die erste in der Arbeit vorgestellte Studie zielt direkt auf die Bestimmung der physikalischen Eigenschaften der Carbonate im Erdmantel ab. Die einzigen direkten Informationen, die wir über den Zustand des Erdinneren erhalten, stammen derzeit aus der Messung der Geschwindigkeit der seismischen Wellen. Aus diesem Grund wird viel Aufwand betrieben, um die Schallgeschwindigkeiten von Mineralien bei hohen Drücken und Temperaturen zu bestimmen.

Alle elastischen Eigenschaften eines Kristalls können aus dem elastischen Tensor abgeleitet werden, der je nach Symmetrie des Kristalls aus drei bis einundzwanzig unabhängigen Parametern besteht. Zu diesen Eigenschaften gehören die Schallgeschwindigkeiten. Wenige Studien weisen darauf hin, dass die wahrscheinlichste Zusammensetzung des Carbonats des unteren Mantels $\text{Mg}_{0.85}\text{Fe}_{0.15}\text{CO}_3$ ist, da CaCO_3 , das an der Erdoberfläche am häufigsten vorkommende Carbonat, mit eisenreichen Silikaten reagiert. Außerdem zeigt FeCO_3 bei 45 GPa einen Phasenübergang, was mit der Änderung der elektronischen Struktur des Fe-Kation und der Verringerung der Dichte von FeCO_3 oberhalb des Übergangs zusammenhängt.

Es war von besonderem Interesse festzustellen, wie sich dieser Übergang auf die elastischen Eigenschaften von FeCO_3 auswirkt. Die Elastizitätsmodule C_{33} und C_{44} von FeCO_3 wurden durch inelastische Röntgenstreuung bis zu 55 GPa bestimmt und mit DFT-basierten Berechnungen ergänzt, die es uns ermöglichten, den vollständigen elastischen Tensor von FeCO_3 bis zu 60 GPa zu bestimmen. Es wurde gezeigt, dass die C_{33} - und C_{44} -Module linear mit dem Druck ansteigen und abrupt am Phasenübergang bei 45 GPa ansteigen.

Zusätzliche Berechnungen wurden für MgCO_3 durchgeführt, die mit zuvor veröffentlichten experimentellen Daten verglichen wurden, aus denen geschlossen wurde, dass C_{33} , C_{12} und C_{13} linear mit dem Druck bis 60 GPa ansteigen, während sich C_{11} , C_{44} und C_{14} oberhalb 20 GPa nicht linear verhalten. Diese beiden Datensätze wurden mit den veröffentlichten Daten zu $\text{Mg}_{0.35}\text{Fe}_{0.65}\text{CO}_3$ kombiniert, um die elastischen Eigenschaften von $\text{Mg}_{1-x}\text{Fe}_x\text{CO}_3$ Carbonat für jede Zusammensetzung x bis zu Drücken von 60 GPa zu interpolieren. Es konnte gezeigt werden, dass die Schallgeschwindigkeiten im untersuchten Druckbereich mit zunehmendem Fe-Gehalt abnehmen. Es wurde auch gezeigt, dass die Geschwindigkeitsanisotropie von $\text{Mg}_{1-x}\text{Fe}_x\text{CO}_3$ sehr hoch ist. Die Studie schloss in einer Diskussion über die Möglichkeit des Nachweises von Carbonat im tiefen Mantel und zeigte, dass nur Regionen mit hoher Carbonatkonzentration einen signifikan-

ten Geschwindigkeitskontrast liefern können, der den Nachweis mit aktuellen Methoden ermöglichen würde.

Das nächste Kapitel beschreibt die Hochdruckgitterdynamik von Calcit, CaCO_3 und Dolomit, $\text{CaMg}(\text{CO}_3)_2$, sowie den Zusammenhang mit den Übergängen zu Calcit-II bei 1.8 GPa und Dolomit-II bei 17 GPa. Die $(\text{Ca},\text{Mg})\text{CO}_3$ -Familie von Carbonaten weist eine Mischungslücke bei Umgebungsbedingungen auf, d. h. die einzigen stabilen (Ca,Mg) -Carbonate sind CaCO_3 , $\text{CaMg}(\text{CO}_3)_2$ und MgCO_3 .

Calcit und Magnesit, MgCO_3 , sind isostrukturell und Mg und Ca sind relativ ähnliche Kationen, jedoch unterscheiden sich die Phasendiagramme von Calcit und Magnesit bei hohen Drücken und Temperaturen drastisch. Das Ziel dieser Studie war es, ein tieferes Verständnis des Mechanismus der Phasenübergänge in Calcit zu erlangen, indem die Gitterdynamik untersucht und mit Magnesit verglichen wurde, um den Ursprung seines breiten Stabilitätsbereichs zu verstehen und möglicherweise die bislang unbekannte Magnesit-II Hochdruckphase aufzuklären.

Frühere Berichte weisen auf die Ähnlichkeit der Kristallstrukturen von Calcit-II und Dolomit-II hin und schlugen einen ähnlichen Mechanismus vor, der diese Übergänge antreibt. Tatsächlich wurde durch inelastische Röntgenstreuungsmessungen in Diamantstempelzellen gezeigt, dass der Übergang zur Calcit-II-Phase mit der Frequenzerniedrigung eines transversalen Phonons am F -Punkt der Brillouinzone zusammenhängt, dessen Energie bei 1.8 GPa auf Null abfällt. Eine weitere DFT-basierte Berechnung zeigte, dass dieses Phonon tatsächlich den Übergang zur metastabilen Calcit-II-Phase vorantreibt.

Das transversale F -Punkt-Phonon wurde ebenfalls in Dolomit gemessen und es wurde erneut der Schluss gezogen, dass es den Phasenübergang zur Dolomit-II-Phase treibt. Diese Ergebnisse wurden durch weitere Messungen der thermischen diffusen Streuung und inelastischen Röntgenstreuung an MgCO_3 , FeCO_3 und ZnCO_3 ergänzt, die es ermöglichten, den Einfluss des Kations X in $X\text{CO}_3$ mit ihrer Gitterdynamik zu korrelieren. Es wurde gezeigt, dass die Energie des transversalen, akustischen F -Punkt-Phonons mit zunehmendem Ionenradius von X abnimmt, und obwohl der Übergang zur Carbonat-II-Phase in CaCO_3 und $\text{CaMg}(\text{CO}_3)_2$ stattfindet, dieser nicht in MgCO_3 , FeCO_3 oder ZnCO_3 auftritt.

Das letzte Kapitel zeigt die Hochtemperaturstudie zum Einfluss der Rotationsunordnung in Calcit auf seine Gitterdynamik. Die Kristallstruktur von Calcit kann durch ionisch gebundene Ca^{2+} -Kationen und starre CO_3^{2-} -Gruppen beschrieben werden. Beim Erhitzen geht Calcit bei 985 K in Calcit-IV über, wo sich eine signifikante Menge von CO_3^{2-} -Gruppen um 60° zu einer alternativen Orientierung drehen kann, wodurch Unordnung in den Kristall eingeführt wird. Beim

weiteren Erhitzen wandelt sich Calcit-IV bei 1240 K in Calcit-V um, wo sich die CO_3^{2-} -Gruppen frei drehen.

Die experimentellen Untersuchungen der Calcit-IV- und Calcit-V-Phasen sind äußerst schwierig, da sich Calcit bei 870 K zu CaO und extrem reaktivem CO_2 zersetzt. Zunächst wurden Messungen der thermischen diffusen Streuung bis 870 K durchgeführt, die eine Zunahme der Intensität der diffusen Streuung am F -Punkt zeigten. Es wurde ursprünglich als die Erweichung des F -Punkt Phonons interpretiert, das für den im vorherigen Kapitel beschriebenen Hochdruckübergang in die Calcit-II-Phase verantwortlich ist. Zur Messung der Calcit-IV-Phase bei hohen Temperaturen wurde eine speziell angefertigte Diamant-Probenkammer und Probenumgebung verwendet.

Dabei wurde die Calcitprobe mit MgCO_3 -Pulver in einem Einkristalldiamanten eingeschlossen, der zwischen zwei Wolframheizungen gespannt wurde. Das MgCO_3 -Pulver zersetzt sich bei 670 K unter Bildung von CO_2 -Gas, das in der geschlossenen Kammer unter mäßigem Druck steht, wodurch die Zersetzung des CaCO_3 -Einkristalls verhindert wird. Die Diamantkammer wird in einem Vakuumgefäß betrieben, was die Graphitisierung der Diamanten bei hohen Temperaturen verhindert. Es wurde eine inelastische Röntgenstreuung durchgeführt, die ein anharmonisches Verhalten des F -Punkt-Phonons zeigte. Es wurde als die Dämpfung des Phonons durch die Rotation der CO_3 -Gruppen interpretiert. Durch Quantifizierung der Erweichung und der Verbreiterung der IXS-Spektren wurde die Zeitskala der Neuorientierung bestimmt. Es wurde gezeigt, dass sich die CO_3 -Gruppen bei 1000 K durchschnittlich alle 7 ps neu orientieren, während sie sich bei 1200 K — näher am Übergang zur Calcit-V-Phase — durchschnittlich alle 0.4 ps neu orientieren. In der Calcit-V-Phase ist die Neuorientierung schneller als 0.1 ps, d. h. die CO_3 -Gruppen rotieren schneller als 10 THz.

Zusammenfassend werden in dieser Dissertation Studien vorgestellt, die verschiedene Aspekte der Gitterdynamik und den Zusammenhang mit den Phasenübergängen in ausgewählten Carbonaten untersuchen. Geowissenschaftlich signifikante Ca-, Mg-, Fe- und Zn-Carbonate wurden durch Kombination von inelastischer Röntgenstreuung, thermischer diffuser Streuung sowie zusätzlicher Raman-Streuung und Wärmekapazitätsmessungen bei verschiedenen Drücken und Temperaturen untersucht und die Experimente wurden durch DFT-basierte Berechnungen ergänzt. Dies ermöglichte es, die Struktur, Stabilität und physikalischen Eigenschaften dieser Carbonate unter den Bedingungen der tiefen Erde zu bestimmen, was das Wissen über den tiefen Kohlenstoffkreislauf erweitert und das Vertrauen in die Existenz von Carbonaten im Mantel stärkt.

Summary of the thesis

Recently, carbonates have attracted a lot of attention, due to the recognition of their importance in the global carbon cycle. This was enabled by improvement of the experimental techniques that allow for investigating the stability, structure, and physical properties of materials and high-pressures and high-temperatures, that is, they allow for investigating minerals and geochemical processes at the conditions occurring deep inside Earth. Although a lot of research has been focused on carbonates, there are still some open questions regarding their structure and physical properties at such extreme conditions. The aim of this thesis is to establish a deeper understanding of the nature of the phase transitions in carbonates by studying how do the atoms building up the crystal structure vibrate, that is lattice dynamics. The methodology adapted in this study is a combination of experimental and computational methods which allows for a very thorough examination of the problem. The computational approach allows to determine parameters that are elusive or tedious to measure, and the experimental results provide a solid benchmark for the calculations. This tandem of methods has been widely used for investigating lattice dynamics of various materials. In this study it was used to elucidate the structure and properties of carbonates in the deep Earth conditions.

The first study presented in the thesis aims directly at determining physical properties of the carbonates in the Earth's mantle. As for now, the only direct information that we get about the state of the Earth's interior comes from the measurements of velocities of the seismic waves. This is why a lot of effort is put to determine the sound velocities of minerals at high-pressures and high-temperatures. The theory of linear elasticity shows, that all elastic properties of a crystal can be derived from the elastic tensor, which consist of three to twenty one independent coefficients, depending on the symmetry of the crystal. Among these properties are sound velocities. The remaining question is about the composition of the mantle carbonate. Few studies pointed out, that the most probable composition of the lower mantle carbonate is $\text{Mg}_{0.85}\text{Fe}_{0.15}\text{CO}_3$, where the Fe content can strongly vary with depth. In addition FeCO_3 undergoes a phase transition at 45 GPa, which

is connected to the change in the electronic structure of the Fe^{2+} cation and decrease in density of FeCO_3 across the transition. It was of particular interest to determine how this transition affects the elastic properties of FeCO_3 . The C_{33} and C_{44} elastic moduli of FeCO_3 were determined by inelastic x-ray scattering up to 55 GPa, while DFT based calculations allowed to determine the full elastic tensor of FeCO_3 up to 60 GPa. It was shown, that the C_{33} and C_{44} moduli increase linearly with pressure, and increase abruptly across the transition at 45 GPa. Additional calculations were performed for MgCO_3 benchmarked with experimental data reported beforehand. These two datasets were combined with the data reported for $\text{Mg}_{0.35}\text{Fe}_{0.65}\text{CO}_3$ in order to interpolate the elastic properties of $\text{Mg}_{1-x}\text{Fe}_x\text{CO}_3$ carbonate for any composition x , up to pressures of 60 GPa. It was shown that the sound velocities decrease with increasing Fe content in the investigated pressure range. It was also shown that the velocity anisotropy of the $\text{Mg}_{1-x}\text{Fe}_x\text{CO}_3$ is relatively high, for all compositions. A discussion on the possibility of the detection of carbonate in the deep mantle showed, that only a region with high concentration of a Mg-Fe carbonate could provide a significant contrast in velocity, that would allow for their detection with current methods.

Next chapter presents the study of the high-pressure lattice dynamics of calcite, CaCO_3 , and dolomite, $\text{CaMg}(\text{CO}_3)_2$, to understand the mechanism of transitions to calcite-II at 1.8 GPa and dolomite-II at 17 GPa. The study was extended to magnesite, MgCO_3 , in order to provide a broader picture of lattice dynamics of $(\text{Ca},\text{Mg})\text{CO}_3$ family of carbonates. Previous reports pointed out the similarity in the crystal structure of calcite-II and dolomite-II and suggested a similar mechanism driving these two transitions. Indeed, by means of inelastic x-ray scattering measurements in diamond-anvil cells, it was shown that the transition to calcite-II phase is connected to the softening of a transverse F -point phonon, which energy decreases to zero at 1.8 GPa. Complementary DFT based calculation showed, that this phonon actually drives the transition to the metastable calcite-II phase, as its eigenvector is the same as the displacement of the atoms upon the transition. The transverse F -point phonon was also measured in dolomite, and on the same basis as for calcite it was concluded, that it drives the phase transition to the dolomite-II phase. These results were complimented with further thermal diffuse scattering and inelastic x-ray scattering measurements on MgCO_3 , FeCO_3 , and ZnCO_3 , which allowed to correlate the influence of the cation X in $X\text{CO}_3$, with their lattice dynamics. It was shown that the energy of the transverse, acoustic F -point phonon decreases with increasing ionic radius of X , and, although the transition to carbonate-II phase occurs in CaCO_3 , $\text{CaMg}(\text{CO}_3)_2$ and possibly in CdCO_3 , it does not occur in MgCO_3 , FeCO_3 , or ZnCO_3 .

The last chapter shows the high-temperature study on the influence of the rotational disorder in calcite on its lattice dynamics. Crystal structure of calcite can be described by ionically bonded Ca^{2+} cations and rigid CO_3^{2-} groups. Upon heating calcite undergoes a transition to calcite-IV at 985 K, where the significant amount of CO_3 groups can rotate by 60° to an alternative orientation, introducing a disorder in the crystal. Upon further heating, at 1240 K calcite-IV transforms to calcite-V, where the CO_3 groups rotate freely. The experimental investigations of calcite-IV and calcite-V phases are extremely hard, as at 870 K calcite decomposes to CaO and extremely reactive CO_2 . First, the thermal diffuse scattering measurements were performed up to 870 K, which showed an increase in the intensity of the diffuse scattering at the F -points. It was initially interpreted as the softening of the F -point phonon, the same one that is responsible for the high-pressure transition to the calcite-II phase, described in the previous chapter. In order to conduct an inelastic x-ray scattering measurements of the calcite-IV phase at high temperatures, a custom-made diamond chamber and sample environment were used. The sample of calcite was enclosed with the MgCO_3 powder in a single crystal diamond, that was enclosed between two tungsten heaters. The MgCO_3 powder decomposes at 670 K producing CO_2 gas that is under moderate pressure in the closed chamber, which prevents the decomposition of the single crystal of CaCO_3 . The diamond chamber is enclosed in a vacuum, that prevents the graphitization of the diamond at high temperatures. The inelastic x-ray scattering measurements showed an anharmonic behavior of the F -point phonon. It was interpreted as the damping of the phonon by the rotation of the CO_3 groups. By quantification of the softening and broadening of the IXS spectra, the timescale of the reorientation was determined. It was shown that at 1000 K the CO_3 groups reorient every 7 ps on average, while closer to the transition to the calcite-V phase, at 1200 K, they reorient every 0.4 ps on average. In the calcite-V phase the rotation is faster than 0.1 ps, that is the CO_3 groups rotate faster than 10 THz.

In summary this dissertation presents three studies investigating different aspects of lattice dynamics and the connection to the phase transitions. A geoscientifically significant calcium, magnesium and iron carbonates were investigated by combination of inelastic x-ray scattering and thermal diffuse scattering, as well as supplementary Raman scattering and heat capacity measurements at various pressures and temperatures, supplemented by DFT based calculations. This allowed to determine the structure, stability and physical properties of these carbonates at the deep Earth conditions, which broadens the knowledge of deep carbon cycle and faith of carbonates in the mantle.

Abbreviations and mineral names

List of abbreviations used throughout the thesis:

BZ	Brillouin zone
DFT	density functional theory
DS	diffuse scattering
HT	high-temperature
HP	high-pressure
IXS	inelastic x-ray scattering
SCXRD	single-crystal x-ray diffraction
TA	transverse acoustic (phonon)
TDS	thermal diffuse scattering

Mineral names used, and their composition:

bridgmanite	MgSiO_3
calcite	CaCO_3
dolomite	$\text{CaMg}(\text{CO}_3)_2$
magnesite	MgCO_3
otavite	CdCO_3
periclase	MgO
siderite	FeCO_3
smithsonite	ZnCO_3

Minerals of geological origin rarely show a perfect, pure composition, and possess various impurities. In case of a major impurity, e.g. $\text{Mg}_{0.85}\text{Fe}_{0.15}\text{CO}_3$, it is typically referred to as Fe-bearing siderite (proper mineral name) or ferromagnesite (colloquial). Various styles were adapted in this work, depending on the context.

1

Introduction

Why should we want to understand *phase transitions* in *carbonates* by investigating their *lattice dynamics*?

It's all about the carbon cycle and the interior of the Earth.

1.1 Why carbonates?

The carbon cycle on Earth can be divided into a surface cycle and a deep cycle [1], sometimes referred to as the subsurface cycle, shown schematically in Figure 1.1. The surface cycle relates to the atmosphere, oceans and shallow crustal environments, while the deep carbon cycle considers the interior of the Earth down to the outer core, where the typical processes occur on geological time-scales, e.g. hundred-thousands, millions of years. As a consequence little is known about the amount and means of transport of carbon in the Earth's interior, as we can't directly monitor the dynamics of these processes and it is almost impossible to get samples from such depths.

Current estimates show that the deep interior may contain more than 90% of the Earth's carbon [3], and it is currently a matter of an intense study to determine in what form carbon is stored in the mantle. Depending on the local conditions, such as pressure, temperature and oxygen fugacity, carbon can be stored in forms of diamond, carbonatitic melts, iron carbides, C–O–H fluids and carbonates [4]. However, recent results suggest that the majority of carbon in the mantle is stored in carbonate minerals [5, 6].

Carbonates are the main mean of transport of carbon into the Earth's mantle. The oceanic sediments, that are transported into the mantle on the subducting plates, are rich in carbon originating from organic matter [7, 8], such as calcium carbonate, that builds the shells and skeletons of oceanic organisms [9]. Recent studies by Kelemen and Manning [2] have shown that previous estimates reported by Dasgupta and Hirschmann [10] on the amount of carbon subducted to the Earth's interior were not accurate, see values given in Figure 1.1, which raised a

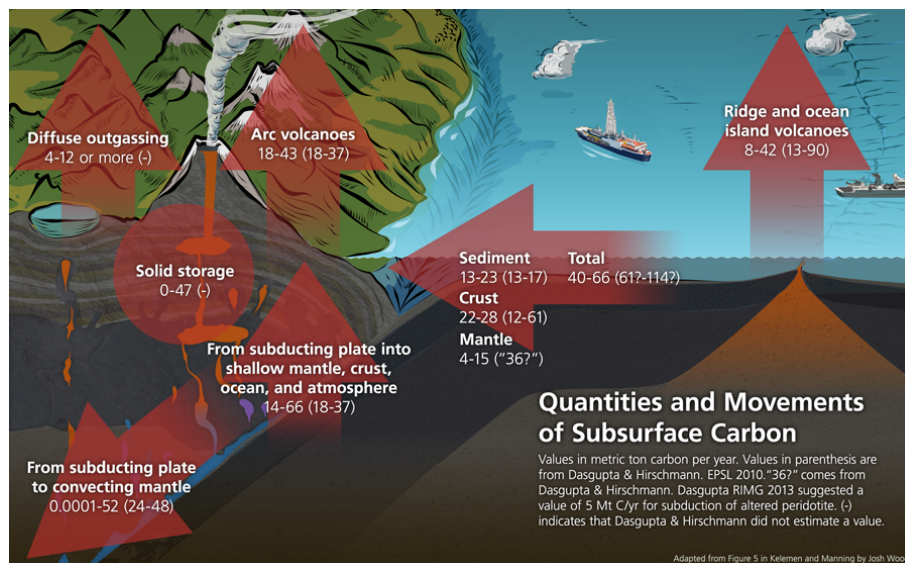


Figure 1.1: Estimates of the different carbon fluxes and storages. Values are in metric ton per year. Note the big uncertainty on the amount of carbon subducted to the mantle. Figure adapted by Joshua Wood based on the study of Kelemen and Manning [2].

hypothesis that the deep carbon cycle may not be balanced, i.e. more carbon is transported to the Earth's surface than gets subducted to the interior.

The knowledge of physical properties of carbonates can help us in modeling the deep processes and understanding the deep carbon cycle and motivated us to investigate these minerals at the conditions of Earth's interior.

1.2 Why phase transitions?

The currently established way to study the Earth's interior is to employ seismic measurements in order to determine the velocity profile, as in an example shown in Figure 1.2. The next step is to recreate the high-pressure and high-temperature conditions corresponding to specific depth in the laboratory, and examine the physical properties of the minerals that could be present in there. With such knowledge we can construct models that include various hypothetical processes, and check their validity with constraints given by the experiments.

When a mineral undergoes a phase transition at specific pressure and temperature, it usually changes its physical properties. In this study the main interest concerns the speed of seismic waves, sound velocities, propagating in the given mineral. If the sound velocities are affected by the transition, usually associated with a change in density, we call it a seismic signature. If the conditions for the phase transition match with the depth of some velocity anomaly from the seismic measurements, it gives us an indication that the considered mineral can be present there.

1.3 Lattice dynamics

Among the properties that are of geoscientific interest, the one that are based on the lattice dynamics are perhaps the most important. Lattice dynamics refer to the vibrations of atoms in crystals, and is described with a rather complex mathematical formalism of normal modes. The knowledge of how atoms vibrate in different modes allows to determine such quantities as sound velocities, heat capacity, and estimate the thermal conductivity.

Sound velocities are of particular importance, as the knowledge of the Earth's inner structure is primarily based on the observation of seismic waves. Currently, it is possible to reconstruct the 3D velocity profile in the Earth's mantle, based on the tomographic data, with an example presented in Figure 1.2 [11]. With the current state-of-the-art methods the spatial resolution of such reconstructions is of the order of hundred kilometers and the velocity contrast is resolved down to tens of percent [11–13].

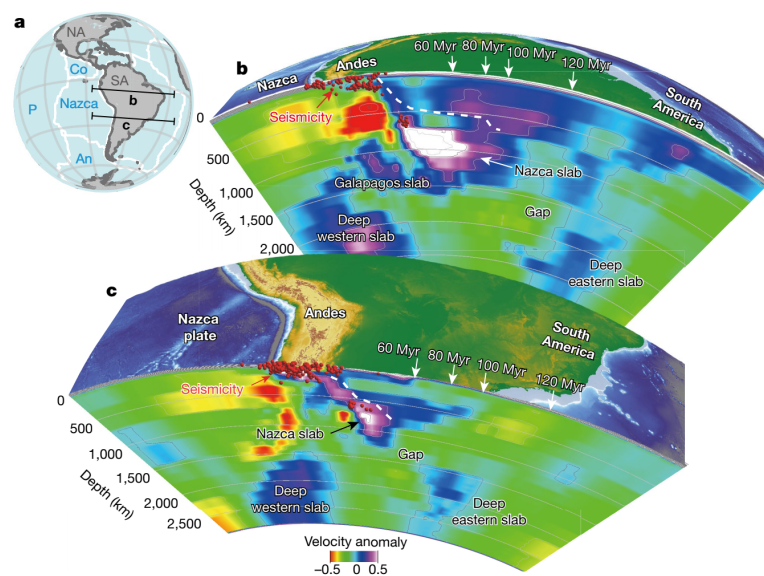


Figure 1.2: Seismic tomography measurements allow to determine the 3D velocity profile of the Nazca plate subducted under South America. (a) Overview map showing the cuts 'b' and 'c' on which the velocity was reconstructed in figures (b) and (c) respectively. Figure adapted from Chen et al. [11].

There is still a room for improvement for the seismological measurements. Arrays of seismic stations are employed for seismic tomography, e.g. USarray [14] and many others [15], which could take advantage of shear anisotropy measurements [16], or maybe even the preferred orientation of the subducted material [16]. Recent reports on the neutrino tomography of the Earth have shown some interesting results [17] indicating a new possible path in geosciences.

1.4 Scope of the thesis

This thesis reports the results of three projects, motivated by the reasons presented in this chapter. The same methodology was established in each case, that is a combination of experimental and computational methods giving information about the lattice dynamics, introduced in Chapter 2.

The first study presented in Chapter 3 aims at investigating the seismic signature of the deep mantle carbonates by determining the elastic tensor of magnesium-iron carbonate. The obtained data was used to derive sound velocities and other elastic properties for any given composition of $\text{Mg}_{1-x}\text{Fe}_x\text{CO}_3$ up to 60 GPa. The dataset was employed to discuss the detectability of deep mantle carbonate.

The following chapters are less geoscientific driven, and explore the physics of phase transition in carbonates. Chapter 4 is dedicated to the high-pressure lattice dynamics in various carbonates. It shows that the transition from calcite to calcite-II, as well as from dolomite to dolomite-II, are driven by a lattice instability corresponding to the transverse acoustic phonon. In order to determine the cation effect on the phonon behavior we investigated magnesite, siderite, smithsonite and otavite at ambient conditions.

Finally, Chapter 5 presents the results of high-temperature measurements of the lattice dynamics of calcite, CaCO_3 , and its connection to the dynamic disorder of the CO_3 groups. By establishing a model of coupling the F -point phonon to the rotational disorder we were able to determine the time-scale on which the reorientation of the CO_3 groups occurs.

2

Lattice dynamics, formalism and methods

The quantitative description of vibration of atoms in a crystal lattice, namely lattice dynamics, was formulated at the beginning of the XXth century. The first compendium on lattice dynamics is the frequently cited book *Dynamical Theory of Crystal Lattices* by M. Born and K. Huang (1954) [18]. The formalism developed therein is applied up to this date. Since many other books and publications [18–21] were dedicated to derivation and application of the formulas describing the vibrations of atoms in crystals, only the ready-to-apply formulas will be presented here, necessary to analyze and interpret the data presented in following chapters, and defining the adapted notation.

2.1 Mathematical formalism of lattice dynamics

¹In a crystal the position of a specific atom at time t can be defined as

$$\mathbf{R}_{ls}(t) = \mathbf{R}_l + \mathbf{r}_s + \mathbf{u}_{ls}(t), \quad (2.1)$$

where \mathbf{R}_l is the lattice vector pointing to the l -th unit cell, \mathbf{r}_s is the position of atom s within the unit cell, and $\mathbf{u}_{ls}(t)$ is the displacement of the atom from its equilibrium position. The information on lattice dynamics is contained in the displacement vector $\mathbf{u}_{ls}(t)$.

In order to determine the functions describing the displacement vector, one starts from defining the total energy of the crystal as the Taylor expansion of the total energy in terms of atomic displacement

$$E = E_0 - \sum_{l,s} \mathbf{F} \mathbf{u}_{ls} + \frac{1}{2} \sum_{\substack{l,s \\ l',s'}} \mathbf{u}_{ls}^T \Phi_{lsl's'} \mathbf{u}_{l's'} + O(u^3). \quad (2.2)$$

¹Notation presented here is based on M. Dove's book *Introduction to lattice dynamics* [19].

Two additional quantities were introduced: residual force vector $F_{l_s}^\alpha$ and force constant matrix $\Phi_{l_s l'_s s'}$ defined as

$$F_{l_s}^\alpha = -\frac{\partial E}{\partial u_{l_s}^\alpha}, \quad (2.3)$$

$$\Phi_{l_s l'_s s'}^{\alpha\beta} = \frac{\partial^2 E}{\partial u_{l_s}^\alpha \partial u_{l'_s}^\beta}, \quad (2.4)$$

where the index α runs over the cartesian components x, y, z . In the mechanical equilibrium there are no residual forces, thus $F_{l_s}^\alpha = 0$. Additionally the harmonic approximation is considered [18], where third and higher order terms in 2.2, denoted as $O(u^3)$ are neglected. This allows the simplification of the equation 2.2 to the well known harmonic oscillator equation.

The displacement vector can be then expressed as a general solution to the harmonic equation

$$\mathbf{u}_{l_s}(t) = \frac{1}{\sqrt{Nm_s}} \sum_{\mathbf{q}, j} \text{Re} \{ a_j(\mathbf{q}) \boldsymbol{\varepsilon}_{j_s}(\mathbf{q}) \exp [i\mathbf{q} \cdot (\mathbf{R}_l + \mathbf{r}_s) + i\omega_j(\mathbf{q})t] \}, \quad (2.5)$$

with N being the number of unit cells in the crystal, m_s the mass of the atom s , j running over the $3Z$ possible solutions to the equation, called vibrational modes, Z being the number of atoms in the unit cell, \mathbf{q} is a vector in the first Brillouin zone, $a_j(\mathbf{q})$ the normal coordinate of the vibrational mode, $\boldsymbol{\varepsilon}_j(\mathbf{q})$ the normalized atomic displacement pattern, sometimes called the eigenvector, and $\omega_j(\mathbf{q})$ the frequency of the vibrational mode. Such a solution introduces the decomposition of the displacement $\mathbf{u}_{l_s}(t)$ into normal modes. Each mode is labelled with wavevector \mathbf{q} and index j and is independent of the other modes. The frequency and atomic displacement vector of a mode are defined as a solution to the eigenproblem

$$\mathbf{D}(\mathbf{q}) \boldsymbol{\varepsilon}_j(\mathbf{q}) = \omega_j^2(\mathbf{q}) \boldsymbol{\varepsilon}_j(\mathbf{q}), \quad (2.6)$$

where $\mathbf{D}(\mathbf{q})$ is the dynamical matrix defined as

$$D_{ss'}^{\alpha\beta}(\mathbf{q}) = \frac{1}{\sqrt{m_s m_{s'}}} \sum_l \Phi_{l_s l'_s s'}^{\alpha\beta} e^{i\mathbf{q} \cdot (\mathbf{R}_l + \mathbf{r}_s - \mathbf{R}_{l'} - \mathbf{r}_{s'})}. \quad (2.7)$$

With such a notation the definition of the atomic displacement vector $\boldsymbol{\varepsilon}_{j_s}(\mathbf{q})$ is

$$\boldsymbol{\varepsilon}_{j_s}(\mathbf{q}) = \sqrt{m_s} \mathbf{U}_{j_s}(\mathbf{q}), \quad (2.8)$$

where $\mathbf{U}_{j_s}(\mathbf{q})$ is the physical displacement of the atom.

Decomposition into the normal modes allows to consider the lattice vibration as collective movement of all atoms in a crystal. Instead of describing the displacement of each atom separately, which means considering $\approx 3N_A$ variables, the problem was reduced to $3Z$ dimensions, where Z is the number of atoms in the unit cell. It is worth to summarize that the displacement $\mathbf{u}_{ls}(t)$ is a 3-dimensional vector, atomic displacement pattern $\boldsymbol{\varepsilon}_j(\mathbf{q})$ a $3N$ -dimensional vector, however considering atom s , $\varepsilon_{js}(\mathbf{q})$ is 3-dimensional, and the dynamical matrix $\mathbf{D}(\mathbf{q})$ is a $3N \times 3N$ -dimensional matrix.

The last unknown variable from equation 2.5 is the normal coordinate $a_j(\mathbf{q})$. It is connected to the amplitude of the vibration and its determination requires further mathematical transformations and the application of quantum mechanics principles. In short the displacement (eq. 2.5) is applied to the formula for total vibrational energy (eq. 2.2), in which the force constant matrix (eq. 2.4) can be substituted by the dynamical matrix (eq. 2.7). The total energy of the system is the sum of the vibrational energy and the kinetic energy, which requires the knowledge of the velocity of each atom, which is a time derivative of the displacement. After these substitutions the total energy of the system becomes

$$E = \sum_{\mathbf{q}j} \omega_j^2(\mathbf{q}) |a_j(\mathbf{q})|^2, \quad (2.9)$$

which is the harmonic oscillator equation. The quantization of the problem starts with recognizing that the total energy of the system is described by discrete energy levels, therefore the amplitude of the vibration can adapt only discrete levels. This way one introduces the idea of a phonon, a quasiparticle representing a quantum of the amplitude of lattice vibration. As shown before, by introducing the normal modes (eq. 2.5) and the dynamical matrix equation (2.7) each solution can be labelled by the wavevector, \mathbf{q} , and the branch number j . When quantizing the lattice vibrations these labels become the characteristic quantum numbers of the phonon.

The solution of the quantum harmonic oscillator equation yields discrete energy levels

$$E = \sum_{\mathbf{q}j} \hbar \omega_j(\mathbf{q}) \left(n_j(\mathbf{q}) + \frac{1}{2} \right), \quad (2.10)$$

provided by the fact that $n_j(\mathbf{q})$ is an integer, called the occupation number, denoting the number of phonons in a state characterized by quantum numbers \mathbf{q} , j . The average number of phonons in a given state is determined by the temperature

$$\langle n_j(\mathbf{q}, T) \rangle = \frac{1}{e^{\hbar \omega_j(\mathbf{q})/k_B T} - 1}. \quad (2.11)$$

Since only the average of the occupation number can be determined, only the average value of the normal coordinate can be derived. It is given by

$$\langle |a_j(\mathbf{q})|^2 \rangle = \frac{\hbar}{\omega_j(\mathbf{q})} \left(\langle n_j(\mathbf{q}, T) \rangle + \frac{1}{2} \right) = \frac{\hbar}{2\omega_j(\mathbf{q})} \coth \left(\frac{\hbar\omega_j(\mathbf{q})}{2k_B T} \right). \quad (2.12)$$

By including this equation into 2.5 an average quadratic displacement can be calculated as:

$$\langle u_{l_s}^\alpha u_{l_s}^\beta \rangle = \frac{1}{Nm_s} \sum_{\mathbf{q}j} \langle a_j(\mathbf{q}) a_j(-\mathbf{q}) \rangle \varepsilon_{j_s}^\alpha(\mathbf{q}) \varepsilon_{j_s}^\beta(-\mathbf{q}), \quad (2.13)$$

where indices α and β correspond to components of the vector in the Cartesian coordinate system. This quadratic displacement is connected to the Debye-Waller factors, and yield information on the direction and average value of the displacement of each atom.

In summary, lattice vibrations were decomposed into the normal modes as defined by equation 2.5. Each mode can be quantized by discretization of the allowed energy levels, which naturally introduces the idea of a phonon. A phonon is a quasiparticle with crystal momentum \mathbf{q} , energy $\omega_j(\mathbf{q})$ and an atomic displacement pattern $\varepsilon_{j_s}(\mathbf{q})$. Its energy is a function of the wavevector, called phonon dispersion relation, and is one of the solutions to equation 2.6. Different solutions of this equation, labelled with j , are called phonon branches. The amplitude of a normal mode is given by the number of phonons that are in the state corresponding to that mode, according to the equation 2.12.

2.2 Methods for determining the lattice dynamics

As shown in the previous section the number of parameters describing the lattice vibrations is extremely large. This is due to the fact, that the atomic displacement pattern is different for each wavevector. Determining the displacement pattern experimentally is in general possible, however the complexity of such a task increases drastically with the number of atoms in the unit cell. In practice, the knowledge of the phonon dispersion relations along few high symmetry directions in the reciprocal space is considered to be enough, and is referred to as full lattice dynamics.

There are many experimental techniques probing the phonon excitations in crystals, the most widely used are summarized in a chronological order on figure 2.1. In case of the projects undertaken in here two of them are of particular importance: inelastic x-ray scattering, IXS and thermal diffuse scattering, TDS. As will be described in detail in the following sections 2.2.1 and 2.2.2, IXS is able to

fully determine the lattice dynamics in the scope of the definition stated before, however the determination of the displacement pattern of a specific phonon is practically impossible. TDS is a technique that in the current state allows identifying regions in reciprocal space with potentially interesting, low energy, phonons.

As the experimental methods provide limited information on the lattice dynamics they are usually accompanied by computational studies. The current state-of-the-art methods are based on DFT calculations, that are able to determine the dispersion curves and displacement pattern for each phonon branch at an arbitrary wavevector. The task of performing reliable calculations is quite complex, some basic principles will be presented in section 2.2.3.

Table 2.1: Experimental methods for investigating lattice dynamics in order of the first reported application. Adapted from Krisch [22].

method		year	authors	cit.
Infrared absorption	IRS	1881	W. Abney and E. Festing	[23]
Brillouin light scattering	BLS	1922	L. Brillouin	[24]
Raman scattering	RS	1928	C.V. Raman and K.S. Krishnan	[25]
Thermal diffuse scattering	TDS	1948	P. Olmer	[26]
Inelastic neutron scattering	INS	1955	B.N. Brockhouse and A.T. Stewart	[27]
Impulsive stimulated light scattering	ISS	1984	M.M. Robinson et al.	[28]
Inelastic x-ray scattering	IXS	1987	B. Dorner et al.	[29]
Nuclear inelastic scattering	NIS	1995	M. Seto et al.	[30]

2.2.1 Inelastic x-ray scattering

IXS is a method allowing the determination of dispersion curves. It allows the investigation of non-transparent samples, which is a limitation of Brillouin light scattering, probes the phonons at arbitrary momentum transfer, as opposed to Raman and infrared spectroscopy that are sensitive only to Γ phonons, and allows the investigation of micrometer sized samples whereas inelastic neutron scattering requires samples of millimeter to centimeter size. The last advantage is thanks to the x-ray optics employed at synchrotron sources that are able to focus the x-ray beam to the micrometer size, and allow measurements at gigapascal pressures in diamond-anvil cells, imitating shallow and deep Earth conditions. The IXS technique, a comparison of current state-of-the-art IXS spectrometers and

comparison of IXS to other techniques was described extensively in the script by Baron [31].

The IXS measurement allows to measure the dynamic structure factor, given as

$$S(\mathbf{Q}, \omega) = \sum_j G_j(\mathbf{Q}) F_j(\mathbf{Q}, T, \omega), \quad (2.14)$$

where \mathbf{Q} is the momentum transfer defined as the difference between scattered and incoming radiation wavevectors $\mathbf{Q} = \mathbf{k}_f - \mathbf{k}_i$. The dynamical structure factor was split into the geometrical factor

$$G_j(\mathbf{Q}) = \left| \sum_s \frac{1}{\sqrt{m_s}} f(\mathbf{Q}) e^{-W_{DW}(\mathbf{Q}) + i\mathbf{Q} \cdot \mathbf{r}_s} (\mathbf{Q} \cdot \boldsymbol{\varepsilon}_{js}(\mathbf{q})) \right|^2 \quad (2.15)$$

and the thermal factor

$$F_j(\mathbf{Q}, T, \omega) = \frac{1}{\hbar \omega_j(\mathbf{q})} [(\langle n_j(\mathbf{q}) \rangle + 1) \delta(\omega - \omega_j(\mathbf{q})) + \langle n_j(\mathbf{q}) \rangle \delta(\omega + \omega_j(\mathbf{q}))]. \quad (2.16)$$

Here \mathbf{q} is the phonon wavevector which is the total momentum transfer \mathbf{Q} reduced to the first Brillouin zone. $W_{DW}(\mathbf{Q})$ is the Debye-Waller factor defined as

$$W_{DW}(\mathbf{Q}) = \frac{1}{2} (\mathbf{Q} \cdot \mathbf{u}_s)^2 = \frac{1}{2Nm_s} \sum_{qj} |a_j(\mathbf{q})|^2 |\mathbf{Q} \cdot \boldsymbol{\varepsilon}_j(\mathbf{q})|^2, \quad (2.17)$$

describing the average quadratic displacement of the atoms, as introduced in equation 2.13

With such separation it is easy to see that the dispersion relation $\omega_j(\mathbf{q})$ is determined by the position of the peak as defined by the thermal factor $F_j(\mathbf{Q}, T, \omega)$ and its intensity is given by the geometrical factor $G_j(\mathbf{Q})$.

In reality one needs to take into account the resolution function of the spectrometer $R(\mathbf{Q}, \omega)$ that needs to be convoluted with the dynamical structure factor and the background $b(\mathbf{Q}, \omega)$ that is added to the spectrum resulting in the measured intensity

$$I(\mathbf{Q}, \omega) = S(\mathbf{Q}, \omega) * R(\mathbf{Q}, \omega) + b(\mathbf{Q}, \omega), \quad (2.18)$$

where the convolution applies to the frequency domain.

In the studies undertaken in this thesis IXS was employed as a method for determining the sound velocities of iron carbonate at high pressures, Chapter 3, measurement the dispersion curve of calcite, dolomite and magnesite at high pressures, Chapter 4, and determining the temperature dependence of a phonon branch in calcite at high temperature, Chapter 5. All measurements were performed at the ID28 beamline at the ESRF synchrotron in Grenoble, France. The

beamline characteristics are described in detail on the ID28 webpage [32] and in the review paper by Krisch and Sette [33].

2.2.2 Thermal diffuse scattering

Thermal diffuse scattering, TDS, is a type of diffuse scattering, DS, that has its origin in lattice vibrations. In general, diffuse scattering can originate from a variety of physical phenomena, other than diffraction, meaning that it arises from any imperfection in the model of a perfect lattice with atoms at fixed positions [34, 35].

Lattice vibrations give rise to the diffuse signal that can be quantified by the formalism described in the previous section. One might think of the TDS signal as *almost* elastic, because the inelastic energy transfer is in the range of meV, while the energy of the incoming synchrotron radiation is of tens of keV. Thus the formula for the TDS signal intensity is derived from the diffraction intensity assuming the displacement of the atoms from the equilibrium position according to formula 2.5. Limiting the corrections to the first order, i.e. omitting the anharmonic effects, the formula for the TDS intensity yields:

$$I_{TDS}(\mathbf{Q}) = \sum_j \frac{1}{\omega_j(\mathbf{q})} \coth\left(\frac{\hbar\omega_j(\mathbf{q})}{2k_B T}\right) \left| \sum_d \frac{1}{\sqrt{m_s}} f_d(\mathbf{Q}) e^{-W_{DW}(\mathbf{Q}) + i\mathbf{Q}\cdot\mathbf{r}_s} (\mathbf{Q} \cdot \boldsymbol{\varepsilon}_{js}(\mathbf{q})) \right|^2. \quad (2.19)$$

The formula for TDS intensity resembles the dynamical structure factor, as in 2.14, however it is not energy resolved. High I_{TDS} will arise in the regions of reciprocal space where $\omega_j(\mathbf{q})$ is small, as after expanding the $\coth(\dots) \approx 1/\omega$, it follows that $I_{TDS} \approx 1/\omega^2$.

Historically TDS was the first experimental technique employed to determine phonon dispersion relations [26], see Table 2.1. After the first experiments the TDS measurements were abandoned due to rise of more convenient techniques like INS and IXS. However, with the rise of novel hybrid area detectors and the brilliant synchrotron sources the TDS measurements were revived.

A diffuse scattering measurement is essentially a single crystal diffraction experiment focused on identifying the intense spots apart from Bragg reflections. The use of novel hybrid detectors allows to count single photons, surpass x-ray fluorescence, which greatly reduces the background signal, and achieve great spatial resolution due to single pixel point spread function of the detector used. The most prominent detectors are from the Pilatus and Eiger family from the DECTRIS company [36]. The use of synchrotron sources allows to efficiently collect the DS signal, due to the unique characteristics of synchrotron radiation. High intensity of the x-ray beam allows for relatively fast data collection, e.g.

30 minutes to perform a full ϕ scan at the ID28 side-station. Small divergence of the source combined with modern x-ray optics provides the possibility to focus the beam to the micrometer size spot, $50 \times 50 \mu\text{m}^2$ at ID28, which allows for performing the measurements at gigapascal pressures in the diamond-anvil cells.

The results of the DS measurements presented here were performed at the side station of ID28 at the ESRF. The characteristics of the instrument are presented in Girard et al. [37]. The side station acts as a tool to explore large volumes of reciprocal space and identify potentially interesting regions with diffuse features. After that the sample can be transferred to the main station, IXS spectrometer, in order to determine the energy profile of the selected regions of the reciprocal space.

In this thesis the side station was extensively used in order to characterize diffuse features in carbonates. It was employed to investigate the F -point instability of calcite and determine its presence in other carbonates, as described in Chapter 4. It was also used to measure calcite at high temperatures, in order to determine if and how the transition to calcite-IV and calcite-V is linked to lattice dynamics of calcite, with results presented in Chapter 5.

Reconstruction and processing of the diffuse scattering maps

The typical workflow for the full reconstruction of DS maps is as follows.

1. Sample preparation.
2. ϕ scan measurement with various detector positions.
3. Importing the frames to CrysAlis [38], which allows to determine the unit cell and the orientation of the crystal.
4. Reconstructing the DS maps with ProjectN [37] program, developed for the ID28 needs.
5. Post-processing:
 - (a) symmetrization, i.e. adding maps of equivalent planes and applying symmetry operations,
 - (b) filtering,
 - (c) smoothing.

The best DS maps can be obtained with a high-quality single crystal of appropriate size. Typically rod-shaped crystals are prepared, with a diameter corresponding to the absorption length of its material. The crystal is then etched in order to clean the surface from possible contamination and reduce its roughness. Finally it is mounted with the long dimension perpendicular to the beam direction, which allows for illumination of the same volume during the ϕ -scan rotation.

In order to enhance the visibility of the signal that is investigated, some post-processing can be performed. The example here will be the smithsonite sample examined in the study presented in Chapter 4. The crystals were small, 20 μm in diameter, their quality was not excellent, and the surface was highly contaminated with powders of other phases.

Symmetrization

In order to access large volumes of reciprocal space the measurement is performed with two detector positions, one for measuring low momentum transfer range, $0 \text{ \AA}^{-1} < Q < 6 \text{ \AA}^{-1}$, and a second for high range, $4.4 \text{ \AA}^{-1} < Q < 11 \text{ \AA}^{-1}$. The planes reconstructed from these two measurements are combined and symmetrized, i.e. rotated, flipped or inverted, according to the symmetry of the crystal. This can also reduce the void regions, present due to the spacing between the detector panels.

Filtering

The features emerging from low crystalline quality are usually sharply localized in reciprocal space. Two typical ones are (I) straight diffuse streaks across the Bragg reflections, that originate from stacking faults, or (II) arc streaks around Bragg reflections with the center in the origin of the reciprocal space, originating from high mosaicity of the crystal.

As the diffuse scattering signal originating from phonons is smooth, the goal of the post-processing is to remove sharp features in the maps. Additional advantage is the removal of the dead pixels of the detector, that were not masked properly. The efficient tool for that is the median filter, which removes sharp, high-intensity signal.

Smoothing

As a sample might be small and not perfectly centered, different volumes of the crystal could have been illuminated during rotation. This results in discontinuous regions on the DS maps emerging on the intersecting parts of symmetry equivalent reconstructions. These regions can be smoothed with case-specific smearing filters.

The final map, obtained after applying the filter and symmetrization procedure is smooth and covers large volume in reciprocal space as shown in Figure 2.1, with all post-processing steps described above. Obviously, the method presented here is not universal and depends on the character of the diffuse signal that is of importance. In case of the investigation presented in Chapter 4 it was important to filter out the surface contamination reflections, in order to focus on the intensity of the TDS at various F -points. For the reconstructions presented in Chapter 5,

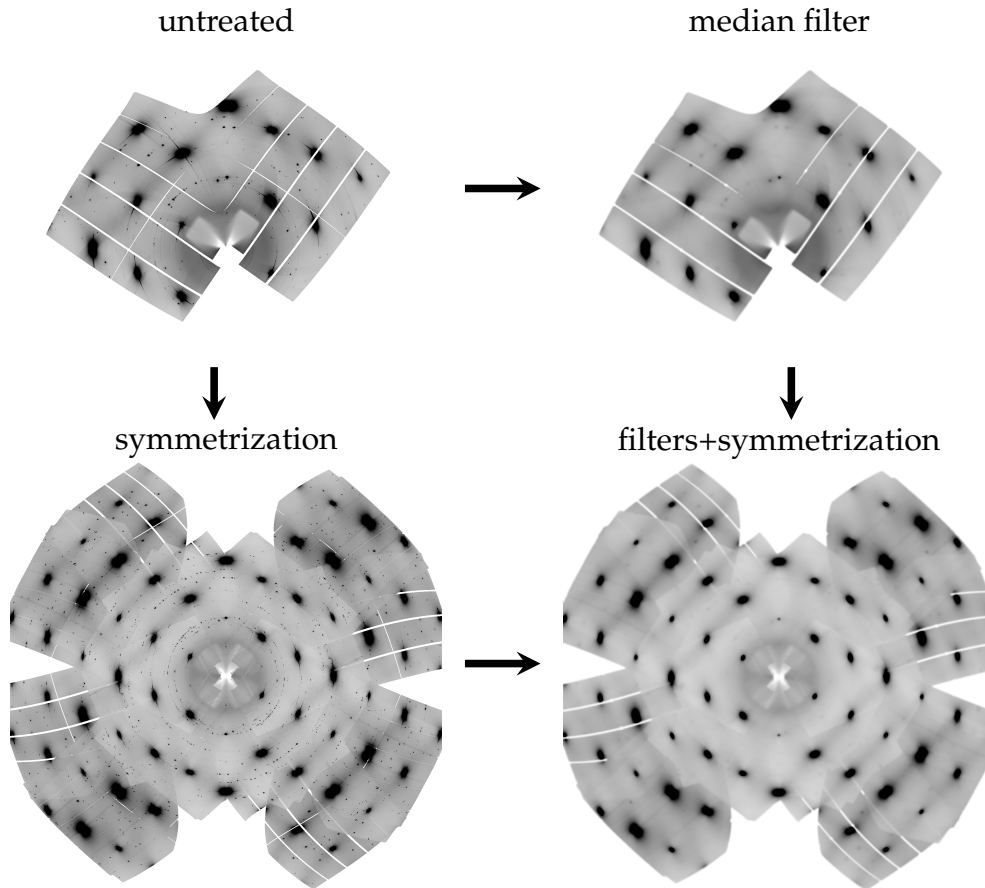


Figure 2.1: Post-processing applied for the reconstruction of the DS intensity on the (H0L) reciprocal plane in smithsonite.

where a platelet crystal was measured, the DS signal and the background was not uniform, and upon symmetrization the signal at the F -point was not averaged properly. Additionally it was of interest to observe the CaO powder rings, thus no post-processing was applied.

2.2.3 Density functional theory based calculations

DFT calculations were employed in this study in order to determine the full lattice dynamics of investigated materials, however, in general, their application is much broader. Their basic working principle is that they allow to determine the energy of the given crystal structure [39]. The energy calculation is based on the theoretical framework laid out by Hohenberg and Kohn [40] and put into practical usage by the set of the so called Kohn-Sham equations defined in their famous work Kohn and Sham [41]. These two works constitute the foundation of density functional theory. A thorough explanation of the theory, methods and their implementation is a rather lengthy topic, covered in various reviews and textbooks on the DFT application [42–45], in here only the absolute minimum of

the explanation will be provided, in order to give a basic understanding on how the calculations provide the description of lattice dynamics.

As mentioned in previous paragraph, the DFT calculations are able to predict the energy of a given atomic arrangement, as introduced by the equation 2.2. The first step is to find the ground state, by a procedure called the geometry optimization. The atoms are slightly displaced from their position, in order to see if given displacement lowers the total energy, in other words their positions, geometry, are going to be optimized. In this step a number of parameters is carefully chosen to ensure the accuracy of the calculated energy. The most important one is a choice of the exchange-correlation functional, see practical explanation in Winkler and Milman [44], followed by the sampling of the reciprocal space and the cut-off energy, that control how the electronic wave-functions are going to be approximated.

In case of calculation of lattice dynamics, the next step is to calculate the dynamical matrix, see equation 2.7. In the basic picture the dynamical matrix can be found by calculating the change of the energy when displacing the atoms in the unit cell. Such approach is called a finite-displacement method, and although conceptually straightforward, is problematic when considering the displacement with arbitrary wave-vector. Another approach that solves this issue is the density functional perturbation theory, DFPT explained in details in Baroni et al. [43].

The knowledge of the dynamical matrix for an arbitrary wave-vector constitutes for the full knowledge of the lattice dynamics, since the diagonalization of the matrix provides its eigenvalues, that give vibrational frequencies, and eigenvectors, that give displacement patterns. With that knowledge one can also calculate the elastic tensor of the crystal at given pressure as well as reconstruct the TDS maps.

2.3 Linear elasticity

Chapter 3 is dedicated to determining the elastic stiffness coefficients of iron and magnesium carbonates, by combining the IXS experiment and results of the DFT based calculations. A short review of the theory of linear elasticity, based on textbook by Landau et al. [46] and a review articles [47], is presented here in order to introduce formulas enabling the deeper understanding of the results presented in that chapter. The notation adapted here gives the multi-dimensional tensor or vector symbols in bold-italics, e.g. $\boldsymbol{\sigma}$, however, when referred to their components they are written only in italics, e.g. σ_{ij} .

The base of the theory is the formulation of the Hooke's law that assumes a linear relation between the stress tensor $\boldsymbol{\sigma}$ and the strain tensor $\boldsymbol{\epsilon}$, by introducing

the elastic stiffness tensor c defined by the equation

$$\sigma_{ij} = c_{ijkl}\epsilon_{kl}. \tag{2.20}$$

As both σ and ϵ are 3×3 symmetrical tensors they have 6 independent variables, and can be mapped to a one-dimensional form, with the indices transformation $xx \rightarrow 1, yy \rightarrow 2, zz \rightarrow 3, yz \rightarrow 4, xz \rightarrow 5, xy \rightarrow 6$, also know as the Voigt notation [48]. This allows to reduce the rank of the elastic stiffness tensor from four to two, which is followed by capitalizing the symbol of the tensor, $c \rightarrow C, c_{ijkl} \rightarrow C_{ij}$. The number of independent coefficients of the elastic tensor depends on the symmetry of the considered material. For example an isotropic material has two independent coefficients, crystal with cubic symmetry three, crystal with rhombohedral symmetry and $R\bar{3}c$ space group six coefficients (some end-member carbonates). This is summarized in Figure 2.2.

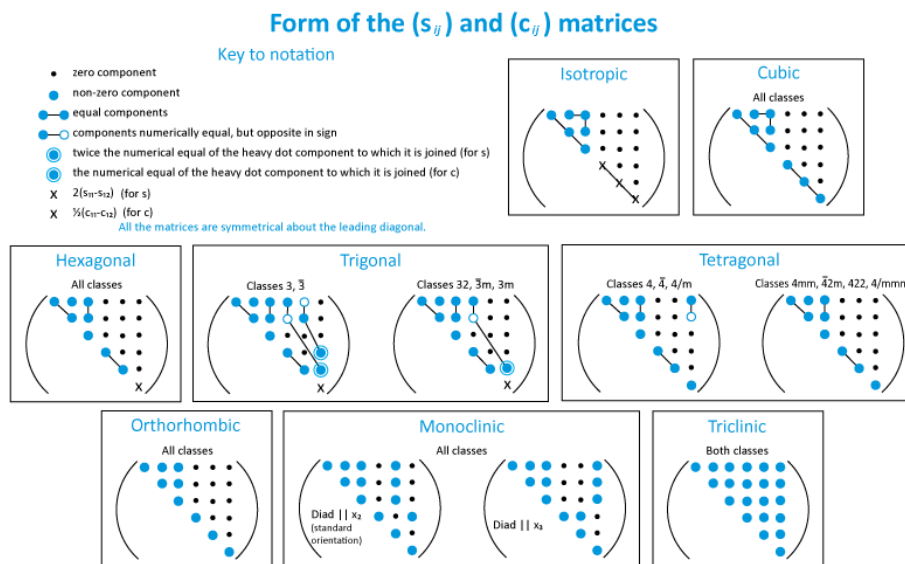


Figure 2.2: Independent elastic moduli and relations between them, for different crystal systems [49].

The determination of elastic tensor coefficients, elastic moduli, at high pressures is not a direct measurement. Currently established techniques – Brillouin light scattering and inelastic x-ray/neutron scattering – rely on measuring the dispersion relation of acoustic phonons in the vicinity of the Γ point. This allows determining the sound velocities propagating along a chosen direction in reciprocal space, as $V = \omega(\mathbf{q})/|\mathbf{q}|$. The connection of sound velocities to the elastic properties is established by considering the wave equation in the solid medium with a time dependent stress field. Solution of such an equation with the input of Hooke’s law 2.20 leads to the Christoffel equation, which allows converting

sound velocities propagating along a chosen direction to a linear combination of elastic moduli. The Christoffel equation is an eigenproblem for the reduced elastic stiffness tensor

$$l_k c_{ijkl} l_l - \rho V^2 \delta_{ij} = 0, \quad (2.21)$$

where $l_i = q_i/|\mathbf{q}|$, defines the direction of the propagation of the acoustic wave. The eigenvalues of the Christoffel equation yield the effective elastic moduli for considered direction, and the eigenvectors yield three different polarizations of the wave.

Given the symmetry of a crystal, the Christoffel equation can be simplified, to a higher degree for higher symmetry materials. A number of publications reports the exact equation for each crystal system, e.g. Auld [50] or Varughese [51]. In a case of a high symmetry direction the eigenvalue usually corresponds directly to one of the elastic modulus (typical approach in an IXS experiment), in other case one can measure the sound wave velocities along various different directions and with an overdefined set of Christoffel equations fit all elastic moduli (approach in a Brillouin scattering measurement).

3

High pressure elastic properties of (Mg,Fe)CO₃ carbonates

Iron bearing magnesite, ferromagnesite, with composition $\text{Mg}_{1-x}\text{Fe}_x\text{CO}_3$, is one of the candidates for a deep mantle carbonate [52]. As current methods of determining the structure of the Earth's mantle are limited to seismic measurements, the only way to approach the problem of a possible presence of ferromagnesite in the mantle is to determine the velocities of seismic waves propagating in ferromagnesite at mantle conditions and trying to match the seismically observed profiles.

Interesting implications come from the fact that around 44 GPa iron carbonate undergoes a phase transition. It is associated with the change of the spin state of iron [53] and the concomitant volume decrease [54]. This transition was shown to have a strong impact on the elastic properties of magnesiosiderite with composition $\text{Mg}_{0.35}\text{Fe}_{0.65}\text{CO}_3$ [55]. Additionally, it was shown that the high temperature broadens the pressure-range in which the spin transition in siderite occurs [56]. However, these studies were conducted separately and no uniform picture was established to describe the high-pressure elasticity of magnesium-iron carbonates and the influence of the spin transition in pure iron carbonate.

This chapter presents the results of a combined IXS and DFT study on high-pressure elastic properties of iron carbonate and magnesium carbonate over the spin transition in iron carbonate. It summarizes the current state of knowledge and combines it with new results in order to establish a complete picture of the high-pressure elasticity for any composition between the iron and magnesium carbonate end-members. The dataset allows to determine the sound velocity profiles of deep mantle carbonate and analyze how the spin transition affects the detectability of iron bearing carbonate in the Earth's mantle.

3.1 Introduction

Iron and magnesium carbonates are isostructural, they both crystallize in the calcite structure with rhombohedral lattice and $R\bar{3}c$ space group. They form a continuous family of solid solutions, unlike calcium and magnesium carbonates which possess a miscibility gap for any mixture other than the 1:1 calcium to magnesium ratio: dolomite, $\text{CaMg}(\text{CO}_3)_2$. That is likely because of the similar atomic radii of iron and magnesium, which does not induce distortions in the structure. At high pressures iron carbonate undergoes an isostructural transition driven by the change in the spin state of the valence electrons [53], hence its name: spin transition. This high-pressure transition was predicted already in 1960 by Fyfe [57] for a variety of iron bearing minerals, which was later confirmed experimentally for $\text{Fe}_{0.94}\text{O}$ [58], hematite, Fe_2O_3 [59, 60], and FeS [61]. Recently there was a number of experimental and theoretical studies devoted to the spin transition in iron carbonate [53, 54, 62, 63], which will be summarized here.

Iron carbonate, FeCO_3 , undergoes a spin transition between 42 and 45 GPa, that was first reported by Mattila et al. [53] who performed an x-ray emission experiment, which directly probes the electronic levels of iron. Later on, by means of single crystal diffraction, Lavina et al. [54] reported that the spin transition is isostructural and is associated with a volume collapse, as well as a color change.

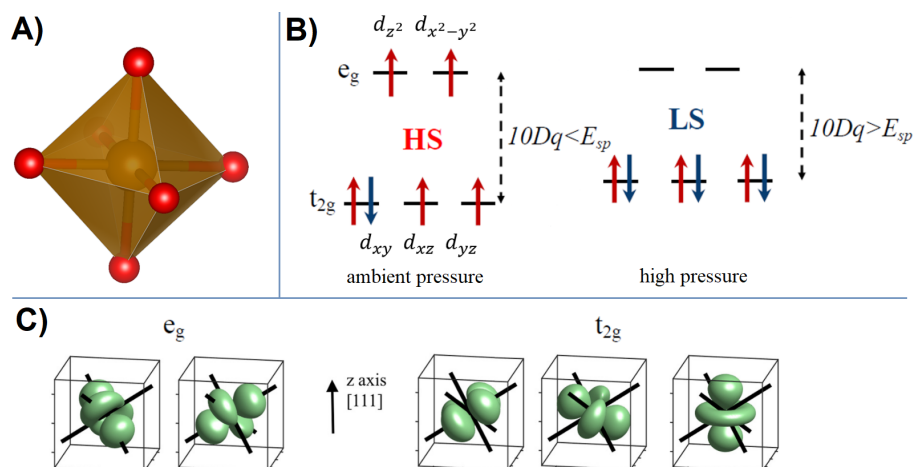


Figure 3.1: (A) Coordination of Fe^{2+} in siderite and (B) electronic structure of its 3d electrons in the high spin, HS, and low spin, LS, state. (C) Visualization of the 3d orbitals in the e_g and t_{2g} levels. Thick black lines denote the direction of the Fe–O bonds. Insets A, B adapted from Vasiukov [64], inset C from Hsu and Huang [63].

The valence electrons energy levels can be analysed on the base of the crystal field theory [65]. In siderite, iron is coordinated by six oxygens atoms in a regular octahedral configuration as shown in Figure 3.1. Such a coordination induces a splitting of the 3d electrons' energy levels into two groups labeled e_g and t_{2g} . The

energy difference between these groups is called the crystal field splitting energy and denoted with symbol $10Dq$, following the crystal field theory. At ambient pressure the electrons follow Hund's rule of occupying the orbitals and adapt the high-spin state, HS, with total spin $S = 2$, as shown in Figure 3.1. This is because it's energetically favorable to occupy the higher energy e_g level, than to pair with an electron on an occupied orbital and overcome the Coulomb repulsion between electrons, also called the spin-pairing energy E_{sp} . The situation changes at high pressure, where $10Dq$ increases, and at some point exceeds E_{sp} . That is when the spin transition occurs, and two electrons from the e_g level pair with two electrons in the t_{2g} level, resulting in the low-spin, LS, state with $S=0$. This effect was extensively studied for temperature-driven spin transitions, summarized by Gütlich and A. [66], and can be adapted to the high-pressure case in the classical picture as follows. The shape of the d_{z^2} and $d_{x^2-y^2}$ orbitals, that compose the e_g level, is such that in the octahedral configuration electrons in these orbitals are closer to the electron clouds of oxygens, than if they would be in any orbital composing the t_{2g} level, see Figure 3.1. Thus, they need to have higher energy than t_{2g} electrons, in order to overcome the Coulomb repulsion between themselves and the oxygen electron cloud. With increasing pressure the distance between the oxygen atoms and the central iron atom decreases [54], so that iron e_g and oxygen electron clouds are brought closer together and the energy of e_g electrons increases, due to Coulomb repulsion. At some point the oxygens are so close that the repulsion pushes the e_g electrons to the t_{2g} level overcoming the spin-pairing energy E_{sp} . Additionally the jump of electrons from the e_g level to the t_{2g} level induces a jump in the distance between iron and oxygens as they are no longer in the way between iron and oxygen, and allow them to be brought closer together, which results in the volume collapse observed by Lavina et al. [62]. Such interpretation is rationalized by the ionic character of the $Fe^{2+}-O^{2-}$ bonding, where the valence electrons are localized on the respective atoms.

Additionally, there was a hypothesis on the existence of an intermediate spin state, IS, in which only one electron jumps from the e_g level to the t_{2g} level resulting in a total spin $S=1$. This was raised due to the observation of a wide pressure range in which the transition proceeds, and apparent continuity of the transition. Calculations of Hsu and Huang [63] show that the IS state is energetically unfavorable, and the spin transition proceeds from the HS to the LS state directly. It seems to be agreed upon that the before-mentioned effects were observed due to pressure gradients in the experiments. This causes a situation in which part of the sample is in the HS state and another one in the LS state, referred to as the mixed-spin state, MS. This was shown by Müller et al. [67], evident as a color gradient on the sample.

Many studies have been dedicated to determine how the spin transition affects the physical properties of iron bearing minerals. They have been primarily applied to more abundant minerals in the mantle than carbonate: bridgmanite [68, 69] and ferropericlase [70], however recently data on magnesiosiderite, Mg_{0.35}Fe_{0.65}CO₃, have been reported [55]. It turns out, that the effect of spin transition on the elastic stiffness moduli, from which all other elastic properties can be derived, is very similar in these iron-bearing minerals.

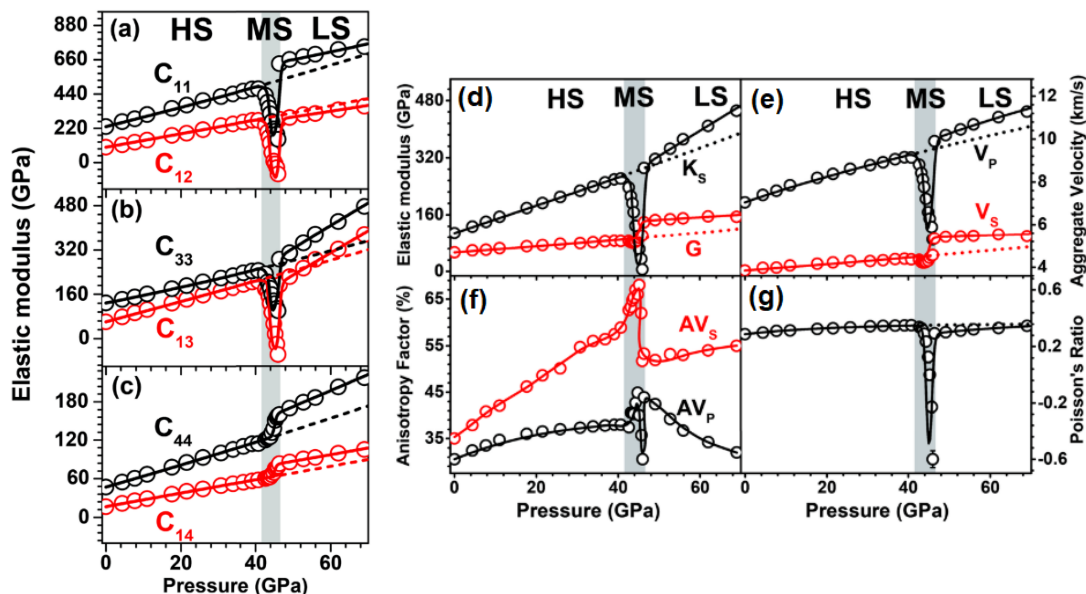


Figure 3.2: (a,b,c) Elastic stiffness moduli of Mg_{0.35}Fe_{0.65}CO₃, and elastic properties derived from them: (d) bulk moduli, (e) sound velocities, (f) velocity anisotropies, and (g) Poisson ratio. HS: high-spin, MS: mixed-spin, LS: low-spin states, described in the text. Figure adapted from Fu et al. [55].

Figure 3.2 shows the results of the combined Brillouin light scattering and impulsive stimulated light scattering experiments on Mg_{0.35}Fe_{0.65}CO₃, reported by Fu et al. [55]. The most interesting feature in their results is the abnormal behavior of the C_{11} , C_{12} , C_{13} , and C_{33} moduli in the mixed spin state, where they have a local minimum. On the other hand the C_{14} and C_{44} moduli monotonically increase their values over the spin transition.

This effect might be explained qualitatively. Following the Voigt notation introduced in chapter 2.3, the 1, 2, 3, 4 indices of elastic moduli correspond to the xx , yy , zz , yz components of the strain/stress tensor, respectively. From that it follows, that e.g. the C_{11} modulus is a relation between the stress component xx arising from applying the strain xx , $C_{11} = \sigma_{xx}/\varepsilon_{xx}$. When iron carbonate is in the mixed spin state some of the FeO₆ octahedra are contracted, i.e. in the LS state, and some of them are not, the ones in the HS state [62]. When an additional pressure is applied in form of a strain ε_{xx} it results in contraction of the FeO₆

octahedra in the HS state, instead of building up the strain. In other words, the contraction of the FeO_6 octahedra in the MS state provides a mechanism of a stress relief upon applied strain. This mechanism results in a lower value of the C_{11} modulus taken as an example, but can be directly translated to C_{33} , C_{12} , and C_{13} as they also describe a strain in a form of contracting (pressurizing) the material. The behavior of the C_{14} and C_{44} moduli is drastically different as the strain involved in the deformation $\varepsilon_4 = \varepsilon_{yz}$ is actually a shear. Shearing the material does not induce additional pressurization thus it also does not induce the contraction of FeO_6 octahedra. That is why these moduli do not exhibit anomalous behavior. The interesting fact is that the C_{ij} 's are symmetrical, so that $C_{14} = C_{41}$, and different argumentation has to be applied to C_{41} . Once again the deconvolution of Voigt notation yields that C_{41} defines the relation of stress σ_{yz} , which is a shear, arising due to the strain ε_{xx} . Lavina et al. [62] have shown that contraction of the FeO_6 octahedra does not involve its rotation, i.e. the jump in oxygen atoms position is in the direction radial to the central iron atom. Thus, the contraction of the octahedra will not induce any shear, which explains why the C_{41} modulus behaves normally.

This anomalous behavior of C_{ij} 's in iron carbonate has direct consequences on its elastic properties. In this study the sound velocities are the main focus. Interestingly, an anomaly was observed for V_p in the MS region but not for V_s , see Figure 3.2 [55]. Sound velocities are derived from C_{ij} 's by solving the Christoffel equation 2.21, where $V \propto \sqrt{C/\rho}$, so that their anomalous/normal behavior depends on what C_{ij} 's constitute on the respective sound velocity. However, the behavior of sound velocities can be explained without referring to the Christoffel equation. Once again invoking the definition of the considered properties allows the explanation of observed phenomena. V_s is a shear wave, as it corresponds to the propagation of a local shear gradient. As explained above, applying shear to iron carbonate in the MS state does not induce anomalies, thus the V_s behaves normally. On the other hand the compression waves velocity, V_p , will be effectively slowed down by the contraction of FeO_6 .

Although the Brillouin light scattering technique is very efficient in determining elastic moduli, its accuracy is limited for samples that are not optically transparent at given conditions. As shown by Lobanov et al. [71] iron carbonate becomes opaque after the spin transition and BS experiments become tedious. The technique able to measure elastic properties of opaque samples at high pressures is IXS. However, IXS experiments are time limited as they can be performed only at synchrotron sources where users have limited time for their experiments. This does not allow performing measurements with fine pressure steps required to investigate the mixed-spin region in iron carbonate. A typical procedure is to combine the IXS measurements with computational modeling of material properties.

Then the IXS measurements are used as a benchmark for the calculations, which in turn allow derivation of full lattice dynamics of the considered material.

Although it is extremely interesting, modeling the elastic properties of iron carbonate in the mixed-spin state is computationally difficult. It is easier and much faster to derive the bulk properties such as bulk modulus, which requires "only" the geometry optimization of the structure, see Hsu and Huang [63] which beautifully, but not perfectly, reproduce the experimental data.

In result, the current study was limited to modeling the elastic properties of iron carbonate only in the spin-pure state: either HS or LS. Additionally, the IXS measurements were limited to extracting the values of the C_{33} and C_{44} moduli, and determining the other moduli from the calculations. We have combined the results of the high pressure experiments on MgCO₃ [72] and FeCO₃ (this study) with the DFT based calculations, which allowed us to determine the full elastic tensor for MgCO₃ and FeCO₃. In the end we have combined the before-mentioned results with the dataset on Mg_{0.35}Fe_{0.65}CO₃ [55] to interpolate the elastic properties of Mg_{1-x}Fe_xCO₃ carbonate for any composition, x , up to 60 GPa. This dataset allows the derivation of sound velocities and velocity anisotropies of Mg_{1-x}Fe_xCO₃ carbonate, which allows determining its seismic signature and test the possibility of its presence in the lower mantle.

3.2 Experimental methods

Single crystals of FeCO₃ were synthesized by the method developed by French [73] and described in details by Cerantola et al. [74] in Bayerisches Geoinstitut (Bayreuth, Germany). Crystals with low mosaicity and appropriate size were chosen for the high pressure IXS experiments. The crystals were loaded in diamond-anvil cells using neon or helium as pressure transmitting media. At least two rubies were loaded in each cell for estimation of pressure in the cell. More details are presented in Table 3.1, photographs of the samples are shown in Figure 3.3. The pressure was measured before and after each IXS measurement.

Table 3.1: Details of the DACs prepared for the IXS experiments. PTM: pressure transmitting medium.

	DAC type	PTM	crystal dimensions	measured pressure
DAC-10	Boehler-Almax	neon	$35 \times 30 \times 15 \mu\text{m}^3$	15 GPa
DAC-28	Boehler-Almax	neon	$80 \times 50 \times 22 \mu\text{m}^3$	2 GPa and 28 GPa
DAC-E	symmetric	helium	$25 \times 25 \times 10 \mu\text{m}^3$	55 GPa

IXS measurements were performed at the ID28 beamline of the ESRF [33]. The incident photon energy was set to 17.794 keV, which results in an energy

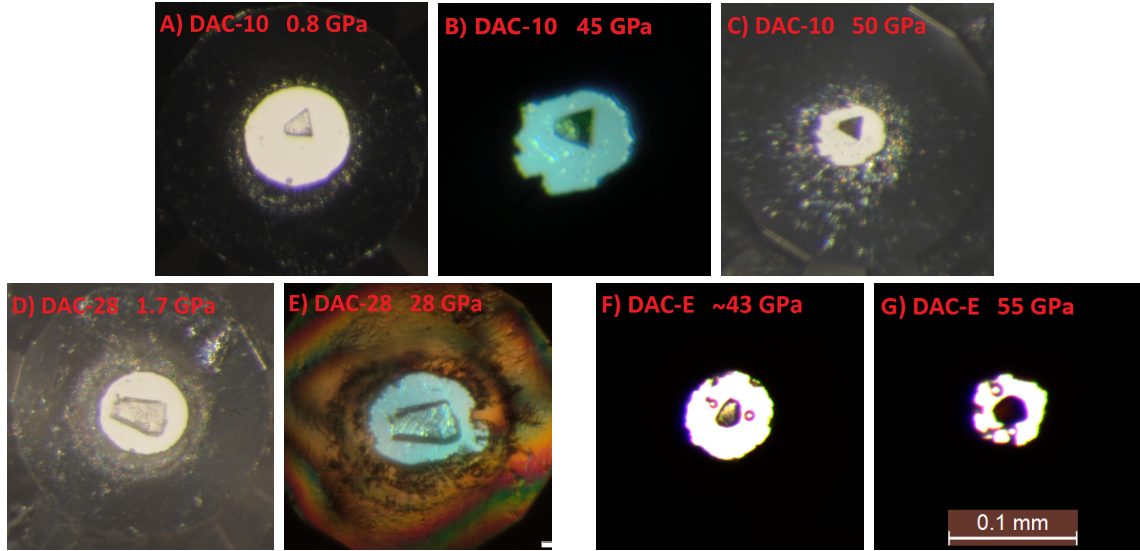


Figure 3.3: FeCO_3 single crystals loaded in diamond-anvil cells for high pressure IXS measurements. Panels A-G show samples at various pressures. Insets B and F show the crystals undergoing the spin transition, which manifests in color gradient across the sample, as reported previously [54, 67, 71]. DAC-10, DAC-28, and DAC-E denote different cells and loadings described in Table 3.1.

resolution of 3.0 meV. The X-ray beam was focused to a spot of $20 \times 30 \mu\text{m}^2$ (vertical \times horizontal) on the sample.

At each pressure point IXS spectra were measured along the Γ -T direction. By solving the Christoffel equation we determined, that the velocity of transverse phonons along this direction corresponds to the C_{44} modulus, and the velocity of longitudinal phonons to the C_{33} modulus. At 2 GPa and 15 GPa pressure points, IXS spectra were recorded around the (0012) reflection and the longitudinal phonons were observed. At 28 GPa IXS spectra were recorded around the (4 $\bar{1}$ 8) reflection, where only a transverse phonon was observed. At 55 GPa, IXS spectra were recorded around the (01 $\bar{4}$) reflection, and both longitudinal and transverse phonon excitations with similar intensities were observed. As shown by our calculations (Fig. 3.4) the acoustic phonons along the Γ -T direction have linear dispersion. Following that fact, in order to determine sound velocities, we were fitting linear dispersion relations to measured data in the vicinity of the Γ point.

3.3 Computational details

The spin-polarized density functional theory calculations were performed with the CASTEP program [75] using the generalized gradient approximation formalized by Perdew, Burke & Ernzerhof [76] with a plane wave basis set and ultra-soft pseudo-potentials from the CASTEP 8.0 database. The maximum cutoff energy of the plane waves was 750 eV. A $12 \times 12 \times 12$ Monkhorst-Pack grid [77] was em-

employed for sampling of the reciprocal space corresponding to a k-point separation smaller than $\sim 0.022 \text{ \AA}^{-1}$.

Following Hsu and Huang [63], a Hubbard U of 4 eV was employed for the d -electrons of iron. Additional calculations showed that a variation of U by 10% had only a negligible influence on the elastic stiffness coefficients. The calculations were considered to be converged once the maximal residual force acting on an atom was $< 0.01 \text{ eV/\AA}$, the residual stress was $< 0.02 \text{ GPa}$, and the maximal energy change was $< 5 \cdot 10^{-6} \text{ eV/atom}$. For the calculations of stress-strain relations used to determine the elastic tensor two strain patterns were employed in order to cross-check the results. The maximum strain amplitude was 0.003.

3.4 High-pressure elasticity of FeCO₃ and MgCO₃ from experiment and calculations

In order to get an idea on how the spin transition affects the lattice dynamics of FeCO₃ we have calculated its phonon dispersion relations at 45 GPa in the HS state and the LS state, as shown in Figure 3.4. The spin transition in FeCO₃ is associated with a jump in volume, which usually results in hardening of the phonon energies across the transition. Such typical behavior was observed for phonons with energies below 100 meV in the HS state. As the sound velocity is given by the slope of the acoustic phonons dispersions, hardening of the phonon energies will result in an increasing of sound velocities and elastic moduli.

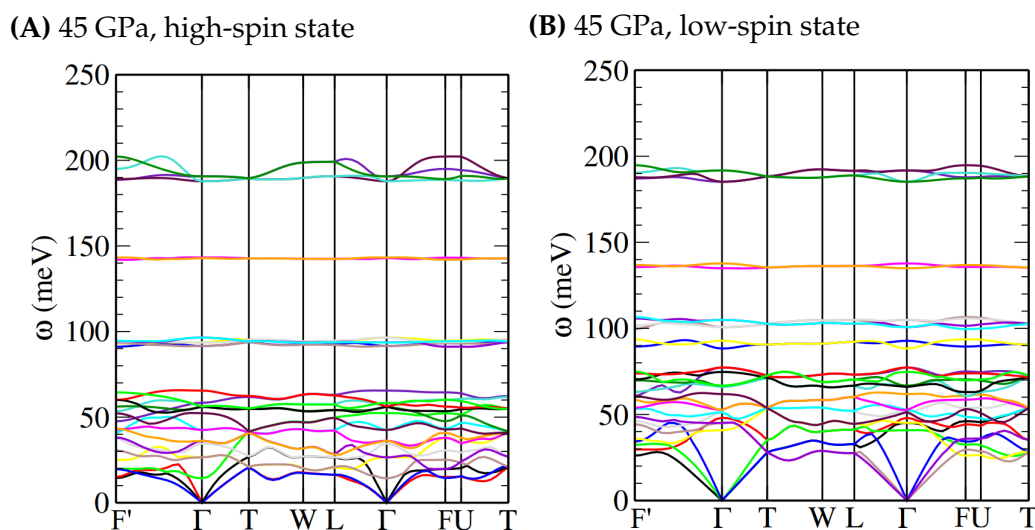
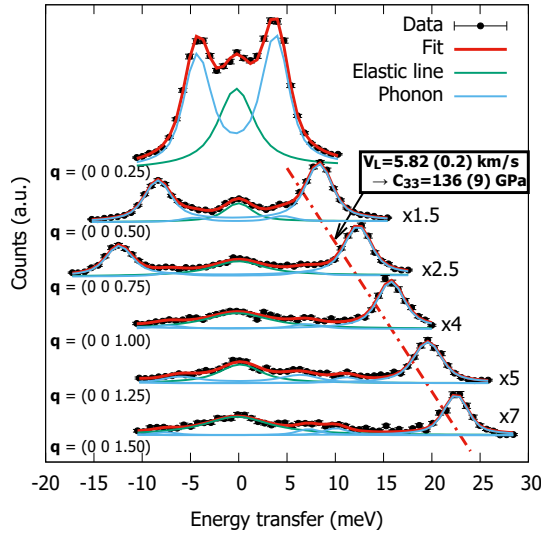


Figure 3.4: Calculated phonon dispersion relations of FeCO₃ at 45 GPa in the (A) high-spin state, and (B) low-spin state.

We have measured the IXS spectra of acoustic phonons at various pressures, as shown in Table 3.1. Figure 3.5 shows the representative high-pressure IXS

spectra collected at 2 GPa and 55 GPa. The spectra were modeled with the pyFit28 program, developed for the needs of ID28.

(A) 2 GPa



(B) 55 GPa

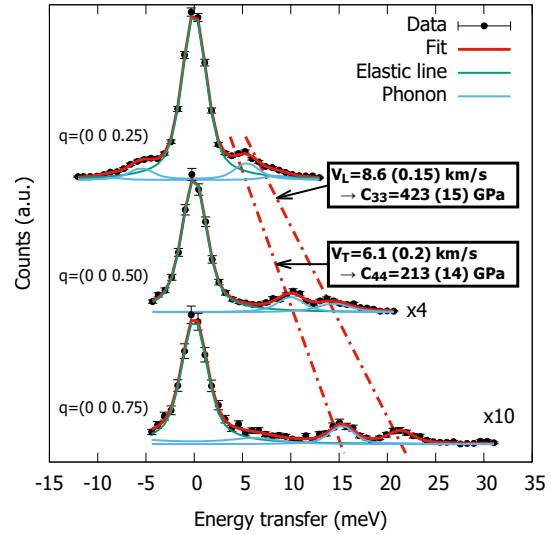


Figure 3.5: IXS spectra of FeCO_3 measured at 2 GPa (A) and 55 GPa (B) (black points) together with model spectra (red lines) obtained by fitting phonon excitations (blue lines) and elastic line (green lines). Linear dispersion relations were fitted in order to determine sound velocities (red dashed lines) and elastic moduli (see text). Some spectra were multiplied by " $\times N$ " for better comparison.

In the LS state at 55 GPa IXS spectra were recorded along various other directions, which allowed determining sound velocities, however they didn't correspond directly to elastic moduli. They were used to derive the effective elastic moduli $C = \rho V_{exp}^2$, and to compare them with calculated values, as shown in Figure 3.6.

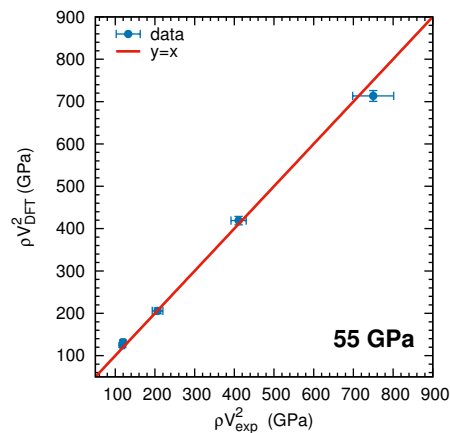


Figure 3.6: Effective bulk moduli, $C = \rho V_{exp}^2$, of FeCO_3 measured along selected directions at 55 GPa, compared to the calculated values.

Measured dispersion relations were employed to determine the C_{33} and C_{44} moduli. The complementary DFT calculations allowed determining all elastic moduli and comparing them to the measured and reported values, as presented in Figure 3.7. We observe a perfect agreement between the values measured by IXS and calculated ones. All elastic moduli increase linearly with pressure and, except for C_{12} , exhibit an abrupt increase in value across the spin transition, which is consistent with measurements of Fu et al. [55]. We did not observe any anomalous behavior, as our measurements were performed at pressures outside of the mixed-spin region, and our calculations were performed for pure spin models.

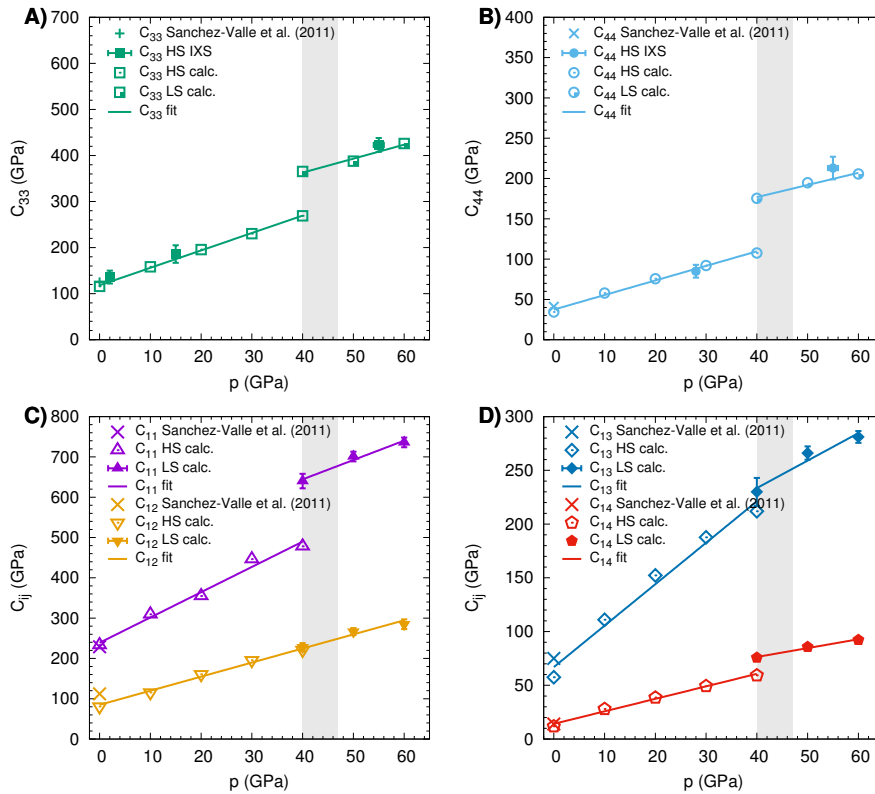


Figure 3.7: A) C_{33} , B) C_{44} , C) C_{11} and C_{12} , D) C_{13} and C_{14} elastic moduli of FeCO₃ at high pressure. Insets present data measured in this study by IXS and calculated by DFT (open and closed symbols), as well as values reported by Sanchez-Valle et al. [78] („×” symbols) at ambient pressure. Solid lines are fits to the calculated values. Shaded area indicates the pressure range of the spin transition [67]. If not shown, errors are smaller than the symbols’ size.

In the next step we have performed calculations aimed at determining the elastic tensor of MgCO₃. The results are presented in Figure 3.8, together with the values reported by Yang et al. [72]. We observe perfect agreement between these datasets, except for the C_{12} modulus. Our calculations give values that are systematically lower than the experiment by 21%, calculated as $[(C_{12}^{\text{exp}} - C_{12}^{\text{DFT}})/C_{12}^{\text{exp}}]$.

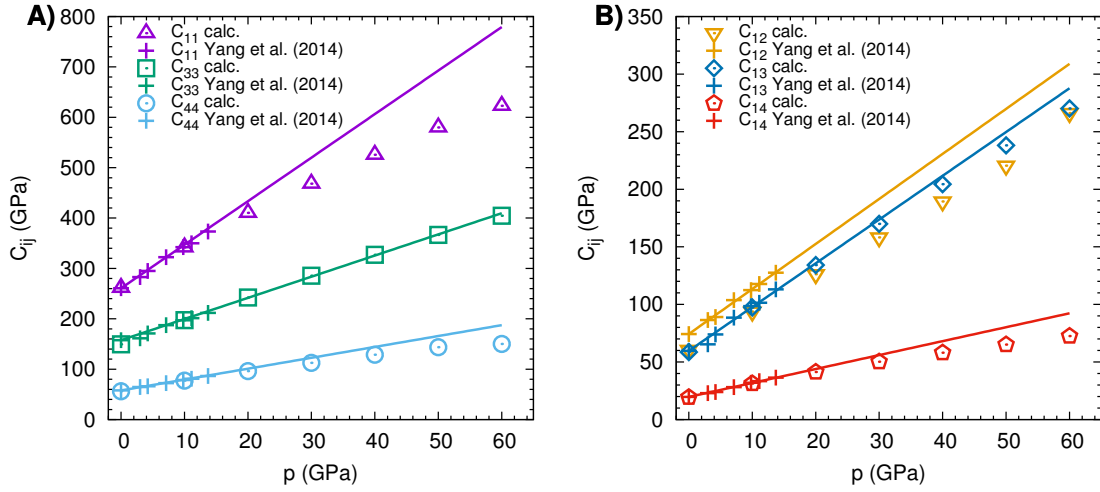


Figure 3.8: Calculated elastic moduli of MgCO_3 at high pressure (open symbols) compared to experimental data („+”) of Yang et al. [72]. Solid lines are fits to the experimental data, and visualize the non-linear behavior of some moduli. If not shown, errors are smaller than the symbols’ size.

Data of Yang et al. [72] show, that up to 14 GPa, all C_{ij} ’s depend linearly on pressure. Our calculations show that C_{33} , C_{12} and C_{13} follow the linear trend even up to 60 GPa, while C_{11} , C_{44} and C_{14} behave non-linearly above 20 GPa.

3.5 High pressure elasticity of $\text{Mg}_{1-x}\text{Fe}_x\text{CO}_3$

The dataset obtained in this study allows us to investigate the influence of the composition on the elastic properties of $\text{Mg}_{1-x}\text{Fe}_x\text{CO}_3$ carbonates at high pressures. We have combined the results of our calculations with reports on elasticity of $\text{Mg}_{1-x}\text{Fe}_x\text{CO}_3$ carbonates [55, 72, 78], in order to determine a universal function $C_{ij}(x, p)$ yielding the value for a selected modulus, ij , for a given composition, x , at a given pressure, p . The fits at selected pressures are shown in Figure 3.9, where we observed, that at a given pressure all elastic moduli vary linearly with composition, except for C_{12} . For further analysis the issue of the non-linear C_{12} was omitted, and a linear function was fitted to determine $C_{12}(x, p)$ at each pressure p , which is not shown in Figure 3.9. Such approach allowed us to determine the $C_{ij}(x, p)$ function, which is shown in form of the heat maps in Figure 3.10. It was assumed that the spin transition is sharp, i.e. no mixed-spin state, and occurs at 40 GPa. Due to the method of obtaining the C_{12} modulus described above, we observed an artifact in its value. It exhibits a jump in its value across the spin transition, which was not observed in calculations shown in Figure 3.7. Nevertheless, further analysis showed minor influence of this artifact on the sound velocities derived from this dataset.

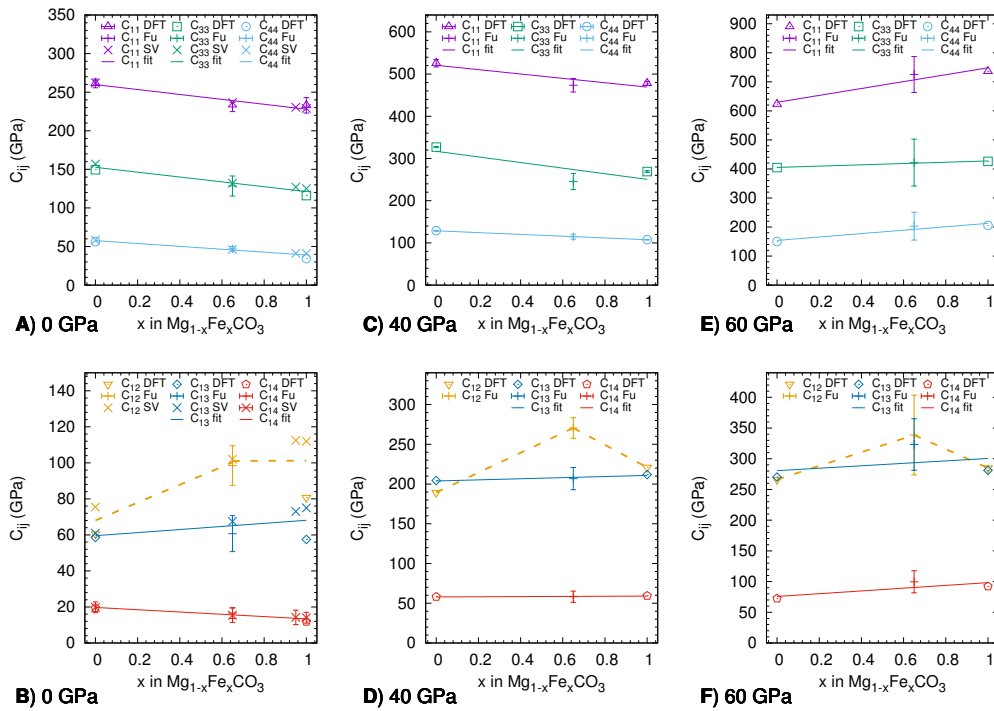


Figure 3.9: Elastic moduli of $\text{Mg}_{1-x}\text{Fe}_x\text{CO}_3$ calculated in this study and measured by other authors (Fu [55], SV [78]). Solid lines are fit to the data as described in the main text, dashed lines are guides to the eye. In panels C, D the calculated moduli correspond to the high-spin FeCO_3 phase.

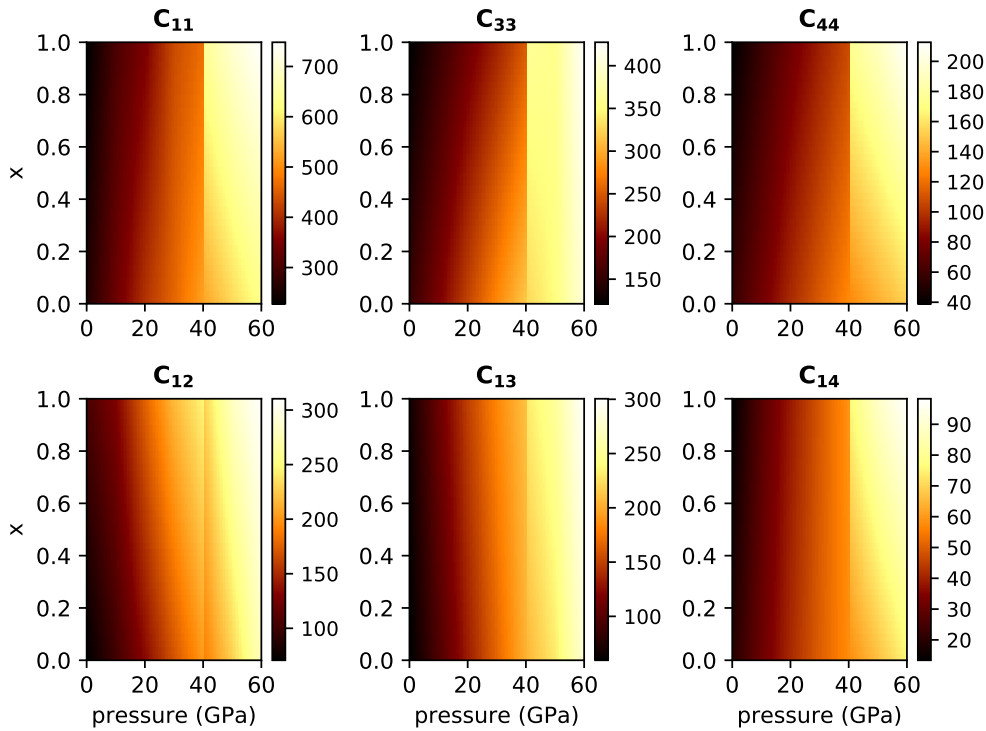


Figure 3.10: Heat-maps representing the elasticity of $\text{Mg}_{1-x}\text{Fe}_x\text{CO}_3$ carbonate for all compositions and pressures up to 60 GPa. Note the different color-scale for each modulus.

3.6 Geophysical implications

In order to determine the seismic signature of $\text{Mg}_{1-x}\text{Fe}_x\text{CO}_3$ carbonate we have computed its sound velocity, as well as velocity anisotropies, as shown in Figure 3.11. Following [79], the velocity anisotropy is defined as:

$$AV_i = 2(V_i^{\max} - V_i^{\min}) / (V_i^{\max} + V_i^{\min}). \quad (3.1)$$

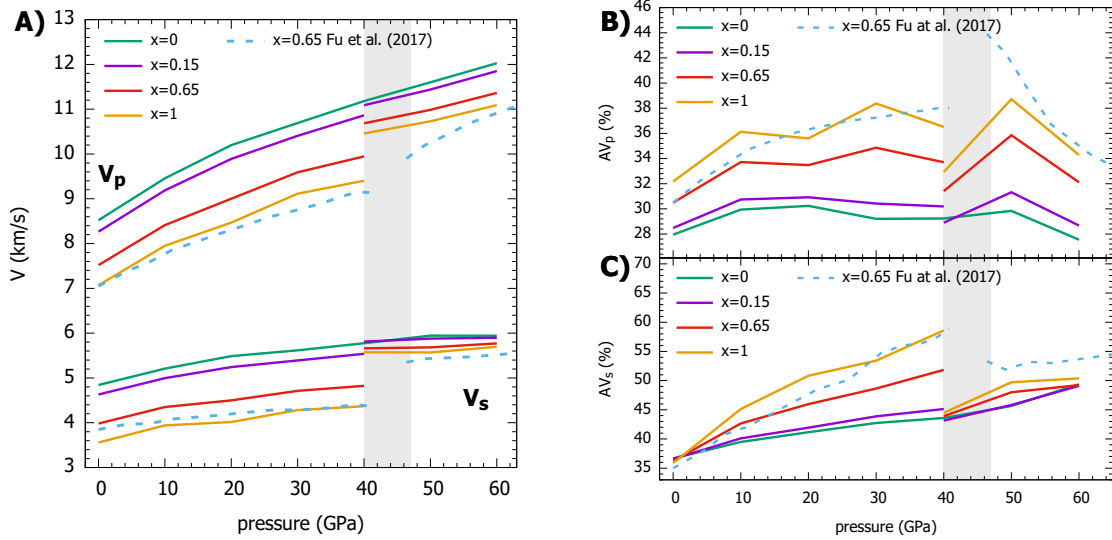


Figure 3.11: A) Mean sound velocities of $\text{Mg}_{1-x}\text{Fe}_x\text{CO}_3$ carbonate with different composition, as well as velocity anisotropies of compressional (B) and shear (C) waves. Solid lines denote values determined in this study, the dashed line shows the values measured by Fu et al. [55] for $\text{Mg}_{0.35}\text{Fe}_{0.65}\text{CO}_3$. Green line shows values for MgCO_3 , purple solid line for potential deep mantle carbonate, $\text{Mg}_{0.85}\text{Fe}_{0.15}\text{CO}_3$, red solid line for $\text{Mg}_{0.35}\text{Fe}_{0.65}\text{CO}_3$ studied by other authors [55, 78], and yellow solid line for FeCO_3 . The data from the mixed-spin region (shaded area) reported by Fu et al. [55] was omitted for clarity, see Figure 3.2.

Results presented on Figure 3.11 show, that the sound velocity decreases with decreasing iron content over the chosen pressure range. There is a significant difference in sound velocities between the HS and the LS FeCO_3 . We observed, that the relative difference in sound velocities before and after the spin transition: $\delta V_i = [(V_i^{\text{LS}} - V_i^{\text{HS}}) / V_i^{\text{HS}}]$ changes linearly with iron content, x . For the hypothetical deep mantle carbonate, $\text{Mg}_{0.85}\text{Fe}_{0.15}\text{CO}_3$, the relative difference in sound velocities before and after the spin transition is 2% for V_p and 5% for V_s , where for pure iron carbonate, FeCO_3 the difference is 11% for V_p and 28% for V_s .

The sound velocity anisotropies seem to have an opposite trend to the sound velocity. Firstly, the anisotropy increases with increasing iron content over the investigated pressure range. Secondly, the anisotropy decreases across the spin transition. The shear wave anisotropy is affected more by the spin transition than

the compressional wave anisotropy. For FeCO₃ the AV_s drops by 24% across the spin transition, while for the Mg_{0.85}Fe_{0.15}CO₃ by less than 1%.

We consider the relative velocity change, as such quantity can be evaluated from seismic tomography measurements, as shown in Figure 1.2. Based on such studies we assume, that the limit of detectability is 1% of the relative velocity change. This limit provides a constrain on how much Mg_{1-x}Fe_xCO₃ is necessary to be in the mantle to provide a significant velocity contrast. We have employed the BurnMan package [80], in order to calculate the mean velocity of a chosen rock assemblage at given p, T conditions. We considered a model of pyrolitic mantle, as proposed by Wang et al. [81], with 80% of iron-bearing bridgmanite (95% MgAlO₃ and 5% FeAlO₃), 20% ferropericlase (82% MgO and 18% FeO) and we were varying the amount of carbonate Mg_{1-x}Fe_xCO₃ with different compositions, x . The necessary physical properties, such as bulk modulus and density, together with their pressure and temperature derivatives, were taken for bridgmanite and ferropericlase from Stixrude and Lithgow-Bertelloni [82]. For Mg_{1-x}Fe_xCO₃ the current dataset allows calculating these properties without their temperature derivatives. The temperature corrections for elastic moduli were taken as for magnesite from [72], and for density from Dorogokupets [83]. Such approach allows us to investigate the mean velocity profile in the upper part of the lower mantle, that is at pressures 30–60 GPa along the geotherm, which corresponds to depths of 700–1450 km, according to the PREM model [84].

In the following sections we investigate the effect of the spin transition on the detectability of the carbonate. Next we examine how does the presence of carbonate influence the sound velocity of a pyrolitic mantle assemblage. Lastly, we look into the velocity anisotropies of the carbonate, to understand their relatively high values.

3.6.1 Effect of the spin transition on the detectability of Mg_{1-x}Fe_xCO₃ in the mantle

First we investigated the effect of spin transition on the velocity contrast, where a detectability constrain is a 1% change in relative sound velocity. As shown in Figure 3.11 this contrast is small for deep mantle carbonate Mg_{0.85}Fe_{0.15}CO₃, and in the pyrolitic mantle assembly at least 24% of total volume of the carbonate is necessary to detect the contrast in shear velocity, and 50% in the compressional velocity. For pure FeCO₃ at least 4% volume would give a significant V_s contrast, and 10% for V_p .

The arising question is, whether it is possible for such concentrations of carbonate to be present in the mantle. We do know, that the mantle is not homogeneous, it has regions with hotter, lower in density plumes, and colder, higher in

density subducting slabs. There could exist a carbonate-rich region somewhere in the mantle. The size of that region would need to be bigger than the spatial resolution of the tomographic measurements, estimated to be around 40 km.

However, our models assume, that the spin transition is sharp, i.e. occurs across a very narrow pressure range of around 1 GPa. The studies of Lin et al. [85] and Müller et al. [56] showed, that this assumption is not correct for ferromagnesite, with compositions $\text{Mg}_{0.35}\text{Fe}_{0.65}\text{CO}_3$ and $\text{Mg}_{0.74}\text{Fe}_{0.26}\text{CO}_3$, where at 1400 K the spin transition progresses over the pressure range of 10–15 GPa. Thus, the concentrations presented in the first paragraph are optimistically only the lower bounds of detectability.

Additionally, in the pyrolitic assemblage iron is incorporated in bridgmanite and periclase as well. Since in both of them iron is octahedrally coordinated by six oxygens, like in iron carbonate, they will also undergo a spin transition, at pressures between 40 GPa and 50 GPa at ambient temperature [69, 70]. The conclusion is, that the spin transition will occur in the whole assemblage, and is not unique for iron carbonate.

The studies on ferropericlase $\text{Mg}_{0.83}\text{Fe}_{0.17}\text{O}$ by Antonangeli et al. [70] have already questioned the effect of the spin transition on the velocity contrast, with similar conclusions as above, calling the transition „transparent“, i.e. not possible to be observed in seismic measurements. This, and other similar studies were a motivation for the current study, in hope to discover a unique effect of the spin transition on seismic velocities.

We conclude that the spin transition has a small effect on the deep mantle carbonate, $\text{Mg}_{0.85}\text{Fe}_{0.15}\text{CO}_3$, and a significant contrast in sound velocities could be observed only in regions of the mantle which are rich in iron carbonate.

3.6.2 Effect of the presence of $\text{Mg}_{1-x}\text{Fe}_x\text{CO}_3$ on the velocity profile of the mantle

As the spin transition does not seem to provide a significant seismic signature for the lower mantle carbonate, we examine how does the presence of carbonate change the mean velocity of a pyrolitic assemblage in the lower mantle.

The extrapolation of our data to lower mantle conditions shows, that the sound velocities propagating in carbonate are lower than that in pyrolite. In order to decrease the shear velocity of carbonated pyrolite by 1%, a concentration of 10% of $\text{Mg}_{0.85}\text{Fe}_{0.15}\text{CO}_3$ is necessary, while the same effect for compressional velocity requires 9% of $\text{Mg}_{0.85}\text{Fe}_{0.15}\text{CO}_3$. As the sound velocities decrease with increased iron content in the carbonate (see Fig. 3.11), smaller amounts of iron-rich carbonate are necessary to obtain the same change in sound velocities.

This shows, that carbonate-rich regions in the mantle with concentrations around 10%, could significantly reduce the aggregate sound velocities.

3.6.3 Velocity anisotropies of Mg_{1-x}Fe_xCO₃

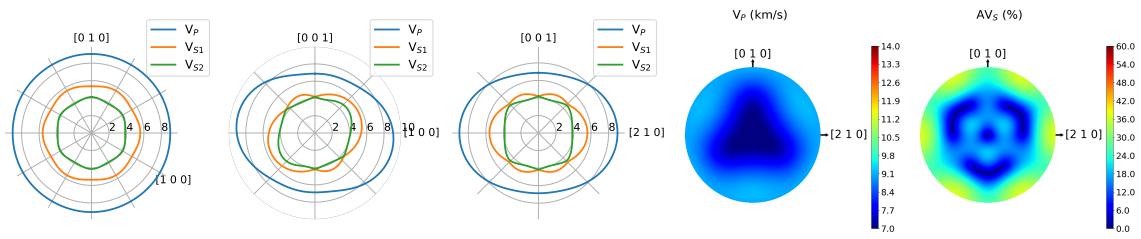
The interesting property of sound propagation in carbonates is its high anisotropy, which originates from the symmetry of the crystal structure. Sanchez-Valle et al. [78] pointed out that this might provide an additional seismic signature for carbonates, by employing the shear wave splitting tomography.

Our data shows, that the anisotropy of the compressional waves in Mg_{1-x}Fe_xCO₃ remains approximately constant in the studied pressure range. It is relatively high, 29% for MgCO₃, and 35% for FeCO₃. The spin transition seems to have negligible impact on the AV_p of iron carbonate. The shear wave anisotropy is even higher, and increases with pressure. Interestingly, after the spin transition the shear anisotropy is similar for all compositions of the Mg_{1-x}Fe_xCO₃ carbonate.

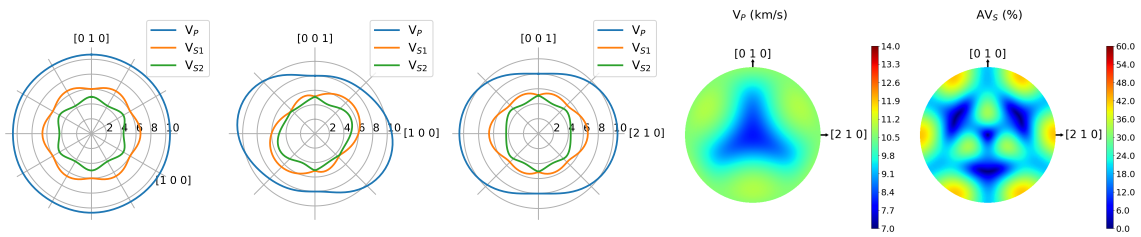
In order to understand the character of the velocity anisotropy in lower mantle carbonate, we have computed the sound velocities along selected directions, see Figure 3.12. The pole figure of V_p shows that the high anisotropy of the compressional velocity originates from the fact, that this wave propagates fast within the ab plane, and slower along the c axis. Up to 60 GPa the V_p is the same for all directions within the ab plane, and the spin transition does not affect its anisotropy, as was already concluded from Figure 3.11.

On the other hand, the splitting of shear wave velocities is high, anisotropic, and increases remarkably with pressure, up to 60 GPa. Again, the spin transition has negligible effect on shear velocities. At elevated pressures the AV_s has global maxima along the $\langle 210 \rangle$ directions, and local maxima along the directions corresponding within few degrees to the Fe/Mg–O bond, which is roughly along the normal of the (104) plane.

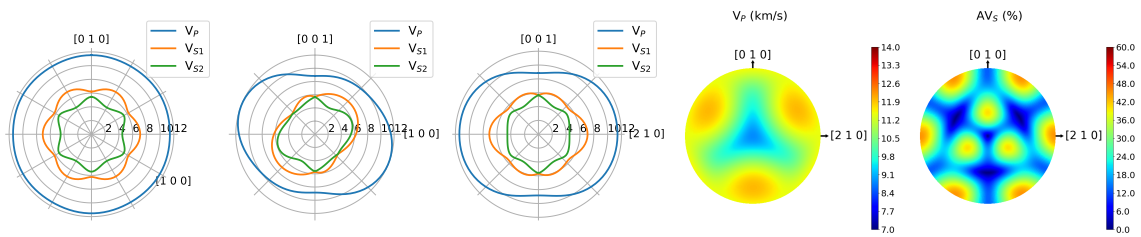
(A) 0 GPa



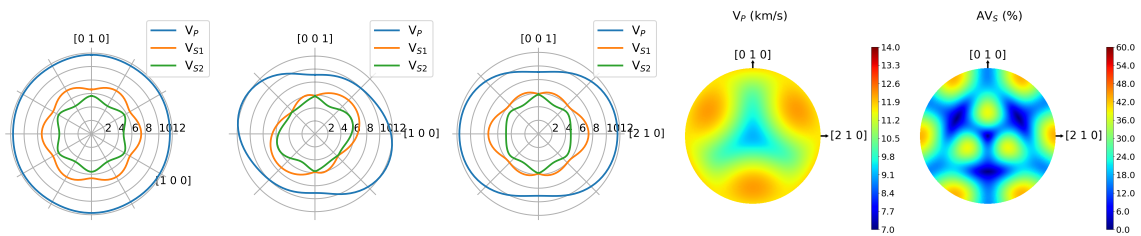
(B) 20 GPa



(C) 40 GPa high-spin state



(D) 40 GPa, low-spin state



(E) 60 GPa

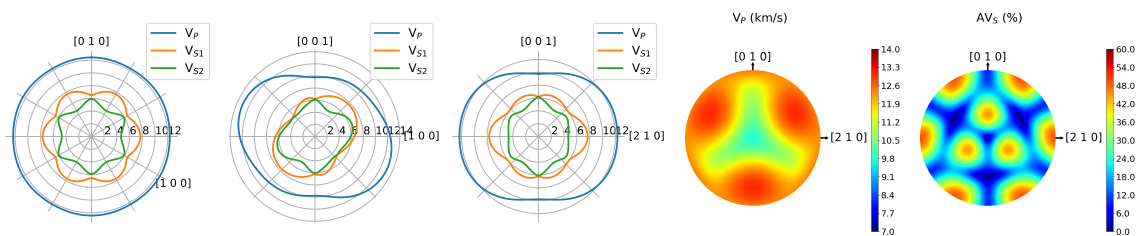


Figure 3.12: Sound velocities (from first to fourth column) and shear wave splitting (fifth column) of the lower mantle carbonate $\text{Mg}_{0.85}\text{Fe}_{0.15}\text{CO}_3$. Fourth and fifth column present the pole figures of V_p and AV_s , respectively, with the $[001]$ direction (c axis) in the center of a circle, pointing to the viewer. All velocities are given in km/s.

3.7 Conclusions

In this chapter we have combined the experimental and computational approach to determine the elastic properties of iron carbonate and magnesium carbonate at high pressure. We have combined the obtained values with the reported ones, to interpolate the high-pressure elastic properties for compositions in between the iron and magnesium end-members.

Our main goal was to determine the influence of spin-transition in iron carbonate on its elastic properties. We have shown that the spin transition significantly increases the elastic stiffness moduli and the sound velocities. However, extrapolation of these results to the lower mantle condition, i.e. high temperature and high pressure, shows, that due to the fact that at high temperature the spin transition progresses over a wide pressure range, the stiffness increase would not provide a significant contrast in sound velocities. We have discussed other possible methods for detecting the carbonates in the lower mantle, with focus on high anisotropy of shear velocities.

4

High-pressure F -point instabilities in carbonates

In order to construct geophysical models of the Earth's interior, it is crucial to determine which minerals are stable at given conditions, and what are their physical properties. This starts with the construction of a phase diagram of a given mineral, and afterwards, determination of physical properties of each phase. Currently, a lot of research is focused on studying the phase transitions of minerals at high pressures and temperatures, as they can abruptly change their physical properties. These can be incorporated into the models and by comparison to experimental observations the geophysical phenomena can be understood.

In case of carbonates there is a huge difference in the complexity of the phase diagram of calcium and magnesium carbonate, even though they are isostructural at ambient conditions. Up to 50 GPa ten different crystalline phases of calcium carbonate were reported [86], while magnesite undergoes only one phase transition to magnesite-II, occurring at 115 GPa and over 2000 K [87]. This difference motivated us to investigate the lattice dynamics of calcite and magnesite, as their phase transitions could have origins in vibrational instabilities. Indeed, some theoretical investigations suggest that the transition from calcite to calcite-II is driven by a soft phonon [88], as well as the transition from dolomite to dolomite-II [89]. However, these suggestions were lacking experimental evidence.

This chapter shows the results of a high-pressure lattice dynamics investigation focused on calcite, dolomite, and magnesite, with additional ambient pressure measurements of siderite, smithsonite, and otavite. The data was obtained by combining TDS and IXS measurements with DFT based calculations. It shows, that the F -point phonon anomaly in calcite is responsible for the transition to calcite-II. A softening of the same phonon was observed in dolomite, suggesting that it is also driving the transition to dolomite-II. No such anomaly was observed in magnesite. These observations shed light on the physical phenomena governing the phase transitions in calcite, dolomite and magnesite, and allow for deeper understanding of their stability fields.

4.1 Introduction

The comparison of the phase diagrams of calcite, dolomite, and magnesite presented in Figure 4.1 shows, that although they are structurally similar they behave very differently at gigapascal pressures. One can see, that up to 50 GPa calcite has ten different polymorphs, dolomite four, and magnesite only one. At ambient conditions calcite and magnesite crystallize in the calcite structure, with $R\bar{3}c$ space group, characterized by alternate layers of cations and trigonal, planar carbonate groups, CO_3^{2-} . The cations are coordinated by six oxygens in a regular, octahedral formation. In dolomite the cationic layers are alternating between calcium and magnesium atoms, which results in lowering the symmetry of the crystal structure to the $R\bar{3}$ space group. Crystal structures of these carbonates are presented in Figure 4.2.

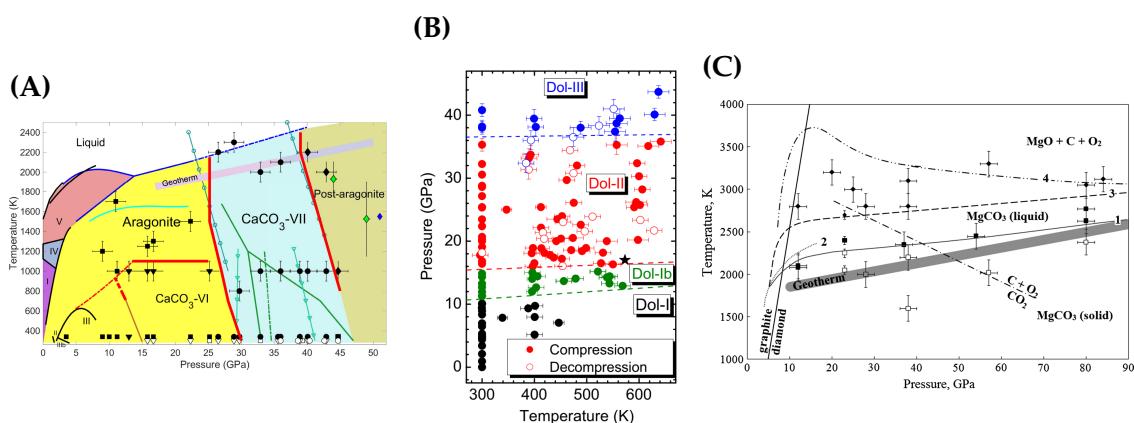


Figure 4.1: Phase diagrams of calcite (A) from Bayarjargal et al. [86] (2018), dolomite (B) from Efthimiopoulos et al. [90] (2017), and magnesite (C) from Solopova et al. [91] (2015).

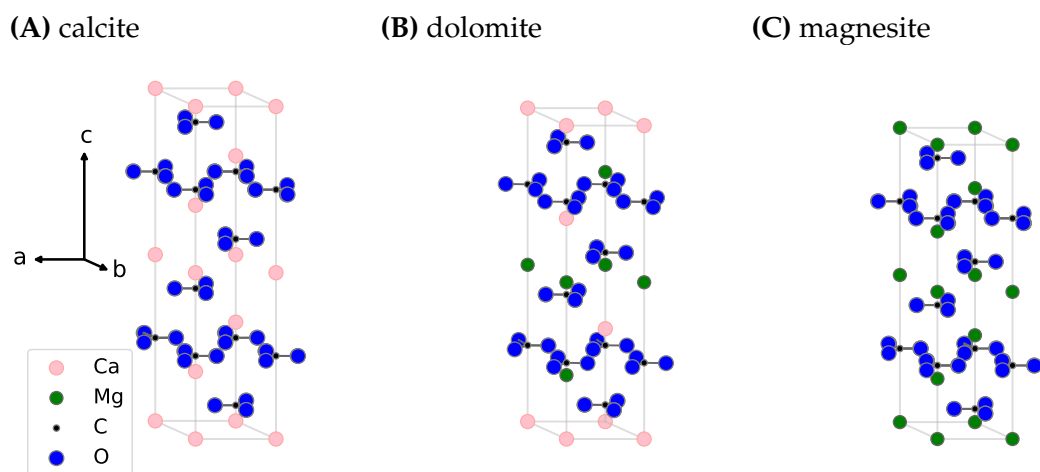


Figure 4.2: Crystal structures of calcite (A), dolomite (B), and magnesite (C). The hexagonal axes, as well as the legend describing the coloring of the atoms, is shown on the left-hand side.

As the stability fields of carbonates are currently a matter of intense study, the phase diagrams of dolomite and magnesite shown in Figure 4.1 do not fully depict the current state of knowledge. The first important addition is the phase transition in magnesite, which heated above 2000 K at 115 GPa transforms to presumably orthorhombic magnesite-II, reported by Isshiki et al. [87]. A number of theoretical investigations report on the possible structure of magnesite-II, as summarized in Oganov et al. [92]. It is believed that it possesses tetrahedrally coordinated carbonate groups, as observed at these conditions in calcite [93], iron-rich dolomite ($\text{Ca}(\text{Mg}_{0.6}\text{Fe}_{0.4})(\text{CO}_3)_2$) [94], and magnesiosiderite ($\text{Mg}_{0.25}\text{Fe}_{0.75}\text{CO}_3$) [95]. The second matter is a clarification of the reported structures and their names in dolomite. In 2012 Merlini et al. [96] published their findings on high pressure stability of iron-rich dolomite, $\text{Ca}(\text{Mg}_{0.6}\text{Fe}_{0.4})(\text{CO}_3)_2$, and found that at 17 GPa dolomite transforms to dolomite-II, and further at 35 GPa to dolomite-III. In a following study on pure dolomite, $\text{CaMg}(\text{CO}_3)_2$ (Merlini et al. [94] 2017), they discovered that iron-free dolomite behaves slightly different under pressure. It adapts the same dolomite-II structure, however, at 35 GPa it transforms to dolomite-IIIc, which is different to the previously reported dolomite-III.

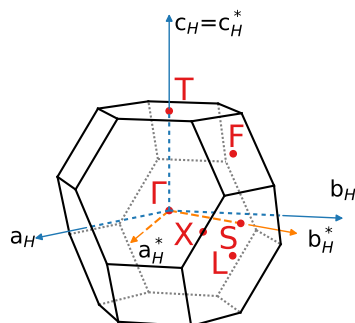


Figure 4.3: Brillouin zone of rhombohedral carbonates. The hexagonal basis vectors of the real and reciprocal space are shown with blue and orange arrows, respectively. The special points with their labels are shown in red.

The connection between the phase stability of carbonates and lattice dynamics comes from two theoretical studies. In the first one, Hatch and Merrill [88] performed a symmetry analysis of the calcite \rightarrow calcite-II transition, concluding that the displacement of the atoms transforms according to the irreducible representation of the F -point in the BZ, see Figure 4.3. This suggests, that the transition is driven by a soft phonon with the F -point wave vector, and the displacement pattern as the one defined by the displacement of the atoms due to the transition. In the second study, Zucchini et al. [89] computed the pressure dependence of the F -point phonons' energies, finding a soft phonon, whose energy decreases to zero at 17 GPa. They did not compute the eigenvector of the soft-phonon for a

direct comparison with the data of [96], and concluded, that the presence of the soft-phonon is related to the transition to dolomite-II. Given the similarities between the calcite-II and dolomite-II structures, we speculated that the underlying mechanism of these transition is the same and decided to investigate the lattice dynamics of these compounds at high pressure.

Previous experimental reports on lattice dynamics of calcite [97, 98] show an anomaly in the transverse acoustic, TA, Γ - F phonon branch, which results in the low-energy phonon at the F point of the Brillouin zone. Without further high pressure measurements the authors concluded that this anomaly precipitates the transition to the calcite-II phase. In addition, they have observed that the phonon softens with temperature, faster than accounted by the thermal expansion of the lattice. These results motivated us to thoroughly investigate the F -point anomaly at extreme conditions.

Driven by the will of providing direct experimental evidence, we have performed high pressure IXS measurements on calcite and dolomite in order to determine the pressure dependence of the soft F -point phonon. We have also measured the energy of the TA F -point phonons in magnesite and smithsonite at ambient conditions. These were preceded by TDS measurements, which allowed to determine the regions of reciprocal space with high intensity of the soft phonon. Additionally, in order to determine the displacement pattern we have performed DFT based calculations on a variety of carbonates. The combination of these methods allowed us to fully determine the lattice dynamics of calcite, dolomite and magnesite, and shed light on the mechanism of the transition to the calcite-II structure in carbonates.

4.2 Summary of the experimental methods

We have conducted a number of experiments on a variety of rhombohedral carbonates, in order to investigate the F -point instability. Table 4.1 summarizes the methods employed to investigate chosen carbonates.

Table 4.1: Summary of methods used to investigate lattice dynamics of carbonates.

	cation	Γ - F branch by IXS	TDS	DFT
calcite	Ca	up to 1.4 GPa	✓	✓
dolomite	Ca _{0.5} Mg _{0.5}	up to 7 GPa	✓	✓
magnesite	Mg	ambient P	✓	✓
siderite	Fe	×	✓	✓
smithsonite	Zn	ambient P	✓	✓
otavite	Cd	×	×	✓

A variety of samples were prepared for the TDS and IXS measurements, with the details explained below. After obtaining a crystal of appropriate size it was etched in H_2O – HCl solution, in order to reduce the contamination and roughness of the surface.

Calcite, CaCO_3

The experiments on calcite were conducted on samples cleaved from a centimeter sized single-crystal mineral of unknown origin. The analysis of single-crystal diffraction data shows, that the possible iron or magnesium impurities don't exceed 1% of cation concentration. For the TDS measurements and ambient pressure IXS measurements, an elongated sample of approximate dimensions $0.5 \times 0.5 \times 2 \text{ mm}^3$ was used. For the high pressure IXS experiment a platelet with (104) face and dimensions $120 \times 80 \times 60 \mu\text{m}^3$ (width \times height \times thickness) was loaded in the Boehler-Almax type diamond-anvil cell with $350 \mu\text{m}$ diameter culet, as shown in Figure 4.4A. A mixture of 4:1 ratio methanol-ethanol filled the sample chamber as a pressure medium, two rubies were loaded for pressure determination, a stainless steel gasket was used to contain the sample chamber.

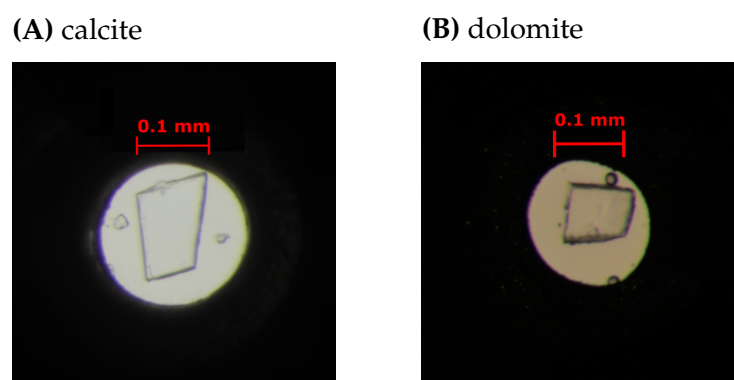


Figure 4.4: (A) calcite and (B) dolomite single-crystals loaded in the diamond-anvil cells for the high pressures IXS measurements.

Dolomite, $\text{CaMg}(\text{CO}_3)_2$

As for calcite, samples of dolomite were cleaved from centimeter size single-crystal mineral characterized in detail in Heinrich et al. [99]. They possess negligible impurities of iron, resulting in a formula $\text{CaMg}_{0.98}\text{Fe}_{0.02}(\text{CO}_3)_2$. For the TDS measurements and ambient pressure IXS measurements a sample with approximate dimensions $0.5 \times 0.5 \times 2 \text{ mm}^3$ was used. For high-pressure IXS measurements a platelet with (104) face and dimensions $100 \times 100 \times 30 \mu\text{m}^3$ (width \times height \times thickness), was loaded in a diamond-anvil cell the same way as described for calcite, shown in Figure 4.4B.

Magnesite, MgCO_3 ; siderite, FeCO_3 ; smithsonite, ZnCO_3

Single crystals of magnesite, siderite, and smithsonite were synthesized from powders at high pressures and temperatures in the multi-anvil apparatus, described in detail by Chariton [100]. The crystals were approximately spherical, with diameter up to $100\ \mu\text{m}$. Optically transparent crystals with diameter around $40\ \mu\text{m}$ were selected under the polarized microscope for TDS and IXS measurements, however their quality was visibly inferior to the calcite and dolomite samples.

TDS measurements

TDS measurements were conducted at the side station diffractometer of the ID28 beamline at the ESRF. The methodology and more details are provided in section 2.2.2 and in Girard et al. [37]. All measurements were performed with a wavelength of $0.6968\ \text{\AA}$, and a beam spot of $50 \times 30\ \mu\text{m}^2$ on the sample. The sample to detector distance was set to $244\ \text{mm}$, χ angle was -45° , single frames were obtained by performing a full ϕ scan with 0.1° step size in two runs, one with the incoming beam–detector angle Γ set to 19° , and the second run with $\Gamma=48^\circ$, in order to cover larger volume in reciprocal space. The integration time depended on the sample size, e.g. $4\ \text{s}$ for the small magnesite crystal and $1\ \text{s}$ for the big calcite crystal.

IXS measurements

IXS measurements were performed at the ID28 main station spectrometer at the ESRF [33]. For the optimal intensity to resolution ratio the incoming energy of $17.794\ \text{keV}$ was chosen which results in the energy resolution of $3\ \text{meV}$. For the experiments on calcite and dolomite the beam was focused with the multilayer mirror to a $25 \times 60\ \mu\text{m}^3$ (horizontal \times vertical) spot on the sample, for other samples, as well as the high-pressure experiments the beam was focused with Kirkpatrick-Baez mirrors to a spot $20 \times 10\ \mu\text{m}^2$.

Computational details

The CASTEP program [75] was used to perform the DFT calculations, employing the generalized gradient approximation formalized by Wu and Cohen [101], with a plane wave basis set and "on the fly" generated norm-conserving pseudo-potentials from the CASTEP database. The maximum cutoff energy of the plane waves was $880\ \text{eV}$. An $8 \times 8 \times 8$ Monkhorst-Pack grid [77] was used for sampling the reciprocal space, corresponding to a k-point separation smaller than $\sim 0.03\ \text{\AA}^{-1}$.

DFT geometry optimization calculations were considered to be converged once the maximal residual force acting on an atom was smaller than $0.01 \text{ eV}/\text{\AA}$, the residual stress was smaller than 0.02 GPa , and the maximal energy change was smaller than $5 \cdot 10^{-6} \text{ eV/atom}$.

In order to simulate the TDS maps we have used the open-source ab2tds software [102]. The input for the ab2tds is the *phonon* file generated by CASTEP, which contains the energies and eigenvectors of phonons with selected wave vectors. In order to get rid of computational artifacts the optimal choice is a uniform sampling of half of the Brillouin zone, e.g. $k_z > 0$, and omitting the BZ edges.

4.3 TDS and IXS measurements on carbonates at ambient conditions

The measured and simulated TDS maps of the prominent (H0L) plane in reciprocal space are presented in Figure 4.5. Full post-processing was employed, as described in section 2.2.2. The arrows are pointing at the $(-2.5 \ 0 \ 2)$ *F*-point. In calcite and dolomite we observed diffuse scattering intensity in between Bragg reflections, with smooth profile, indicating its phonon origin. The signal is strongest along the line between $(-3 \ 0 \ 0)$ and $(0 \ 0 \ 12)$ reflections, or between $(-6 \ 0 \ 0)$ and $(0 \ 0 \ 24)$ reflections. Upon closer inspection, weak intensity of similar characteristic can be observed in smithsonite, between Bragg reflections on the $(-6 \ 0 \ 0) \rightarrow (0 \ 0 \ 24)$ line. No such intensity was observed in magnesite or siderite. The siderite crystal had a non-merohedral twin, resulting in additional Bragg reflections in non-integer positions. The maps reconstructed from DFT calculations excellently reproduce the measured DS intensity, indicating that the calculated eigenvectors are accurate.

In the next step we have conducted IXS measurements in order to determine the dispersion of the soft TA phonon in the Γ -*F* branch at ambient conditions. The heat-maps shown in Figure 4.6 show the measured IXS spectra compared and calculated dynamic structure factor (see equations 2.14 and 2.18) for calcite, dolomite, magnesite and smithsonite. In the experimental maps the intensities in between measured *Q* points were interpolated, in order to facilitate a comparison with the calculated maps. However, such approach can produce artifacts in the data, such as „islands” of intensity, when a large step in reciprocal space is adapted, see the data for magnesite. Nevertheless, we observe perfect agreement between the measured and calculated intensities, which proves the reliability of our calculations.

Finally we have extracted the phonon energies from the experimental data to determine the dispersion of the transverse acoustic phonons, and compared

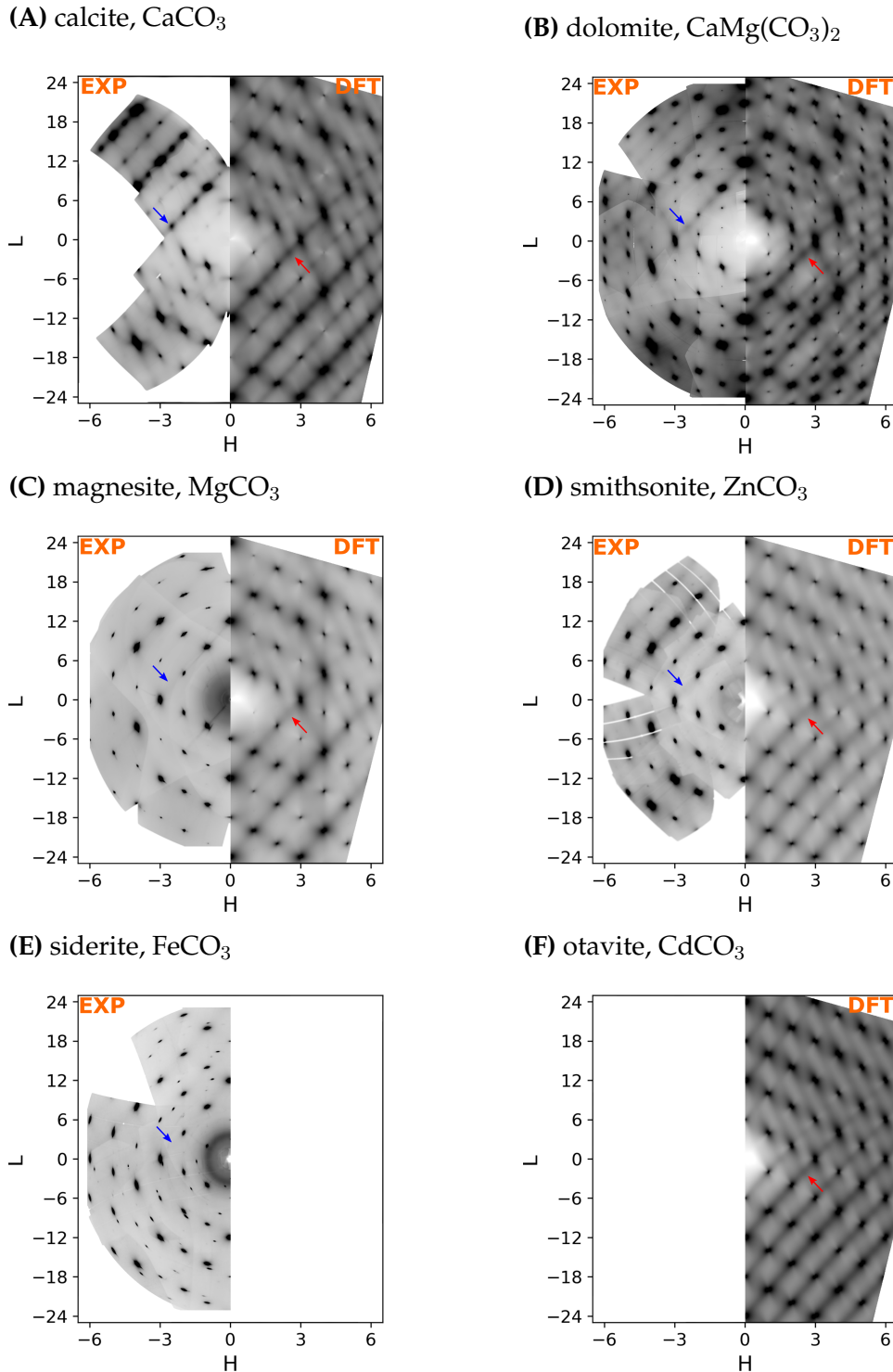


Figure 4.5: Diffuse scattering signal reconstructed on the (H0L) plane of various carbonates measured at the side-station of ID28 (left parts, marked with EXP) and reconstructed from DFT calculations (right parts, marked with DFT). DFT based reconstruction was not possible for siderite (E), as adequate calculations were not performed. Measurements for otavite (F) were not possible, as crystals were not available. Blue arrows point at the measured, and red arrows at the calculated intensity of the $(-2.5\ 0\ 2)$ F -point. Reciprocal space maps are centrosymmetric.

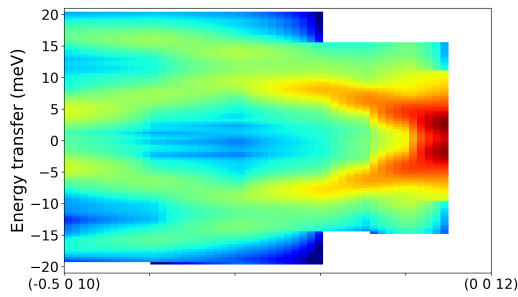
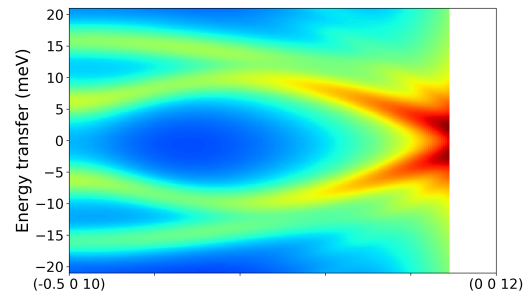
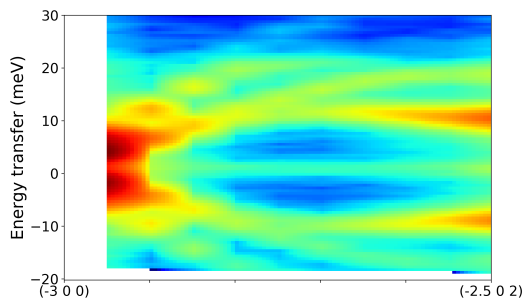
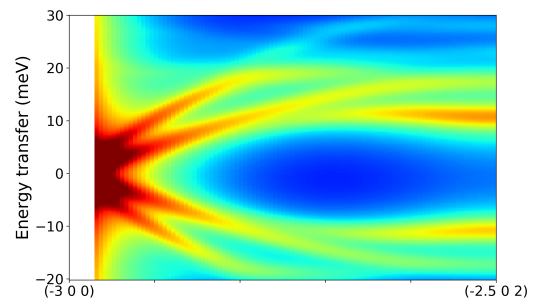
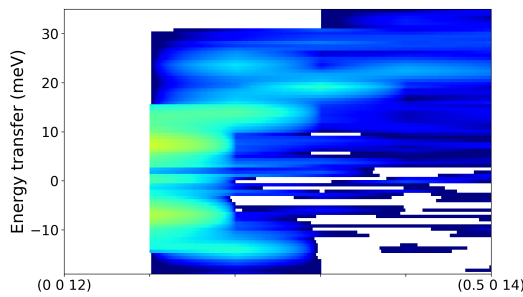
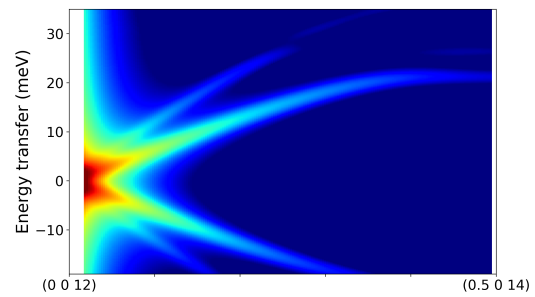
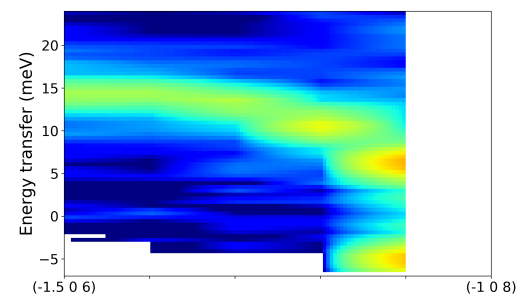
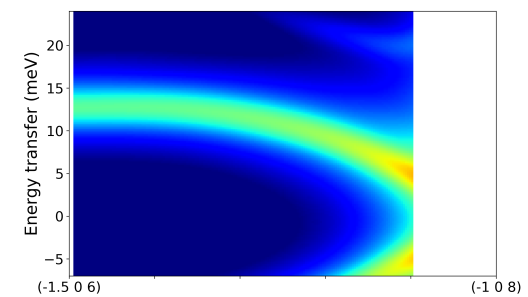
(A) calcite, CaCO_3 , IXS**(B)** calcite, CaCO_3 , DFT**(C)** dolomite, $\text{CaMg}(\text{CO}_3)_2$, IXS**(D)** dolomite, $\text{CaMg}(\text{CO}_3)_2$, DFT**(E)** magnesite, MgCO_3 , IXS**(F)** magnesite, MgCO_3 , DFT**(G)** smithsonite, ZnCO_3 , IXS**(H)** smithsonite, ZnCO_3 , DFT

Figure 4.6: Measured (left column) and calculated (right column) IXS spectra of calcite, dolomite, magnesite and smithsonite (see labels descriptions) along the Γ - F branch. The color scale in a sequence brown-red-yellow-green-blue corresponds to regions from high to low intensity.

them to the calculated values, as presented in Figure 4.7. In addition we have calculated the dispersion curves for siderite and otavite, to determine the influence of the cation substitution on the phonon energies. Along the Γ - F direction the transverse acoustic phonons are non-degenerate and we label them as TA and TA'. We label the anomalous branch in calcite as TA and plot it with a solid line. For other carbonates, we investigate the displacement pattern of the phonons along both transverse acoustic branches, and the label TA is put on the branch that resembles more the TA phonon in calcite. The IXS measurements show an anomalous dispersion of the Γ - F branch in calcite and dolomite, where the branch softens upon approaching the BZ boundary at the F -point. Typical, sinusoidal dispersion was observed in magnesite and smithsonite.

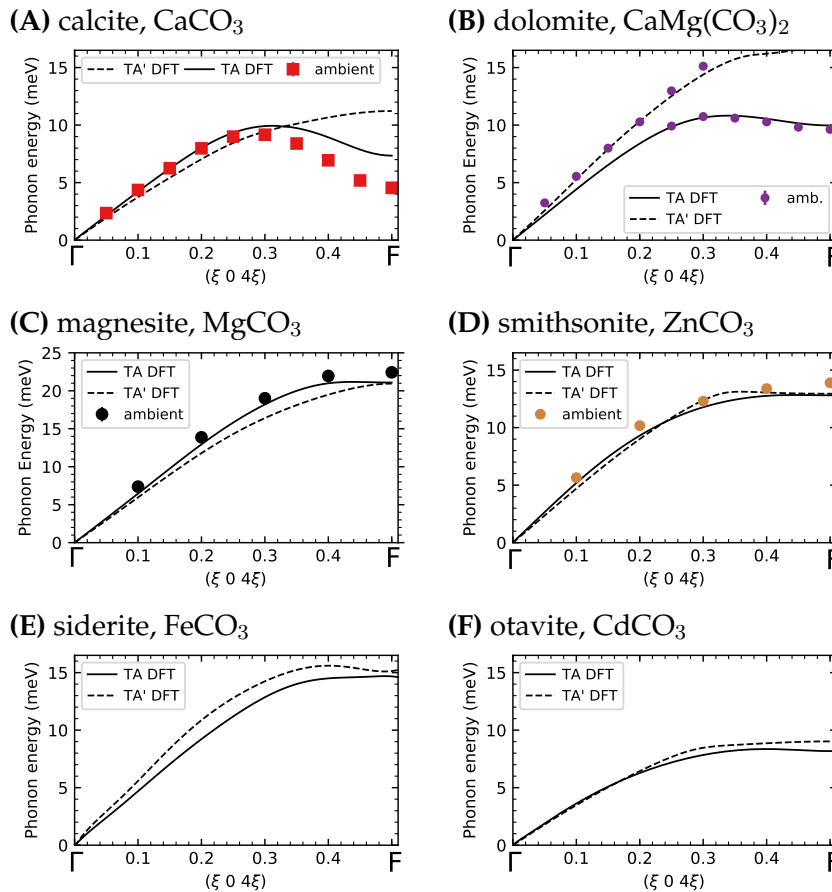


Figure 4.7: (A-F) Measured (various symbols, described in insets' legends) and calculated (solid and dashed lines) dispersion curves of rhombohedral carbonates. Note the different energy scale taken for magnesite (C).

The dispersions calculated for dolomite, magnesite and smithsonite match the experiment very well, however for calcite there is a discrepancy between calculated and measured energy in the vicinity of the zone boundary, $\xi > 0.3$, as shown in Figure 4.7A. This might point to the anharmonic character of the phonon, as our calculations were performed within the harmonic approximation. For

each carbonate the calculated dispersion of the TA Γ - F branch is sinusoidal up to $\xi \in [0.25, 0.35]$, depending on the cation, and afterwards decreases anomalously in calcite and dolomite, or flattens in other carbonates.

4.4 Phonon-driven transitions to calcite-II and dolomite-II

We have performed high-pressure IXS experiments to investigate how the dispersion anomaly in calcite and dolomite changes with pressure, and determine if the F -point phonon drives the transitions to calcite-II and dolomite-II as suggested in previous theoretical works [88, 89]. The dispersion relations measured at various pressures are shown in Figure 4.8, and the IXS spectra for the measurements at the F -point are shown in Figure 4.9. The strong elastic line present in high-pressure measurements, Figure 4.9, originates from the elastic scattering on the methanol-ethanol pressure medium.

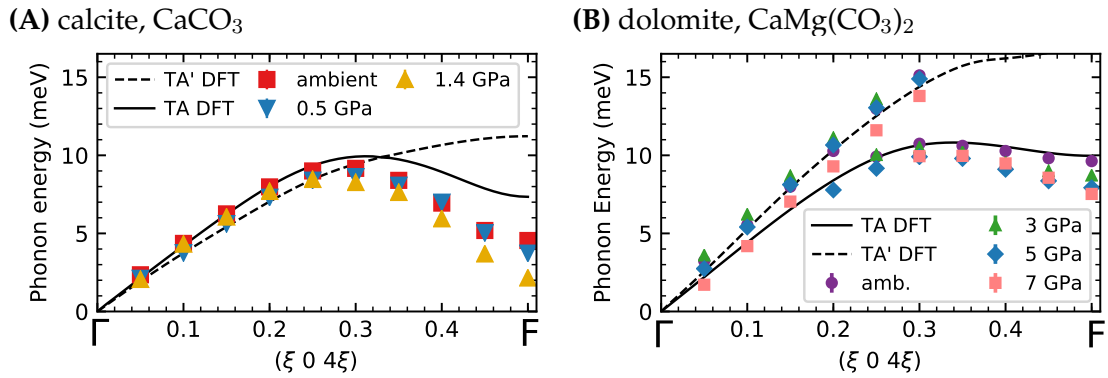


Figure 4.8: Dispersion of the TA Γ - F branch in calcite (A) and dolomite (B).

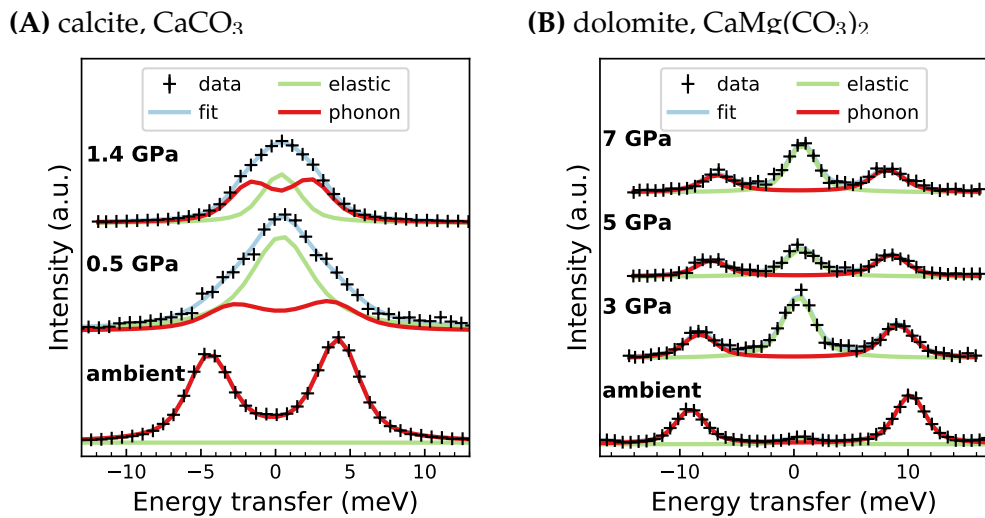


Figure 4.9: High-pressure IXS spectra (+) of calcite (A) and dolomite (B) at various pressures. The fit (blue) consists of the elastic line (green) and phonon excitations (red).

In case of calcite we observed a strong softening of the TA F -point phonon with pressure, as shown in Figure 4.10, that freezes at 1.8 GPa, which is the pressure of transition to the calcite-II phase. In dolomite, where our experiment was limited to 7 GPa, we observe systematic softening of the same phonon. Our experimental results can be modeled with the theoretical predictions [103, 104], which show that in the mean-field picture the energy of the soft phonon, E , changes with pressure, p as

$$E(p) = E_0 \sqrt{1 - p/p_c}, \quad (4.1)$$

where E_0 is the energy of the phonon at ambient pressure, and p_c is the pressure of the transition. This model fits perfectly with the energies measured for calcite, and gives the transition pressure $p_c^{\text{Ca}} = 1.8$ GPa. It also fits the data of dolomite, and allows extrapolating our results, indicating a transition pressure $p_c^{\text{Do}} = 17.5$ GPa, which is consistent with the pressure measured by Merlini et al. [96] $p_c = 17$ GPa, and calculated by Zucchini et al. [89] $p_c = 17$ GPa.

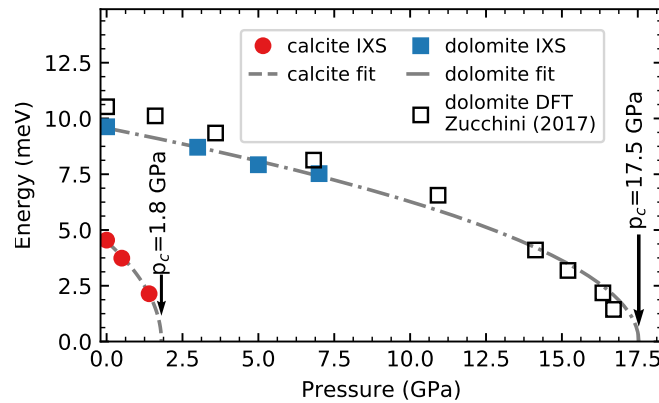


Figure 4.10: Pressure dependence of the energy of the TA F -point phonon in calcite (filled circles) and dolomite (filled squares), together with fit to the IXS data (dashed lines) and values calculated by [89] (empty squares).

The soft phonon theory dictates that the displacement pattern, eigenvector, of the softening phonon must match the displacement of the atoms upon the transition. If it doesn't, the phonon is not *driving* the transition, and its softening could be either accidental, or due to coupling to the real mechanism driving the transition. As the experimental determination of the eigenvector is practically impossible, we determine it from the DFT calculations. We consider them highly reliable, as they excellently reproduce the measured TDS maps and IXS intensities.

The calcite \rightarrow calcite-II transition is characterized by the rotations of the CO_3 groups around the hexagonal c axis, and the displacement of the Ca atoms within the (104) plane. The displacement of the atoms due to the transition is shown in Figure 4.11, together with the eigenvector of the soft phonon determined from

our calculations. There is an excellent agreement between the calculated and observed displacement. A detailed analysis shows that the rotation of the CO_3 groups shows an umbrella-like distortion, where the displacement of the oxygen atoms has a component along the c axis, that is larger than that of the central carbon atom. This resembles the undulated movement observed by Ishizawa et al. [105] at high temperatures, when calcite approaches the transition to calcite-IV, and will be the topic of the study presented in Chapter 5. The agreement between the calculated and observed atomic displacement, together with freezing of the TA F -point phonon observed experimentally, clearly shows, that the transition to calcite-II is driven by the soft phonon.

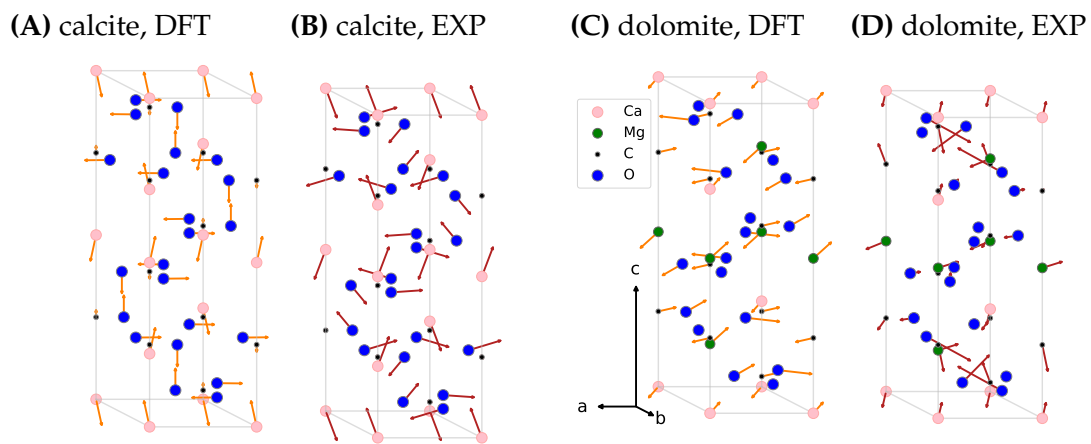


Figure 4.11: The eigenvector of the soft F -point phonon in calcite (A) and dolomite (C) together with the atomic displacement due to the corresponding structural transitions, calcite $\xrightarrow{1.7 \text{ GPa}}$ calcite-II (B) and dolomite $\xrightarrow{17 \text{ GPa}}$ dolomite-II (D). Displacements of the atoms are indicated with arrows. Atom coloring is described in the legend, the hexagonal reference system is shown with black arrows.

The transition from dolomite to dolomite-II is similar to calcite-II, with few differences. The magnesium atoms are displaced in a different way than calcium, and there seems to be a difference in the magnitude of the rotation in CO_3 groups. The determination of the displacement across the transition can lack in accuracy, as it is based on the comparison of the dolomite structure at 14 GPa (from Merlini et al. [96]), and the dolomite-II structure at 20.5 GPa (from Binck et al. [106]). Structures closer to the transition pressure are not reported in the literature. The displacement of atoms in dolomite and the eigenvector of the soft F -point phonon are shown in Figure 4.11. The agreement between the experiment and calculations is good, however not as good as in calcite. Nevertheless, our calculations reproduce the main features of the atomic displacement, the rotations of the CO_3 groups and the displacement of the cations, with correct phase factors. This, together with the experimental evidence of softening of the F -point phonon, allows us to conclude that the transition to dolomite-II is also driven by the soft phonon.

4.5 F -point phonons in other carbonates

As the transitions to calcite-II and dolomite-II were shown to be phonon-driven we were motivated to investigate the F -point phonon in other carbonates, and by comparison of the results, attempt to determine the mechanism of the F -point phonon instability.

Magnesite

We start with another geologically relevant carbonate, magnesite, that after heating to 2000 K at 115 GPa transforms to magnesite-II. As described in details beforehand, see section 4.1, despite the same label the structure of magnesite-II is believed to be drastically different compared to the structure of calcite-II.

The phonon dispersion of the TA Γ - F branch in magnesite is shown in Figure 4.7. The energy of the phonon at the F point is exceptionally high, 22.4 meV, compared to other carbonates, where $E_F < 15$ meV. In order to determine how the lattice dynamics of magnesite changes under pressure we performed the calculations at ambient pressure and 100 GPa. The calculated dispersion relations of low-energy branches and the eigenvector of the TA F -point phonon are shown in Figure 4.12. Our calculations show a very small softening of the TA F -point phonon, from 21.1 meV at ambient pressure to 18.4 meV at 100 GPa. On the other hand the energies of the T -point phonons increase with pressure. Extrapolation of the phonon softening with formula 4.1 gives a transition pressure $p_c = 420$ GPa. Another interesting result is that even though the pressure drastically modified the dispersion relations, the eigenvector of the softening phonon does not change as much. At high pressure the displacement of magnesium atoms turns towards the c axis, but the rotation of the CO_3 groups is preserved.

The displacement pattern of the F -point phonon in magnesite is very similar to the one in calcite and dolomite, compare Figures 4.11 and 4.12. By displacing the structure of magnesite at 100 GPa by the eigenvector of the softening phonon and relaxing the structure, we have obtained a new, monoclinic phase of magnesite, magnesite-F. It consists of co-planar, triangular CO_3 groups and magnesium coordinated by eight oxygen atoms. It is topologically identical to calcite-II and dolomite-II, and different from any of the high-pressure magnesite structures reported up to now, summarized in [92]. At 100 GPa the energy of the magnesite-F phase is 88 kJ/mol higher than the energy of magnesite, so it could be a metastable phase of magnesite at 100 GPa, that becomes stable above $p_c = 420$ GPa. That is under the assumption that there are no other competing structural instabilities, that would distort magnesite in another fashion. As the phase diagram of magnesite is unexplored above 100 GPa, and it doesn't seem

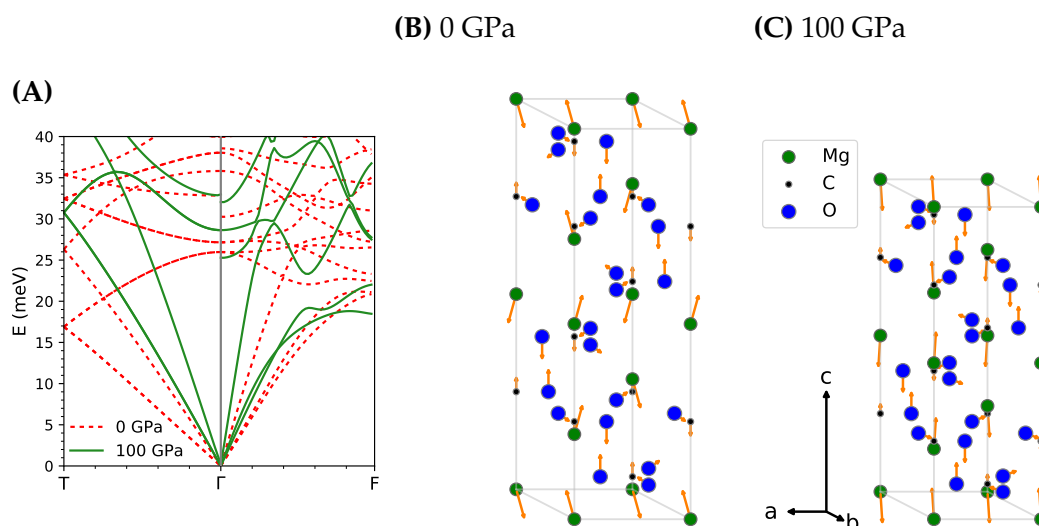


Figure 4.12: (A) Calculated phonon dispersion relations for magnesite at ambient pressure and 100 GPa. (B) Eigenvector of the softening F -point phonon at ambient pressure and (C) 100 GPa.

to compare well with phase diagrams of calcite and dolomite, the stability of the magnesite- F phase is an open question.

The discussion above was stripped of the temperature effect, which is a crucial parameter in the geological context. A pressure of 100 GPa corresponds to lower mantle conditions, where the expected temperature is 2500 K [84]. As discussed in the beginning of this section, at these conditions magnesite undergoes a transition to the tetrahedral carbonate phase. This transition is reconstructive, which means it involves a complete reorganization of atoms and their bonds, and in result it can't be associated with a soft phonon, as the transition does not involve a continuous, collective displacement of the atoms. Therefore, it is doubtful that magnesite- F is stable at high temperatures.

Otavite

Otavite is a carbonate that seems likely to undergo a transition to the calcite-II structure. The energy of the TA F -point phonon is 8.2 meV, which is slightly lower than in dolomite, 9.6 meV, thus it is expected that the transition would occur at similar pressures as in dolomite. Minch et al. [107] observed strong peak broadening at 19 GPa in both their powder diffraction and Raman scattering measurements. They did not observe the appearance or vanishing of peaks in their diffractograms and Raman spectra, which is indicative for a reconstructive transition to the aragonite structure, which they were expecting. They concluded that at 19 GPa otavite undergoes a transition associated with a symmetry change to an unknown structure.

Based on their reports it seems possible that they observed the transition to the calcite-II phase. It is continuous, so it would involve splitting of the peaks, observed as broadening in lower resolution experiments. In addition, the new peaks appearing because of the symmetry change would be initially low in intensity, due to the continuous character of the transition.

Siderite

The stability of siderite has been thoroughly studied at high pressure and temperature by Cerantola et al. [108], who established an updated phase diagram up to 120 GPa. By the extrapolation of their results they suggest that at ambient temperature siderite remains in the calcite structure at least up to 120 GPa.

We have calculated the phonon energies at ambient pressure, as well as at 45 GPa in the high-spin and low-spin state of iron, the dispersion relations of selected branches are shown in Figure 4.13. We observed that the dispersion anomaly is enhanced with pressure, and at 45 GPa the branch has a visible local minimum at the F point, see blue line in Figure 4.13. The F -point phonons soften with pressure, unlike the T -point phonons, which resembles the case of magnesite, see Figure 4.12. By comparing the energy of the F -point phonon at ambient pressure, 14.7 meV, and at 45 GPa in the HS state, 13.3 meV, we extrapolate that the phonon would soften to zero energy at 248 GPa. On the other hand the spin transition increases the energy of all phonons, as shown with green lines in Figure 4.13, for more directions see Figure 3.4. The energies of the F -point phonons increase well above the values at ambient pressure and effectively, the transition to calcite-II structure is shifted to even higher pressures. We have not performed full lattice dynamics calculations for siderite at higher pressures, thus we are not able to extrapolate the critical pressure for transition to the calcite-II phase. By comparison to magnesite it seems that the transition pressure in siderite would be well beyond 400 GPa, where, most probably, other instabilities in the crystal structure would start competing with the soft phonon of the F -point.

Smithsonite

There is only one experimental study reporting on the high pressure behavior of smithsonite. Gao et al. [109] reported that up to 50 GPa smithsonite is stable in the calcite structure. Bouibes and Zaoui [110] performed DFT-based calculations and showed a variety of possible high pressure structures of smithsonite. None of them resembles the calcite-II structure. Our measurements show, that the energy of the F -point phonon is 13.9 GPa, which is higher than for dolomite, but lower than for the magnesite. Due to the lack of data it is not possible to predict if smithsonite could adopt the calcite-II structure, and if so, at what pressure.

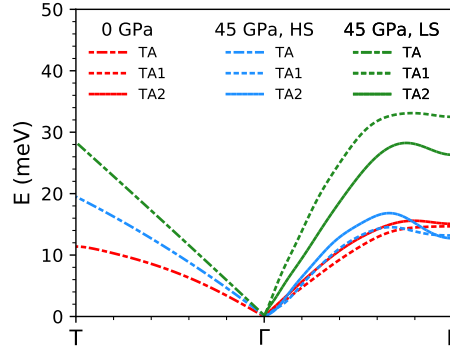


Figure 4.13: Calculated dispersion relations of the TA phonons for siderite at ambient pressure (red lines) and 45 GPa in the high-spin (blue lines) and low-spin (green lines) state of iron.

4.6 Crystal chemistry of the transition to the calcite-II structure

The selected properties of the carbonates studied in this chapter are summarized in Table 4.2. The attempt was to determine which property correlates best with the transition to the calcite-II structure, which is presented in Figure 4.14. The first choice was the energy of the soft-phonon at the F point, E_F , at ambient pressure. Next, we follow the idea, that the transition pressure will be proportional to the forces arising due to the displacement of the F -point phonon. The energy of the phonon is not the direct indicator here, as it depends on the mass of the cation. We employ a mass on the spring model, an archetype to the harmonic oscillator model which describes the phonons, where the restoring forces are quantified in the spring constant, k . Based on the solution to the harmonic oscillator problem, $k_{\text{eff}} = m_{\text{eff}}\omega^2$, which will be further called the effective force constant. We employ energy instead of angular frequency, as $E_F = \omega/\hbar$, and the effective mass is $m_{\text{eff}} = \sum_i m_i U_i$, where index i runs over the atoms in the unit cell, m_i is the mass, and U_i is the displacement of an atom. In the end we consider the ionic radius of the cation, r_{ion} .

As the *cation*–O bond is ionic in carbonates, the physical properties based on the bonding scheme should not depend on the valence electrons of the cation, but rather on its radius. In case of the transition pressure there exists a pressure homologue rule [111, chap. 2.5], which states that the transition pressure scales linearly with the ionic radius. The aragonite→post-aragonite transition is a perfect example of that, as shown in Biedermann et al. [112]. In short, the ion with larger ionic radius has its valence electrons closer to the elements which participate in bonding, thus imitating higher pressure conditions, where the atoms would be

Table 4.2: Selected properties of carbonates and their cations, that could correlate with the transition to the calcite-II structure. Entries sorted by the energy of the TA phonon at the F point, E_F .

	cation	E_F (meV)	k_{eff} ($10^3 \cdot \text{u} \cdot \text{meV}^2$)	r_{ion} (\AA)	p_c (GPa)
calcite	Ca	4.2	1.2	1.0	1.8
otavite	Cd	8.2	10.9	0.95	19.0 ?
dolomite	$\text{Ca}_{0.5}\text{Mg}_{0.5}$	9.6	5.0	0.86*	17.5
smithsonite	Zn	13.9	15.9	0.74	?
siderite	Fe	14.7	17.6	0.78 ^{HS} 0.61 ^{LS}	? (280)
magnesite	Mg	22.4	24.0	0.72	? (420)

? not clear if the transition takes place, see the main text for details

* taken as an average between Mg and Ca

HS, LS high-spin, low-spin electronic configuration

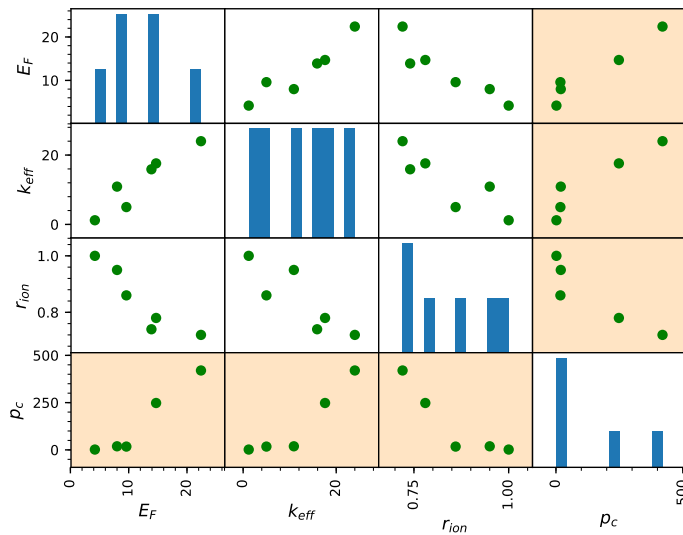


Figure 4.14: Correlation maps for parameters presented in Table 4.2. Histograms of the values on the diagonal, p_c plots are highlighted with orange color.

brought closer together. In effect the transition pressure is lower for cations with larger ionic radius.

In case of the transition to the calcite-II structure the transition pressure does not scale linearly with the ionic radius. Neither does the effective force constant. Shi et al. [113] investigated solid solutions of calcium-manganese carbonates with up to 40% of Mn, and have observed a linear increase in transition pressure to calcite-II with increased manganese content. They reported the scaling factor of 0.19 GPa/mol, e.g. for CaCO_3 $p_c = 1.5$ GPa, and for $\text{Ca}_{0.6}\text{Mn}_{0.4}\text{CO}_3$ $p_c = 9.1$ GPa. These results, however, do not seem to transfer to a comparison of different cations.

It is likely that the underlying mechanism of the transition can not be simplified to a single parameter.

4.7 Conclusions

We have presented a comprehensive analysis and comparison of the high pressure transitions from calcite to calcite-II and from dolomite to dolomite-II. We have combined the TDS and IXS measurements with the DFT based calculations in order to determine full lattice dynamics of calcite, dolomite, and magnesite. In addition we have investigated smithsonite, siderite, and otavite in less comprehensive manner. We were able to show that the transition to calcite-II and dolomite-II is based on the same mechanism, i.e. it is driven by the soft, transverse acoustic phonon with the F -point wave vector. We have compared the character of the F -point phonon in various carbonates in order to determine the underlying physical mechanism of the anomalous dispersion of the Γ - F branch.

The phonon dispersion relations, from which full lattice dynamics for calcite, dolomite, and magnesite can be retrieved, are given in Appendix A

5

Phonon coupling to the high-temperature rotational disorder in calcite

Apart from the variety of phase transitions at ambient temperature and high pressure, calcite undergoes very interesting phase transitions at lower pressures and high temperatures, namely to calcite-IV and calcite-V [86]. These phase transitions are associated with the rotational disorder of the CO_3 groups [105, 114], and even though up to few years back there was no direct experimental confirmation of this hypothesis, it was widely agreed upon.

The experimental difficulties of measuring calcite at high temperatures and ambient pressure arise from the fact that at 870 K calcite decomposes to CaO and highly reactive CO_2 , while the transition temperatures to calcite-IV and calcite-V are $T_{\text{IV}} = 985$ K and $T_{\text{V}} = 1240$ K, respectively [105]. Investigation of the high temperature calcite-IV,V phases requires prevention of the decomposition and complicates the experiment. Recently Ishizawa et al. [105] provided an excellent experimental evidence for the rotational disorder phenomenon by a single crystal x-ray diffraction study. Although their models very accurately describe the reorientation of CO_3 groups, we were motivated to provide a more direct experimental evidence of the dynamical character of the high temperature transitions. Single crystal diffraction provides a time-averaged image of the structure, while inelastic x-ray scattering combined with DFT based calculations provides exact displacement pattern of the atoms, the frequency of the vibration, and gives clues on the harmonicity of the phonon.

This chapter presents the methods and instruments developed in order to perform high temperature IXS experiments on calcite, shows the experimental results and with support of the DFT calculations provides a full explanation of the calcite to calcite-IV transition from the lattice dynamics point of view. It is shown that once again the F -point instability plays a crucial role in the transition mechanism, just as in the high pressure study presented in the previous chapter.

5.1 Introduction

The crystal structure of calcite at ambient conditions was determined in 1914 by Bragg [115] and is shown in figure 5.1a. However, it was known already two years before that it undergoes a reversible phase transition at 1240 K [116]. Much later Mirwald [117] reported on another high temperature transition in calcite that occurs at around 985 K. They named the high temperature phases calcite-IV and calcite-V and speculated on the rotational disorder character of these phases.

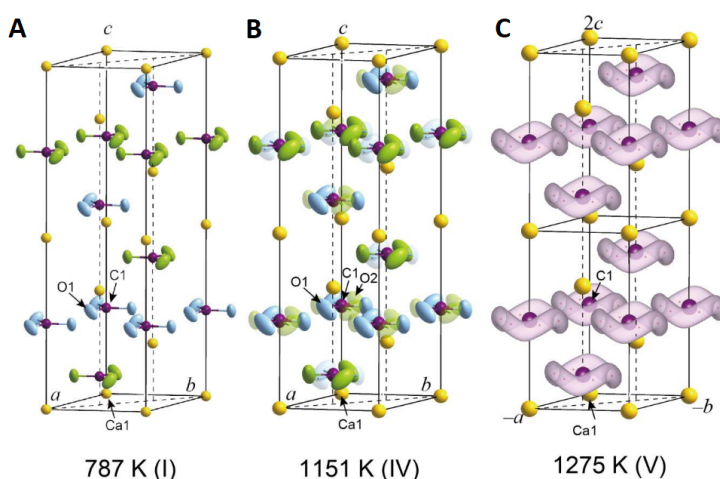


Figure 5.1: Crystal structure of calcite (A), calcite-IV (B), and calcite-V. Calcium and carbon atoms are depicted with yellow and purple spheres respectively, while oxygen atoms with green and blue ellipsoids (A,B) indicating the average displacement, or with pink orbitals, showing the path on which the oxygen atoms rotate. Figure adapted from Ishizawa et al. [105].

First experimental evidences on the rotational disorder was provided by Dove and Powell [114] who performed a neutron powder diffraction study. Recently Ishizawa et al. [105] published an excellent dataset from single-crystal diffraction study, that elegantly presents the character of the reorientation in calcite. They showed that the calcite-IV phase arises due to partial disorder of the CO₃ groups that are rotated by 60° to the alternate configuration, as shown in Figure 5.1B. This behavior arises from the thermal fluctuations in energy that allows a number of CO₃ groups to overcome the potential barrier between normal and alternated orientation. As the temperature increases, the potential barrier decreases and the thermal energy of atoms increases, see Figure 5.2. Above $T_V = 1240$ K the thermal energy is higher than the potential barrier and CO₃ groups freely rotate on the undulated orbitals, as shown in Figure 5.1. Ishizawa et al. [105] were able to determine the percentage of CO₃ groups being in alternate orientation, as shown in Figure 5.2A, they have also determined the energy of the potential barrier at different temperatures, shown in Figure 5.2B.

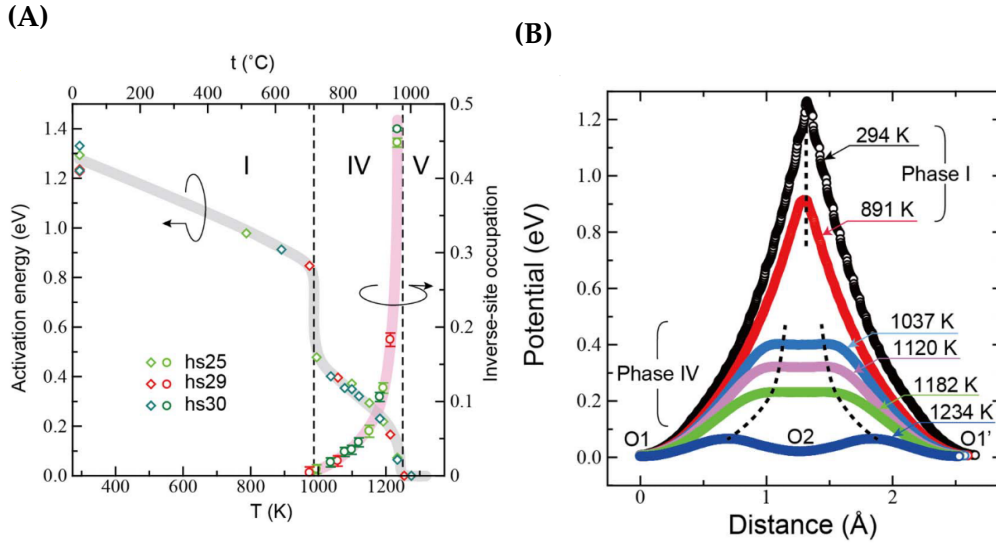


Figure 5.2: (A) The potential barrier for adapting the alternate orientation for CO_3 groups in calcite and the inverse-site (alternate orientation site) occupation. (B) The potential along the O1-O2-O1' arc, following the Figure 5.1. Figures adapted from Ishizawa et al. [105].

The motivation of the current study was to provide more direct experimental confirmation of the rotational disorder of CO_3 groups at high temperatures. Since the disorder is dynamical it has to manifest in a specific way in experiments investigating lattice dynamics. Previous reports of such experiments include infrared emissivity [118], Raman scattering [119] and inelastic neutron scattering [97, 98] measurements. We found of particular interest the latter ones, that show an anomaly in the Γ -F branch, its dependence on temperature and possible explanations of the observed phenomena. The interesting features observed in these reports provided a motivation for performing the IXS experiment at high temperature, as to confront the observed phenomena with a complementary technique and revise the physical explanations. These results will be presented and discussed in details further on.

In summary, the TDS measurements were performed in order to get the overview of the diffuse features at high temperatures. However, due to decomposition of calcite below the transition, we were not able to obtain DS maps of calcite-IV and calcite-V. After identification of interesting q -points from DS maps we planned the IXS experiment at high temperatures. In order to measure IXS spectra of calcite-IV and calcite-V phases a custom sample environment equipment was built. We have also performed full lattice dynamics calculations to determine the displacement patterns of measured phonons and identify their role in the transition.

5.2 Diamond chamber sample environment

In order to perform the IXS experiment of calcite-IV and calcite-V one needs to prevent the decomposition of calcite to CaO and CO₂ above 875 K. This can be accomplished by applying a sufficient pressure of CO₂ on the sample. In this experiment the sample was contained in a millimeter sized single crystal diamond that consists of two parts, as shown schematically in Figure 5.3, photos are shown in Figure 5.4. The first advantage of using diamond is that it's chemically inert to the highly reactive CO₂ at high temperatures. Secondly, the phonons of diamond have relatively high energies away from the center of the Brillouin zone, so they will not obscure the signal from lower energy calcite phonons. Lastly, diamond is the hardest known material and it is able to withstand the internal pressure of CO₂ and external uniaxial stress applied in order to maintain the sample chamber closed.

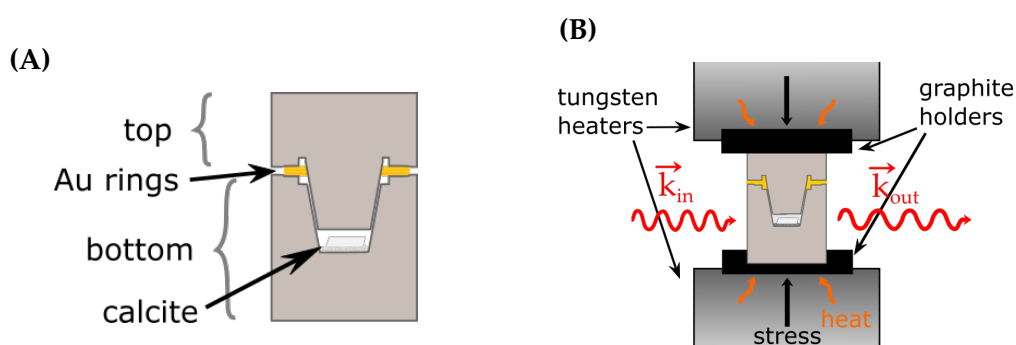


Figure 5.3: Side view cut of the diamond sample chamber (A) just after loading and (B) during heating. Single crystal of calcite is glued by the mixture of epoxy and MgCO₃ powder to the hole in the bottom diamond. The golden rings are acting as a gasket and spacer between the top and bottom diamonds. The chamber is placed on the graphite holders which transfer the stress and heat from the tungsten heating stage to the diamond.

After loading the sample in the diamond chamber the custom cut gold rings are placed on the bottom diamond which act like a gasket and the spacer between the top and bottom diamond. Next, the diamond chamber is placed on the graphite holders that ensure proper thermal contact between the diamond and the heating system.

A diamond chamber is placed in the sample environment as shown in Figure 5.5. It consists of the resistive heating stage that accommodates the diamond chamber and the uniaxial pressure system that closes the chamber. Both of them are enclosed in a sealed housing with high vacuum.

The resistive heating stage is made of two tungsten heaters, top and bottom ones, that are water cooled in order to confine the heated volume just to the diamond chamber. The temperature is monitored by a K-type thermocouple, with

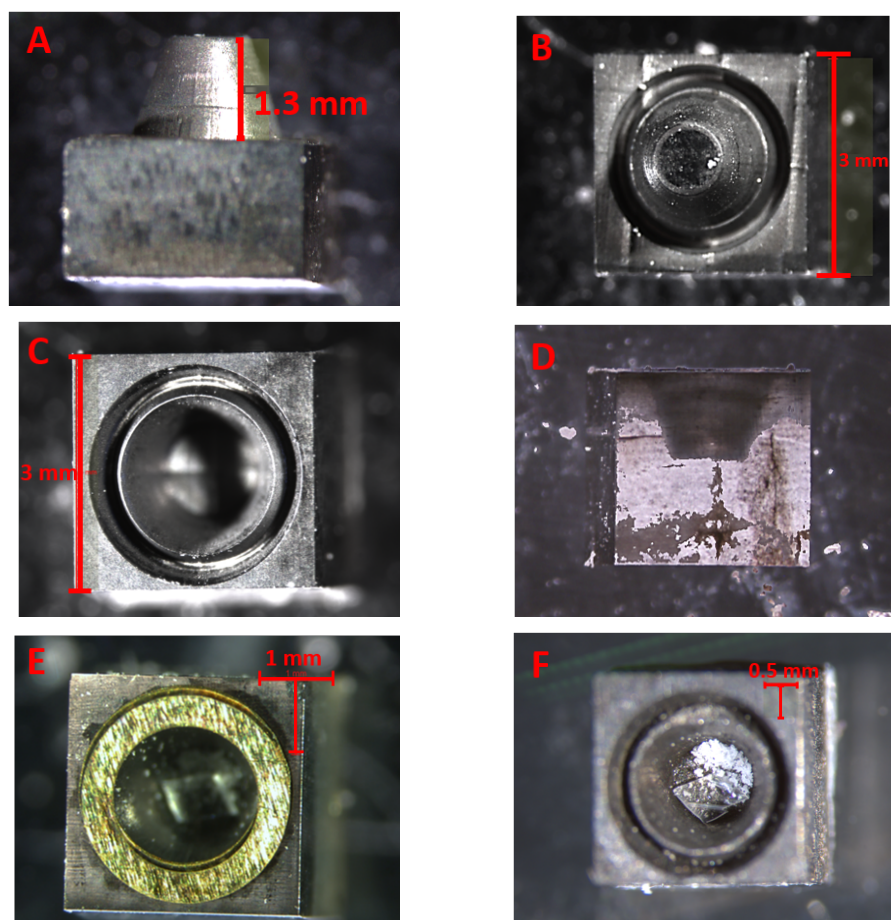


Figure 5.4: Photos of the diamond chamber. Top (A) and the side (B) view of the top diamond. Top (C) and a side (D) view of the bottom diamond. (E) Gold rings placed on the bottom diamond. (F) Test loading, with MgCO_3 (white powder) and calcite crystal. Photo (D) shows the diamond after the high pressure experiment, where the outer graphite layer felt off, showing the drilled chamber.

the sensing element glued in the proximity of the diamond chamber. Together with the power generator the thermocouple is connected to a PID controller that allows manipulating the temperature by adjusting the current parameters remotely. The system was commissioned up to 1320 K, where the applied voltage was 3 V and the current 32 A, DC.

In order to apply the uniaxial pressure, four screws are adjusted on the bottom part of the chamber. They transfer the force through a long pin to the spring that is attached to the bottom part of the heating stage. The pressure is monitored by a piezo-tensometer which is located between the screws and the pin.

In order to prevent the decomposition of diamond under high temperature and oxygen atmosphere, the chamber is sealed under high vacuum of around 10^{-5} mbar. Finally the chamber is mounted on the ID28 sample stage and the IXS experiment can be performed.

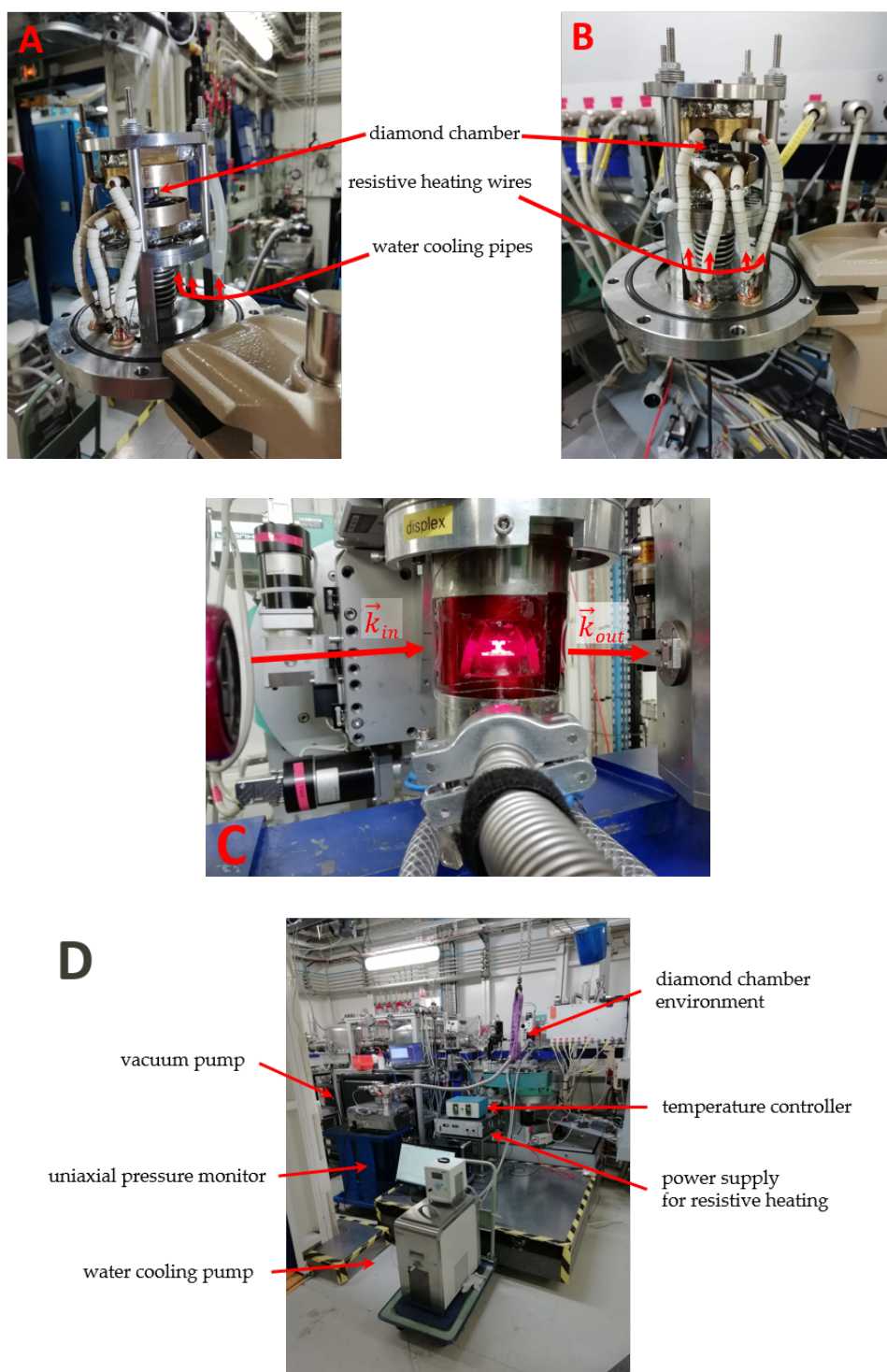


Figure 5.5: Diamond chamber sample environment for the high temperature IXS experiment with calcite, mounted at ID28 of the ESRF. (A) and (B) show the sample environment with the diamond chamber mounted at the heating stage. (C) Fully assembled sample environment with the diamond chamber heated to ~ 1000 K. The arrows are indicating the incoming and scattered x-rays. (D) Apparatus used to control and monitor the conditions of the sample environment.

5.3 Sample preparation

The IXS experiment with the diamond chamber was performed with a single crystal plate of calcite with dimensions $600 \times 600 \times 200 \mu\text{m}^3$ polished with the $(\bar{1}20)$ face corresponding to the large $600 \times 600 \mu\text{m}^2$ surface. It was etched in diluted nitric acid in order to clean and smoothen its surface. The crystal was glued to the bottom of the sample chamber with a mixture of epoxy and MgCO_3 powder. At 670 K MgCO_3 decomposes to MgO that binds the glue and CO_2 . During the heating the CO_2 gas expands and exerts the pressure that prevents the decomposition of calcite.

Due to the presence of four stabilizing pins that hold the heating stages together, the sample needs to be carefully oriented in a way, that the chosen part of the reciprocal space is accessible in the restricted geometry. The choice of points measured by IXS was based on the previous TDS experiment, which allowed to identify the interesting regions of the reciprocal space. The sample was oriented with the (104) crystal face along the incident beam direction and the $(\bar{1}20)$ face in vertical direction. Such an orientation gives access to the quadrant of the H0L plane with $H < 0$ and $L > 0$.

5.4 Experimental details

An initial TDS measurement was performed with the same calcite crystal as described in the previous chapter, section 4.2. The crystal was heated by the hot air heat blower, so that the decomposition of calcite was not prevented. The measurement was performed at the side station of the ID28 beamline [37] with a wavelength of 0.6968 \AA . The five circle goniometer was set to $\chi = -30^\circ$ with the detector position $\Gamma = -19^\circ$ and the sample to detector distance of 244 mm. Full ϕ scans were performed with the angular increment of 0.25° , one second integration time, and without using an attenuator.

The IXS experiment was performed at the ID28 beamline of the ESRF [32, 33]. The incoming beam was monochromatized to an energy of 17.794 keV with the backscattering monochromator consisting of a perfect silicon crystal with (999) diffracting reflection. The beam was focused with the KB mirrors to a spot with dimensions of $30 \times 10 \mu\text{m}^2$ on the sample. The determination of the instrumental resolution was based on a prior measurement of a polycrystalline plexiglass sample cooled to low temperatures.

5.5 Mapping the reciprocal space by thermal diffuse scattering

Figure 5.6 shows the intensities reconstructed on the (HK0) and (H0L) planes in the reciprocal space, where the intense spots at the F points of the Brillouin zone were observed. It is clearly visible that with increasing temperature the cloud of TDS signal around Bragg reflections and around the F -points increases in intensity and volume in reciprocal space. The reconstructions at 875 K are contaminated with the signal from the CaO that is forming due to the thermal decomposition of calcite. The TDS features at 1075 K are much less intense than at 875 K due to the fact that a large part of the crystal has decomposed, which is also indicated by an increase in intensity of the CaO powder rings.

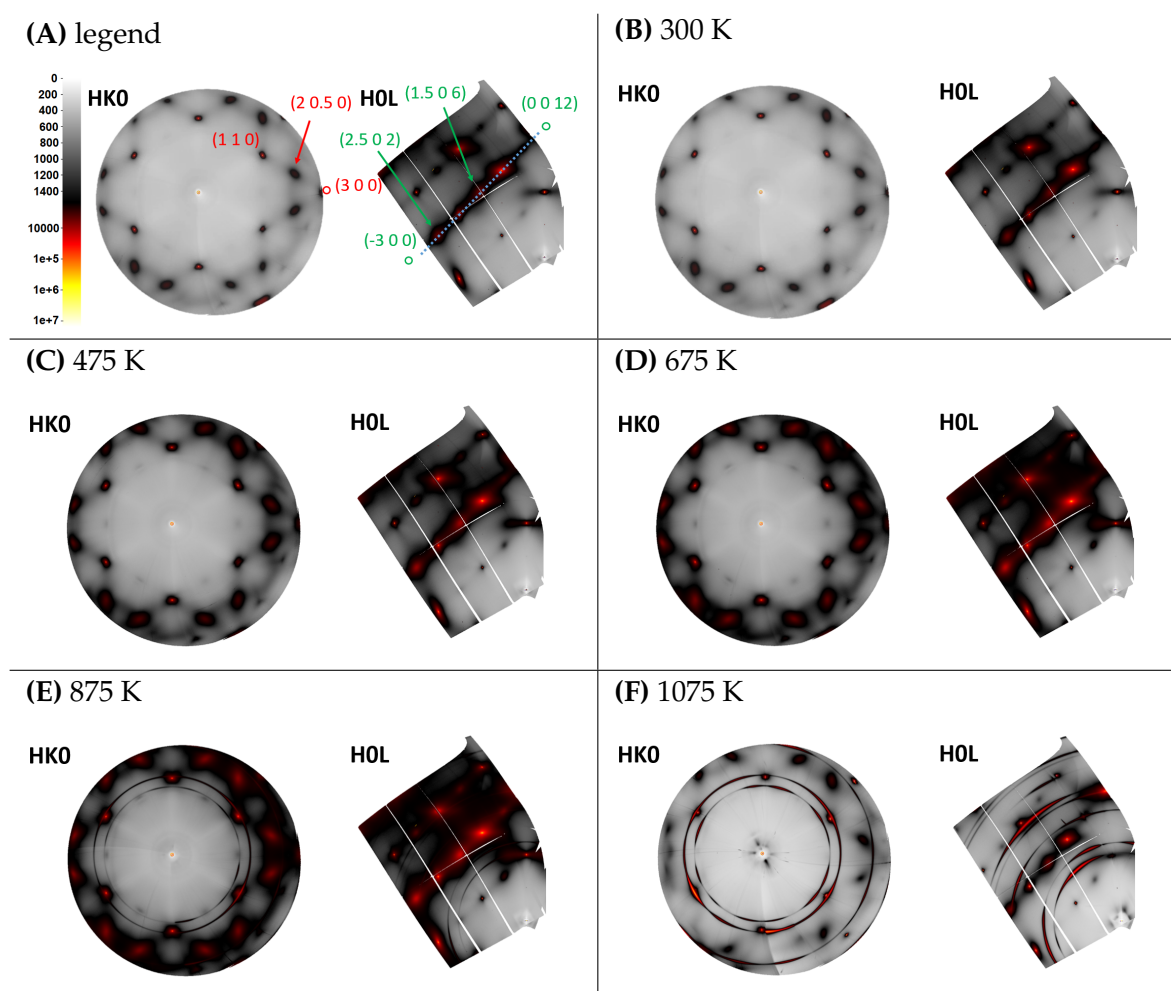


Figure 5.6: (A) Legend of the intensity maps shown in consecutive insets. Empty circles point on the unrecorded Bragg reflections, arrows at various F points. Red annotations refer to the (HK0) map, green ones to the (H0L) map. The dashed blue line shows the path on which intensities were reconstructed and shown in Figure 5.8. (B-F) Intensity maps measured at various temperatures reconstructed on high symmetry planes in the reciprocal space.

The intensity maps of calcite at high temperatures were also reconstructed from single crystal diffraction data by Ishizawa et al. [105] for the HK0 and HK1 plane. Figure 5.7 shows their results. As in the experiment reported here, the decomposition of calcite was not fully suppressed, and the rise of rings coming from CaO powder was observed. The maps reconstructed from the data collected at ID28 are superior to the ones reconstructed by Ishizawa et al. [105] owing to the use of a detector with higher dynamic range and finer slicing of the reciprocal space. The intense TDS signal at the F point was already observed in the (HK0) plane, here it is shown, that the signal at the F points in the (H0L) plane is even more intense.

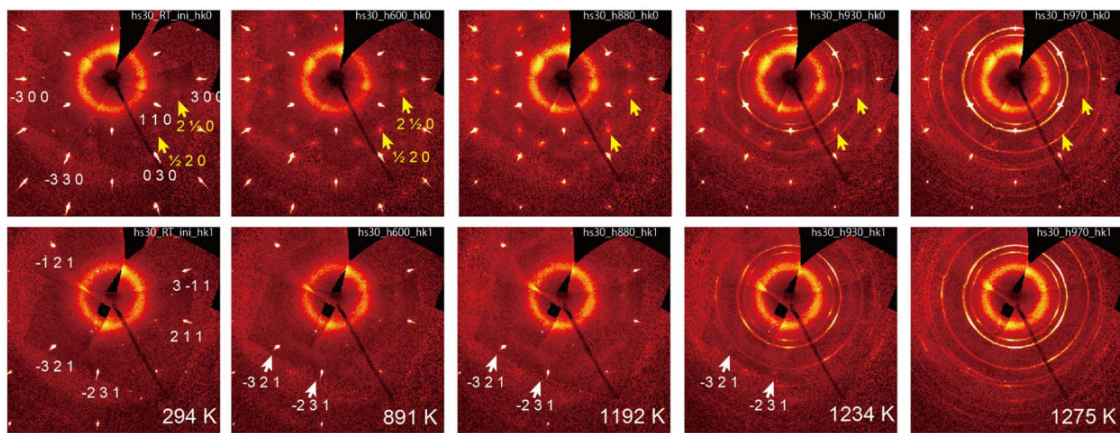


Figure 5.7: Intensity maps measured at various temperatures by Ishizawa et al. [105]. Top row shows the (HK0) plane, bottom row the (HK1) plane. Yellow arrows show the diffuse scattering signal observed at the F points, white arrows point at the Bragg reflections.

In order to quantitatively analyze the TDS signal, the reconstructed intensities were further mapped on the line between the $(-3\ 0\ 0)$ and $(0\ 0\ 12)$ reflections, where an intense signal is observed at the F points, see Figure 5.6. The results are shown in Figure 5.8. The intensities reconstructed from measurements at different temperatures were rescaled, so that the maximum intensity value of the $(1\ 0\ 8)$ reflection is the same. The glitches in the intensity profiles are due to the voids in the reconstructed maps, see figure 5.6, that are present because of the gaps between the detector panels.

Clearly there is a local maximum of the intensity at the three recorded F points. The maxima are assumed to arise due to the TDS signal. Two strongest spots were observed at the $(1.5\ 0\ 6)$ and $(2.5\ 0\ 2)$ points. Note that the intensities in figure 5.8 were not shifted vertically. The intensity of the signal increases with temperature, which is characteristic of the TDS signal due to the temperature factor in equation 2.19.

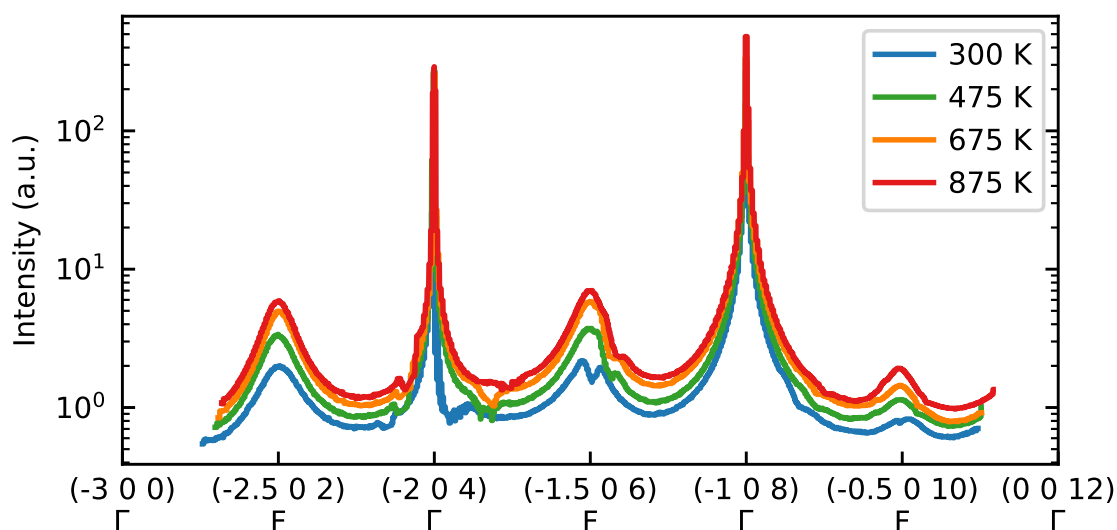


Figure 5.8: Intensity along the line between the $(-3\ 0\ 0)$ and $(0\ 0\ 12)$ reflections, measured at various temperatures. Glitches in the intensity profiles are due to the gaps between the detector panels. The intensities were normalized to the maximum intensity value of the $(1\ 0\ 8)$ reflection. Note that the intensities reconstructed for different temperatures were not shifted vertically, the difference arises from the high TDS signal.

Because the decomposition of calcite was not prevented for the TDS experiment, the intensity maps of calcite-IV, as shown in Figure 5.6F for 1075 K, are difficult to compare with that of calcite. Additionally, the maps of calcite-V were not recorded, as the sample decomposed. Nevertheless, the intense spots at the F points in the calcite-IV phase are still visible and since their intensities are at least an order of magnitude lower than the Bragg reflections, it can be speculated that the phonon energy at the F point is just few meV.

5.6 Anharmonicity of the Γ - F branch from inelastic x-ray scattering

With the calcite sample loaded in the diamond chamber, as shown in Figure 5.4, and placed in the sample environment, as shown in Figure 5.5, the IXS experiment was performed at temperatures above 875 K. Results from lower temperatures come from previous measurements with the heat blower. The experiment was focused on measuring the energy of the soft phonon at the F point, however up to 875 K, below the decomposition temperature, the dispersion of the whole branch was measured.

We have observed a softening and broadening of the F -point phonon with increasing temperature, as shown in Figure 5.9. A detailed analysis of the phonon line-shape showed, that even though the typical Lorentz profile fits the spectra very

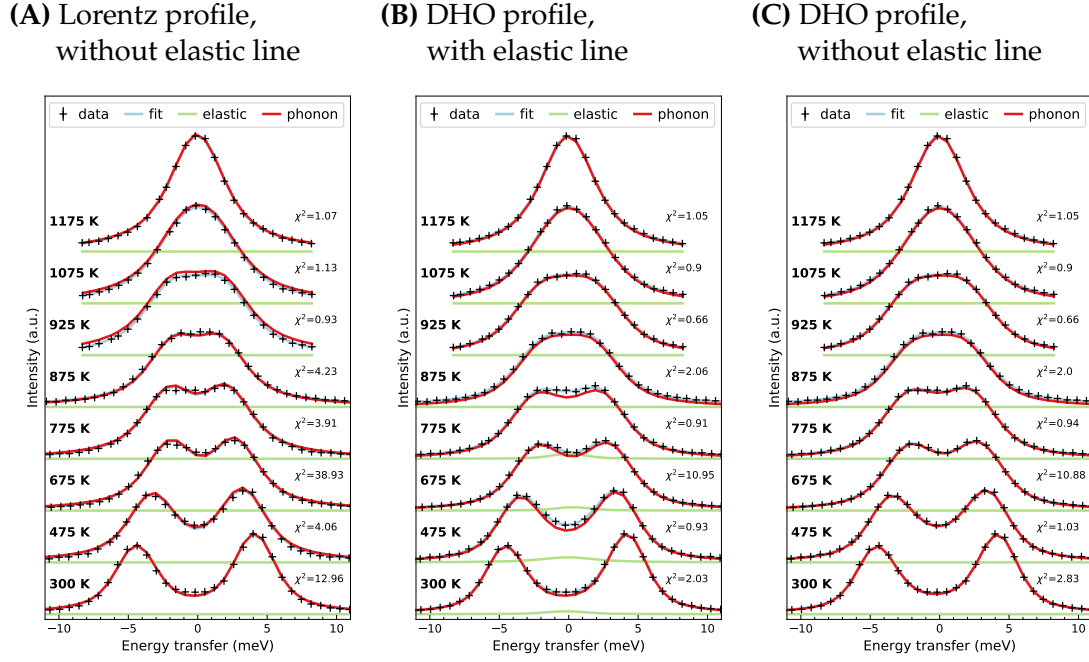


Figure 5.9: IXS spectra measured at the F point at different temperatures, together with the modeled spectrum, described in the inset label. Temperatures at which each scan was acquired are shown on its left side, the quality of the fit indicated by the χ^2 is shown on the right side. Scans were shifted vertically for clarity.

well, a much better quality of the fit can be obtained by employing the damped harmonic oscillator model, DHO, which is typically used to model the excitation of *anharmonic* phonons, see [120, p. 411]. For the DHO model the dynamic structure factor is given as

$$S(\mathbf{Q}, \omega) \propto \frac{\omega}{1 - e^{-\hbar\omega/k_B T}} \frac{\gamma}{(\omega^2 - \omega_0^2)^2 + (\omega\gamma)^2}, \quad (5.1)$$

where the dependence on the wave vector \mathbf{Q} was omitted for clarity, ω_0 is the undamped phonon excitation frequency, and γ is the damping coefficient. All spectra were convoluted with the instrumental resolution function and corrected for the background, as indicated by equation 2.18. The quality of the fit was evaluated by calculating the χ^2 . As shown in Figure 5.9, the χ^2 is much lower for the fits assuming the DHO profile, even though the number of free parameters is the same for the Lorentz profile and the DHO profile. We note here the importance of choosing the proper model function, as it is based on different underlying phenomena. In particular, Figure 5.10 shows the energies and the γ parameter retrieved by fitting different models. For the Lorentzian line-shape γ is the width of the excitation, while for the DHO line-shape γ is the damping coefficient, which denotes the width and apparent softening of the excitation. One sees that for the Lorentz model the energy decreases to zero, while the width of the excitation

increases from less than 1 meV at ambient temperature to 2 meV at 1175 K. This increase in line-width is typical for anharmonic effects. On the other hand, the energy from the DHO model decreases only to 3.2 meV, while the damping coefficient increases up to 9.5 meV, which broadens the excitation and induces an apparent softening.

We note here, that the spectra were deconvoluted with the instrumental resolution, which is a pseudo-Voigt function with a width of ≈ 3 meV. As such, the measured line-width is a sum of the excitation line-width and the instrumental resolution.

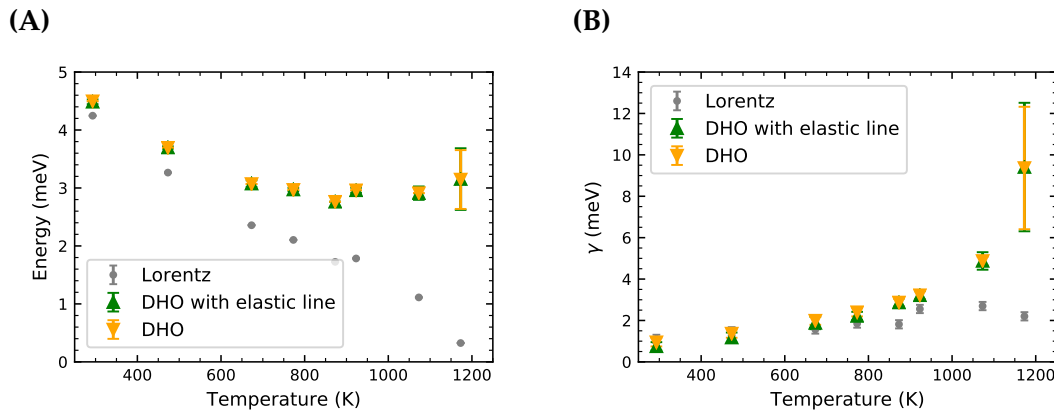


Figure 5.10: Temperature dependence of the soft phonon energy (A) and γ parameter (B) determined by employing different models for measured spectra, as described in the main text. For comparison, the parameters retrieved from the Lorentz fit are marked with small grey symbols, however, they don't denote the real characteristics of the phonon. The errorbars correspond to the precision of the fit.

By fitting all the measured spectra with the DHO model, we determined the dispersion of the Γ - F branch at various temperatures, as shown in Figure 5.11. We observed, that the part of the branch with $\xi > 0.25$ softens with increasing temperature, while the acoustic part, $\xi < 0.25$, doesn't change significantly. As already shown in Figure 5.10, the energy of the F -point phonon decreases from 4.5 meV at ambient temperature to 3.2 meV at 1175 K. Interestingly, we observed a high value of the damping coefficient for phonons with $\xi > 0.25$ at all temperatures, as shown in Figure 5.11.

The IXS results presented here are consistent with the INS measurements reported by Dove et al. [97] (1992) and refined later by Harris et al. [98] (1998). They were the first one to observe the anomalous dispersion of the Γ - F branch, and performed various experiments to determine its high temperature behavior, up to 1100 K. In their experiments they observed a column of inelastic scattering at the F -point manifesting in the appearance of an elastic line in the scans at the F -point. We have fitted our spectra with the elastic line and observed a slight

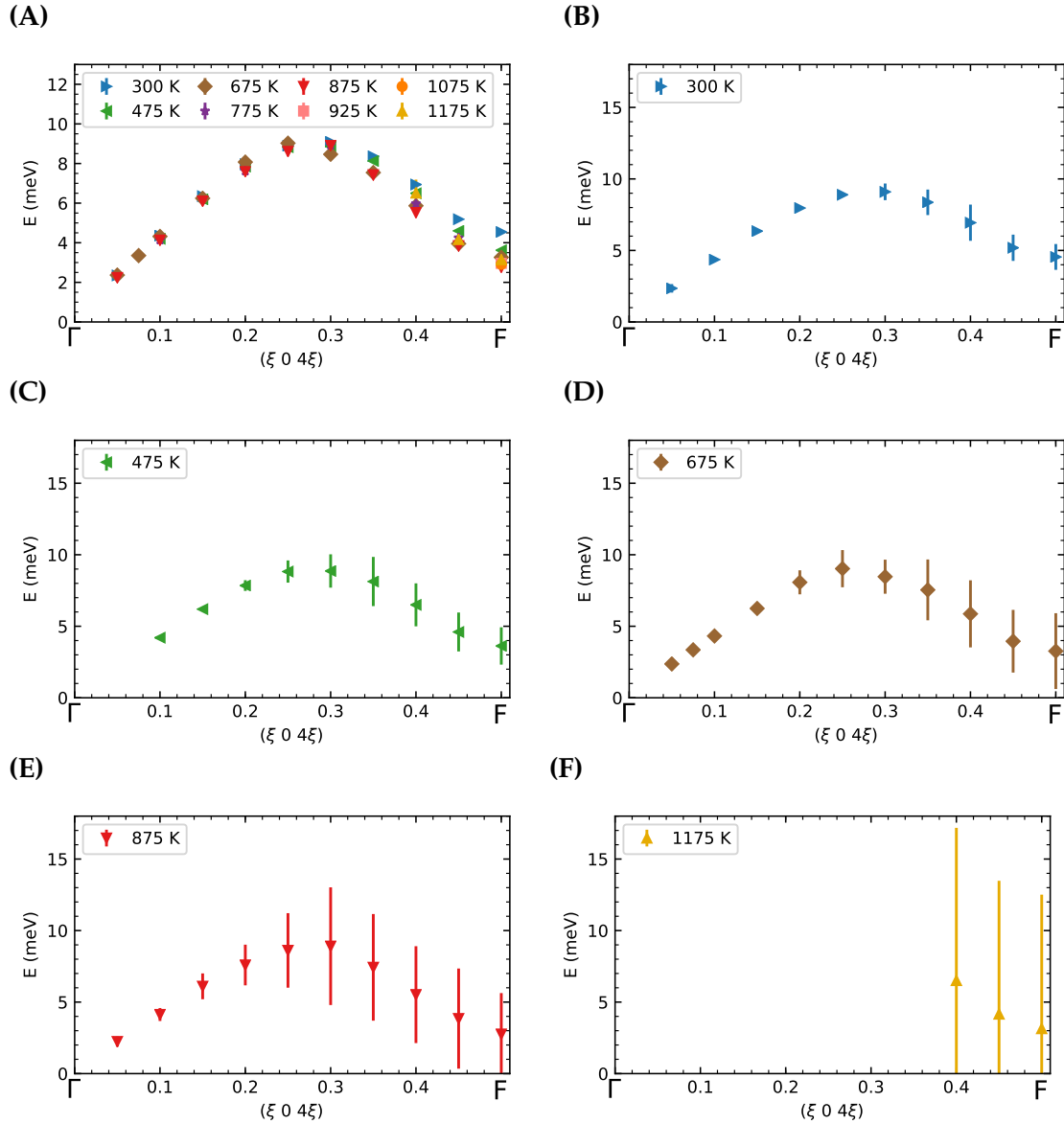


Figure 5.11: (A) Dispersion of the Γ -F branch at high temperatures in calcite. The errors in energy are smaller than the symbol sizes. (B-F) Dispersion of the Γ -F branch at chosen temperatures, with the damping coefficient γ shown as the errorbar.

improvement in the quality of the fit at 300 K, 475 K, and 775 K, see lower χ^2 value in Figure 5.9B compared to Fig. 5.9C, in other cases the quality was the same or actually worse. Therefore we do not confirm their observation of the column of inelastic scattering and consider it an artifact in the data of unknown origin.

5.7 Origin of the high temperature anharmonicity in calcite

The interpretation of the IXS data presented in here can be facilitated by briefly summarizing previous measurements of high temperature lattice dynamics of calcite with other techniques.

Sakurai and Satō [118] measured infrared emissivity of calcite at temperatures up to 1000 K and observed an anharmonic lattice vibration at 37.8 meV at ambient temperature, which energy decreased to 35.2 meV at 1000 K, while the damping increased four times from 300 K to 1000 K. The widths of other measured bands were order of magnitude smaller and their widths increased only three times in from 300 K to 1000 K. Due to the fact that the emissivity spectra are fitted with different function, a direct comparison with damping measured in here is not feasible. Gillet et al. [119] measured Raman scattering of calcite at high temperatures and observed two low-energy anharmonic bands. Their energies at ambient temperature were 19.3 and 34.8 meV, and they decreased to 15.9 and 30 meV at 1000 K. Their widths increased from 10 meV at ambient temperature to 55 meV at 1000 K. They concluded that the observed anharmonic phonons are coupling to the mechanism that is responsible for the transition to calcite-IV phase, which, in light of later findings, is the rotation of the CO₃ groups.

There is an overwhelming number of scientific reports on anharmonic phonon effects, studied mainly by means of Raman spectroscopy. Many theoretical investigations [121–123] explain these effects as the decay of the anharmonic phonon to lower energy phonons. Although such approach can be readily adapted to explain the anharmonic behavior of the high energy phonons observed by Sakurai and Satō [118] and Gillet et al. [119] in calcite, it does not seem to be applicable to the case of the anharmonic *F*-point phonon observed in this study. We have computed the energies of all phonons in the Brillouin zone and realized, that only acoustic phonons with the momentum in the close proximity of the Γ point have lower energies than the *F*-point phonon. However, no pair of acoustic phonons could satisfy both the energy and momentum conservation rules. This shows, that either the *F*-point phonon decays into more than two acoustic phonons, or that its anharmonicity has an origin in a different mechanism.

We are convinced that the latter case holds true. The acoustic phonons in the proximity of the Γ point have an eigenvector that corresponds to a collective translation of all the atoms in the unit cell in a given direction, i.e. an acoustic wave. This movement does not resemble a rotation of a rigid CO₃ group, that defines the eigenvector of the *F*-point phonon, thus the decay into such two translational-like acoustic phonons is unlikely. This hand-waving argument has its basis in the symmetry analysis of the atomic displacement, as the decay products should transform according to the same irreducible representation as the decaying phonon. Unfortunately, a complete symmetry analysis of all possible decay products is a complex task, and beyond the matter of this study. Thus, we limit the analysis to such crude simplification of the symmetry restriction.

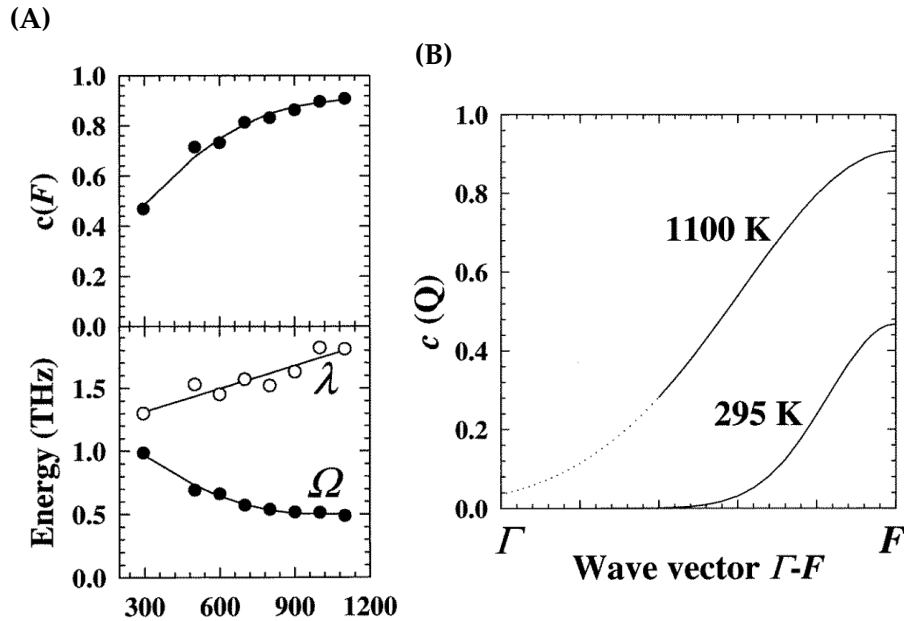


Figure 5.12: (A) F -point phonon frequency Ω , frequency of the relaxational mode λ , and the maximum value of the coupling parameter c . (B) dependence of the coupling parameter $c(Q)$ along the $\Gamma - F$ direction. Data from the INS measurements by Harris et al. [98]. 1 THz = 4.13 meV.

As we have set aside the possibility of a decay of the F -point phonon we continue with the analysis of the results reported by Dove and his collaborators [97, 98]. They have fitted their high-temperature INS data with the expanded DHO model, where the damping originates from the coupling to the relaxational mode, and the coupling parameter can be retrieved from the fit. Figure 5.12 shows their results adapted from Harris et al. [98]. We note that the phonon frequency determined from their model is very similar to the energy measured in this work, they observed the decrease from 4.1 meV (1 THz) at ambient temperature to 2 meV at 1100 K, with a similar „exponential decay“ trend as observed in this work and shown in Figure 5.10. Being biased by the observed column of inelastic scattering from their previous experiments [97], they suggested that the relaxational mode corresponds to the „...dynamical fluctuations into the high-pressure phase [calcite-II]“ [98]. Given the fact that the transition to calcite-II phase involves the collective rotation of the CO_3 groups by 11° and displacement of the Ca atoms along the (104) plane normal, see Chapter 4 and [124], on one hand, and on the other hand that at high temperatures the CO_3 rotate as rigid groups [105], we find it plausible that in small volumes of the crystal the collective thermal displacement of the atoms accidentally resembles the calcite-II structure, and thus forms small domains with short lifetime. In such case, the frequency of the fluctuations would be of the order of atomic vibrations, that is THz, as observed in their results, see Figure 5.12A. The observed column of inelastic scattering could be interpreted as a broad *elastic*

scattering from the weak Bragg reflection of the small calcite-II domains. However, these fluctuations seem to be present also at ambient temperature, see Figure 5.12, as the coupling is non-zero and the frequency of fluctuation is finite at ambient temperature. We find that explanation insufficient, as it does not address the reorientation of the CO_3 groups directly.

Based on the knowledge of the eigenvector of the soft F -point phonon we propose another model for explaining the observed results. We claim that the damping of the Γ - F branch originates from the interaction with the reorientation of the CO_3 groups, which is based on the fact that both the eigenvector of the soft phonon and the reorientation process involve the rotation of the CO_3 groups.

When the particular CO_3 group jumps to the inverse orientation it introduces a local change in the crystal structure, which can be considered as a point defect in the calcite structure, effectively describing the calcite-IV phase. As the eigenvector of the F -point phonon consists of the rotation of the CO_3 groups in the normal orientation, such defect effectively damps the phonon, since the oxygen atoms are afterwards in a different position. In other words we have a scenario of scattering the phonon on the crystal defects, which is common in IXS and INS experiments. It was shown that in such case the spectra are described by the damped harmonic oscillator line-shape [120], which applies very well to the current dataset, as shown in Figure 5.9.

In this scenario the lifetime of the F -point phonon is an average time after which a CO_3 group would reorient to the inverse site. However, with such description we run into the same problem as pointed out for the model of Harris et al. [98], the lifetime of the phonon is relatively short at ambient temperature and it couples to the non-existing reorientation of the CO_3 groups. We improve this model by taking into account the collective variety of anharmonic effects in lattice dynamics, that are responsible for uniform broadening of all phonons. As was shown for a variety of materials [125], the contribution of such anharmonic effects to the profile of the phonon excitation is such, that it lowers the energy and broadens the line-shape of the phonon *linearly* with temperature. Actually, even in case of calcite only few Raman modes show non-linear behavior [119], while the other bands shift and broaden linearly with temperature. In summary, we will describe the damping of the F -point phonon, γ_F , with two components, γ_α linear in temperature, originating from the anharmonic atomic interaction, and γ_D originating from the interaction with reorientation of CO_3 groups, that increases rapidly around the temperature of transition to the calcite-V phase, T_V . As the contributions to the phonon width are additive [120], the total width is $\gamma_F = \gamma_\alpha + \gamma_D$. The fitted damping parameter, γ_F , is shown in Figure 5.13, where its values were taken from the DHO fit without the elastic line, as in Figure 5.9B.

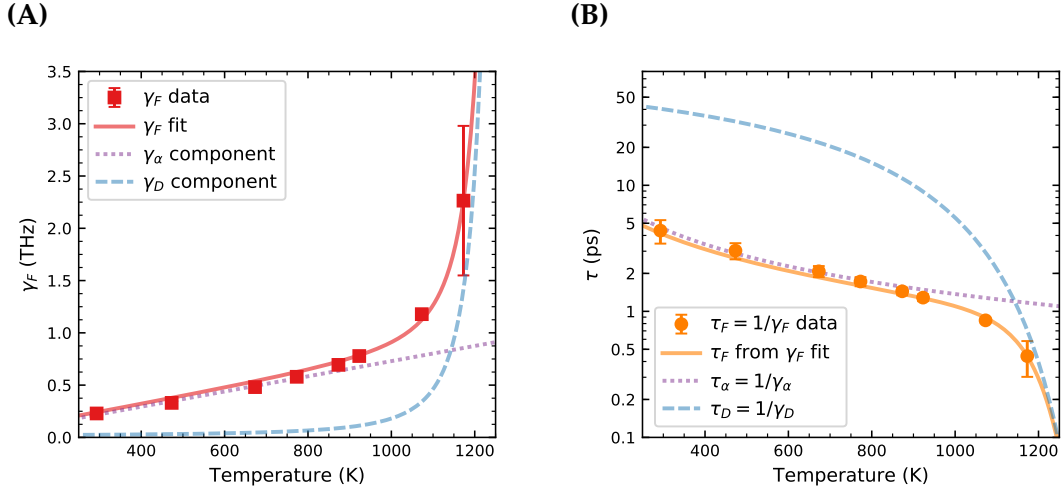


Figure 5.13: Temperature dependence of the F -point phonon (A) damping coefficient γ_F , data points are plotted with red squares, the fit is plotted with red line, and (B) lifetime τ_F , data points are plotted with orange circles, the fit is plotted with orange line. In both cases the fit composes of the contribution from anharmonic effects, purple dotted line, and contribution from the CO_3 groups reorientation, blue dashed line.

We have conveyed a phenomenological analysis of the temperature dependence of γ_D , and concluded that an exponent of inverted temperature, $\exp(1/(1 - T/T_0))$, describes it very well. We have taken into account various functions and varied the extent to which the linear contribution is dominant, with details presented in Appendix C. As shown in Figure 5.13A, the contribution from γ_D becomes significant around 1000 K, and is dominant above 1150 K. This is consistent with the fact, that the reorientation of the CO_3 groups does not occur below $T_{IV} = 985$ K. By inverting the damping parameter, we obtain the lifetime of the phonon [120]. The contribution to the phonon lifetime is given as $1/\tau_F = 1/\tau_\alpha + 1/\tau_D$, from which it follows that $\tau_F = \tau_\alpha \tau_D / (\tau_\alpha + \tau_D)$. The deconvoluted contributions to the measured phonon lifetime are shown in Figure 5.13B. As was stated before, current model assumes that the finite lifetime, derived from damping, originates from a sum of anharmonic interaction and CO_3 groups reorientation. As such, the parameter τ_D can be interpreted as an average time a CO_3 group occupies the normal orientation, after which it would jump to the inverse orientation, thus introducing a point defect. Further on τ_D will be called the occupation time, and $1/\tau_D = \mu_D$ the reorientation frequency.

We see that at ambient temperature the lifetime of the phonon is around 5 ps, and has a major contribution from the anharmonic lattice interactions, as the occupation time is an order of magnitude larger. Around 1000 K, the reorientation frequency is high enough to give a significant contribution to the lifetime, and we are able to determine that the occupation time is of the order of 10 ps. At the

highest temperature measured in this study, 1175 K, γ_F has a minor contribution from the anharmonic effects and the occupation time is of the order of 1 ps. Close to the transition temperature $T_V = 1240$ K the occupation time decreases down to 0.1 ps.

Within the model established here the temperature evolution of the reorientation of the CO_3 groups in calcite can be summarized as follows. At ambient temperature the reorientation does not occur, the width of the F -point phonon is slightly broader than the instrumental resolution, which is due to some collective anharmonic interactions. As the temperature increases the lattice expands in a way, which causes a slight damping and broadening of the F -point phonon. At the same time the potential barrier for occupying the inverse orientation decreases, however its still high enough to prevent the reorientation of the CO_3 groups, see Figure 5.2. At $T_{IV}=985$ K, due to an unknown mechanism, the potential barrier drops significantly, see Figure 5.2A, which allows a significant fraction of CO_3 groups to reorient to the inverse site, as they have enough thermal energy to overcome the potential barrier. This reorientation accounts for an additional contribution to the phonon width, as observed in our measurements. Upon further temperature increase the potential barrier decreases even more, which allows higher fraction of CO_3 groups to reorient, so that above 1150 K the lifetime of the F -point phonon is significantly reduced.

The transition temperature marks the extent to which the current model can be applied. Above the transition the CO_3 groups rotate with finite frequency, where lattice dynamics can be described by the rotational-translational coupling formalism, as established by Lynden-Bell and Michel [126]. They have shown that in such case two scenarios are possible, either the reorientation frequency of the rotor is significantly lower than the coupled phonon frequency, or significantly higher. In the former case the phonon spectrum will possess an emerging elastic line, as in the case of KCN [127]. In the latter case, the background signal is increasing and a softening of the phonon is observed. We have excluded the possibility for the existence of an elastic line in calcite, see Figure 5.9, and observed a significant softening of the phonon. Thus, the second scenario applies to the calcite-V case, where the frequency of the CO_3 groups reorientation is significantly faster than the frequency of the coupled F -point phonon. This finds quantitative confirmation in the current data, as at ≈ 1240 K the reorientation frequency is $1/0.1 \text{ ps} = 10 \text{ THz}$ which is significantly higher than the frequency of the F -point phonon 0.72 THz, that corresponds to 3 meV.

At last, we take a step back to revisit the characteristics of the whole Γ - F branch. Just like in the case of the F -point phonon we have investigated the displacement pattern of the acoustic phonons of the Γ - F branch. First we have

constructed a vector describing the rotation of the CO₃ groups by taking the eigenvector of the soft F -point phonon, with the displacement of the Ca and C atoms set to zero. Next, we multiply it with the eigenvectors of the acoustic phonons in the Γ - F direction. The resulting quantity, the projection of the eigenvector, allows to quantify how much the eigenvector of a specific phonon resembles the rotation of the CO₃ groups. Figure 5.14 shows the calculated projection. Such depiction shows the change in the character of the eigenvector of the anomalous branch, where from $\xi \approx 0.25$ the displacement pattern resembles the rotation of the CO₃ groups much more than for the shorter wave vectors. At the same ξ , the Γ - F branch starts to soften, see Figure 5.11A, which leads us to the conclusion, that the anomalous behavior originates from coupling of the branch to the rotational disorder of the CO₃ groups. We note here that the trend of the eigenvector projection strongly resembles the profile of the coupling parameter reported by [98], shown in Figure 5.12B.

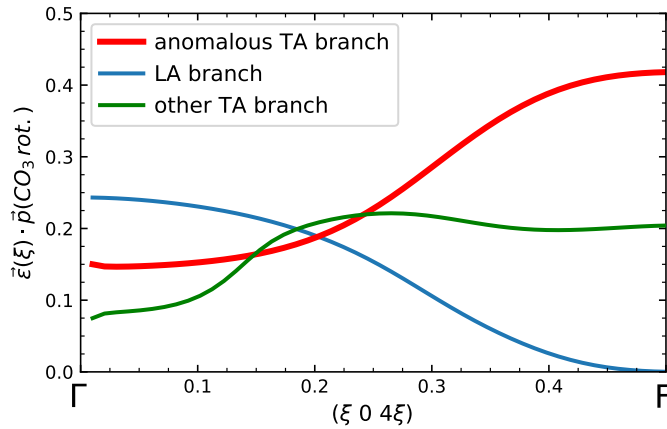


Figure 5.14: Scalar product of the Γ - F acoustic phonons eigenvectors, $\vec{\epsilon}(\xi)$, and the vector describing the rotation of the CO₃ groups, $\vec{p}(CO_3 \text{ rot.})$. Note, that the $\vec{p}(CO_3 \text{ rot.})$ is not an eigenvector of the F point, thus its scalar product with non-anomalous branch at the F -point is not zero, and the product with anomalous branch is not one.

5.8 Comparison of the CO₃ reorientation in calcite with other systems

The interconnection between rotational disorder and lattice vibrations is a relatively well studied field, with a thorough theoretical review [126], and numerous experimental reports cited within. In order to provide some perspective on the results presented here on calcite we compare them to other examples known in literature.

There exists a wide range of materials known plastic crystals, which are defined as an ordered lattice of weakly interacting molecules. In the review study

of Brand et al. [128] six different organic plastic crystals were investigated, and it was shown that at ambient temperature the reorientation frequency spans the range from 10^5 to 10^{10} Hz, increases with temperature and decreases with higher moment of inertia of the molecule. It was also shown that the reorientation frequency can shift by orders of magnitude across a hundred Kelvins. Since the investigated molecules were heavier than a CO_3 group, the results of Brand et al. [128] are consistent with the one presented here, where we have shown that the frequency of reorientation increases from 10^{12} Hz at 1150 K, to 10^{13} Hz at 1250 K.

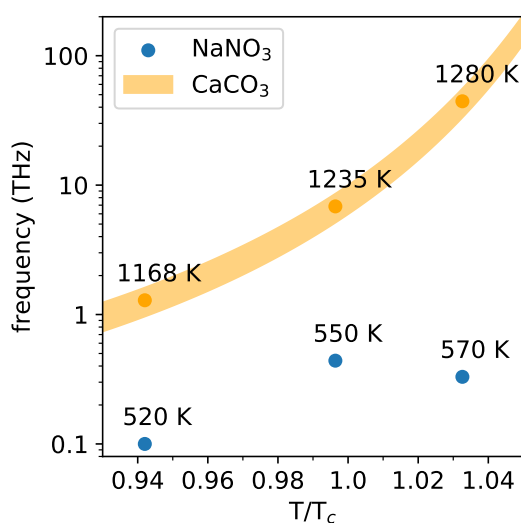


Figure 5.15: Comparison of the reorientation frequency in CaCO_3 and NaNO_3 . Data for CaCO_3 come from this study with the error given as the width of the line, data for NaNO_3 are from the calculations reported by Lynden-Bell et al. [129] and Liu et al. [130].

A direct comparison can be conducted with NaNO_3 . It is isostructural with calcite and undergoes the same order-disorder transition as calcite, driven by reorientation of the NO_3 groups [131]. Due to the fact that the reorientation takes place at lower temperatures, 552 K [131, 132], and it does not involve producing a reactive CO_2 , the reorientation of the NO_3 groups in NaNO_3 was studied in far more details experimentally [131–135]. These studies allowed to perform a well constrained molecular dynamics calculations, which showed that the average reorientation frequency is around 0.1 THz at 520 K and 0.33 THz at 570 K as reported by Lynden-Bell et al. [129] (1989) and 0.44 THz at 550 K as reported by Liu et al. [130] (2001). We have calculated the reorientation frequency in calcite at equivalent temperatures, rescaled as T/T_c , where T_c is the transition temperature, with the results shown in Figure 5.15. 0.1 THz at 520 K in NaNO_3 corresponds to 1.2 THz at 1165 K in CaCO_3 , 0.44 THz at 550 K to 6.7 THz at 1235 K, and 0.33 THz at 570 K to 43 THz at 1280 K. We have estimated that the error of the reorientation time in calcite is around 25%, while it is unknown for NaNO_3 . In conclusion the reorientation

frequency is an order of magnitude higher in calcite before the transition and two orders of magnitude higher after the transition. An order of magnitude difference in the reorientation frequency is rather unexpected, as the study on plastic crystals [128] showed, that the reorientation frequency is a universal function of rescaled temperature T/T_C , i.e. the reorientation frequencies should be the same for calcite and NaNO_3 , especially since the rotating molecule is the same. It is possible that the calculations for NaNO_3 are not accurate and introduce a systematic error. The two reports [129] and [130] are definitely not consistent, as the reorientation frequency should increase with increasing temperature, while it is slightly lower at 570 K (0.33 THz), than at 550 K (0.44 THz), thus their accuracy is questionable. In addition, the difference in the reorientation frequencies could be connected to the fact that the transition in calcite takes place at higher temperatures, where by the energy equipartition theorem at $T_c = 1240$ K CO_3 groups have higher kinetic energy than NO_3 groups at $T_c = 552$ K. In conclusion, this effect requires a more thorough investigation and the question on the origin of this difference remains open.

5.9 Conclusions

As shown in the current study, the high temperature lattice dynamics of calcite is strongly connected to the behaviour of the transverse acoustic F -point phonon, which was also the case at high pressure, presented in Chapter 4. We have employed a simple model of treating the rotational disorder of the CO_3 groups as point defects, which leads to anharmonic interactions with the anomalous part of the Γ - F branch, resulting in apparent softening of the branch at high temperatures. We presented a quantitative description of the model and were able to retrieve the frequency of the CO_3 groups reorientation.

6

Summary and outlook

In the scope of the project summarized in this thesis a variety of carbonates and their physical properties were investigated at high pressures and high temperatures. The main focus was put on their lattice dynamics and the connection to their phase transitions.

Chapter 3 presents the results of the study on high pressure elastic properties of the magnesium-iron family of carbonates. The results of a high-pressure IXS experiment of siderite were presented, which were used to derive the C_{33} and C_{44} elastic moduli. Complementary DFT based calculations were performed, so that a full elastic tensor could be determined at pressures up to 60 GPa. We have combined our results with data published on MgCO_3 [72] and $\text{Mg}_{0.35}\text{Fe}_{0.65}\text{CO}_3$ [55], in order to provide a dataset, that could describe the elastic properties for any composition and pressure for the $\text{Mg}_{1-x}\text{Fe}_x\text{CO}_3$ family of carbonates up to 60 GPa. A detailed analysis was presented in Chapter 3, the obtained dataset was encapsulated in form of a python script, given in Appendix A, that provides a function which returns the elastic tensor for a given composition and pressure. The dataset was employed to determine the seismic signature of the Mg,Fe-carbonates in the Earth's mantle. We investigated how the spin transition affects the sound velocities, what amounts of Mg,Fe-carbonate would produce a significant velocity contrast, and how the texture in subducted carbonates would affect the average sound velocities.

Chapters 4 and 5 are closely related, as they are both dedicated to study the phonon anomaly in calcite, which manifests in softening of the transverse acoustic Γ - F branch, upon approaching the edge of the Brillouin zone. In Chapter 4 the anomaly was investigated for a variety of carbonates at ambient and high pressure by a combination of TDS, IXS and DFT calculations. It was shown that the anomalous part of the transverse acoustic Γ - F branch softens under pressure in both calcite and dolomite. In particular, in calcite the energy of the phonon at the F point decreases to zero at 1.8 GPa, which marks the transition to the calcite-II

structure. In dolomite the energy of the F -point phonon decreases systematically upon pressure increase to 7 GPa. The extrapolation of the softening in dolomite shows that the phonon's energy would decrease to zero at 17.5 GPa, which marks the transition to dolomite-II. The eigenvector of the softening F -point phonon was determined by DFT calculations in both carbonates, and was found to be identical to the atomic displacement due to the transition to calcite-II, and very similar in case of dolomite-II. This allowed to conclude that both transition are soft-phonon driven. The anomaly was also studied in other carbonates: magnesite, siderite, smithsonite and otavite, in order to determine the underlying physical mechanism responsible for the anomalous dispersion of the Γ - F branch.

Chapter 5 showed the complementary study on calcite, where the F -point anomaly was investigated at high temperatures. Due to the thermal decomposition of calcite and high reactivity of CO_2 at high temperatures, a custom designed sample environment was used. It allowed to measure the IXS spectra of the dynamically disordered calcite-IV phase, where the CO_3 groups can jump to the reverse site by a 60° rotation. It was observed that the anomalous F -point phonon couples to the disorder, which was indicated by softening and broadening of the phonon. The application of the model that treats the disorder as point defects, with the F -point phonon being scattered on such defects, allowed to determine the time-scale of the reorientation of the CO_3 groups by a careful analysis of the lineshape of the IXS spectra. It was shown that in the calcite-IV phase the CO_3 groups stay in a certain orientation for few picoseconds on average, and the time decreases with increasing temperature. This picture was found to be fully consistent with the transition to calcite-V at 1240 K, where the CO_3 groups are freely rotating.

Outlook

Although many questions were answered in this study many more remain open. The most important ones resolve around the application of current results to the domain of geoscience, in order to model and understand the processes that govern the deep carbon cycle.

Few of such questions were tackled in Chapter 3, with rather pessimistic conclusions. Current cutting-edge seismic tomography methods are able to resolve big objects, like subducting slabs, but applying them as to constrain the composition of Earth's interior, which was one of the attempts in Chapter 3, seems beyond current possibilities. The next step in this project would be to determine the elastic tensor of Mg-Fe carbonate at high pressure *and* high temperature. Such

experiments are rather complicated, however they could unravel some unexpected properties of carbonate at high temperature.

Chapter 4 showed that the transitions calcite \rightarrow calcite-II and dolomite \rightarrow dolomite-II are driven by a soft phonon, and that only carbonates with a relatively big anion, Ca^{2+} or Cd^{2+} , will adapt the calcite-II phase at high pressure. However, it was not fully understood why calcite-II is metastable, while dolomite-II is stable. An attempt to shed light on the structure of magnesite-II phase was made, however calculations can not compete with the proper experimental data. The structure of magnesite-II still awaits to be determined, and the mechanism of its transition to be understood.

Finally, the connection between the dynamic rotational disorder and lattice dynamics of calcite was established in Chapter 5. It was shown how the rotational disorder affects the F -point phonon, but it was beyond the current study to elucidate on the origin of the rotational disorder. Since it's a collective movement of specific atoms it seems that it could also be caused by some phonon instability. The rotational disorder could be understood even better if it was studied in other carbonates, where the influence of the cation site on the disorder could be determined. However, there is no direct experimental evidence of dynamically disordered phases in other carbonates.

The combination of thermal diffuse scattering, inelastic x-ray scattering and density functional based calculations was applied here to understand the mechanism of the phase transitions in carbonates and determine their physical properties. Nevertheless the combination of these methods is systematically used to study a broad range of materials that are of interest for various branches of science. In particular, one of the most important recent developments in x-ray based techniques is the construction of the hybrid detectors, with high dynamic range and a single pixel spread function, like the Pilatus detector used in this study. These detectors become more affordable each year, and are quickly becoming a standard in synchrotron facilities. It is anticipated that in the near future that they will also become standard detectors in the laboratory diffractometers, so that the diffuse scattering studies will be conducted on much larger scale.

A

Source code for determining the elastic tensor of $(\text{Mg,Fe})\text{CO}_3$

The following source code allows to determine the elastic stiffness coefficients of $\text{Mg}_{1-x}\text{Fe}_x\text{CO}_3$ for any composition, x , at pressures up to 60 GPa, based on the data presented in Chapter 4. It is written in python2.7 language, and gives a minimal example for reproducing the Figure 3.10. All elastic properties presented in Chapter 4 were determined based on this source code and additional scripts.

```
1 import numpy as np
2 import matplotlib as mpl
3 import matplotlib.pyplot as plt
4 import matplotlib.cm as cm
5
6 #####
7 ##### Hard-coded Cij #####
8 #####
9
10 def C11_00(x): return 259.806000 + x*(-31.876000)
11 def C33_00(x): return 152.624000 + x*(-31.419000)
12 def C44_00(x): return 57.668000 + x*(-18.680200)
13 def C12_00(x): return 70.726300 + x*(34.502500)
14 def C13_00(x): return 59.559900 + x*(8.552540)
15 def C14_00(x): return 19.727600 + x*(-6.338140)
16 def C11_10(x): return 338.806000 + x*(-34.931100)
17 def C33_10(x): return 194.931000 + x*(-41.009800)
18 def C44_10(x): return 77.675200 + x*(-18.997600)
19 def C12_10(x): return 101.949000 + x*(28.832300)
20 def C13_10(x): return 97.015100 + x*(13.525600)
21 def C14_10(x): return 31.206600 + x*(-3.308140)
22 def C11_20(x): return 409.100000 + x*(-56.355300)
23 def C33_20(x): return 237.637000 + x*(-50.629600)
24 def C44_20(x): return 96.580100 + x*(-19.991000)
25 def C12_20(x): return 135.213000 + x*(42.083500)
26 def C13_20(x): return 133.074000 + x*(17.182800)
27 def C14_20(x): return 41.444300 + x*(-2.613800)
28 def C11_30(x): return 461.301000 + x*(-27.909500)
29 def C33_30(x): return 278.400000 + x*(-61.346100)
30 def C44_30(x): return 112.698000 + x*(-20.451500)
31 def C12_30(x): return 170.444000 + x*(47.867700)
32 def C13_30(x): return 167.731000 + x*(15.760000)
33 def C14_30(x): return 50.141000 + x*(-1.112610)
34 def C11_HS_40(x): return 520.883000 + x*(-51.726600)
```

```

35 def C33_HS_40(x): return 317.058000 + x*(-66.502700)
36 def C44_HS_40(x): return 128.733000 + x*(-21.222800)
37 def C12_HS_40(x): return 203.180000 + x*(43.217700)
38 def C13_HS_40(x): return 203.835000 + x*(7.024980)
39 def C14_HS_40(x): return 57.911600 + x*(1.107860)
40 def C11_LS_40(x): return 525.600000 + x*(114.400000)
41 def C33_LS_40(x): return 327.040000 + x*(38.360000)
42 def C44_LS_40(x): return 128.700000 + x*(46.800000)
43 def C12_LS_40(x): return 189.450000 + x*(38.550000)
44 def C13_LS_40(x): return 204.390000 + x*(25.610000)
45 def C14_LS_40(x): return 58.060000 + x*(17.740000)
46 def C11_50(x): return 580.201000 + x*(121.749000)
47 def C33_50(x): return 350.529000 + x*(7.544610)
48 def C44_50(x): return 142.161000 + x*(49.563200)
49 def C12_50(x): return 228.984000 + x*(53.273200)
50 def C13_50(x): return 230.745000 + x*(21.680600)
51 def C14_50(x): return 66.880900 + x*(22.103000)
52 def C11_60(x): return 629.417000 + x*(118.739000)
53 def C33_60(x): return 405.245000 + x*(22.225300)
54 def C44_60(x): return 153.820000 + x*(58.851700)
55 def C12_60(x): return 279.769000 + x*(30.559600)
56 def C13_60(x): return 280.584000 + x*(19.882000)
57 def C14_60(x): return 75.723800 + x*(22.562900)
58
59 #####
60 ##### Wrappers #####
61 #####
62
63 def C_MgFeCO3(P, x):
64     C11 = (C11_00(x) + (P-00.0)*(C11_10(x)-C11_00(x))/10.0)*(P>=0)*(P<=10) + \
65           (C11_10(x) + (P-10.0)*(C11_20(x)-C11_10(x))/10.0)*(P>10)*(P<=20) + \
66           (C11_20(x) + (P-20.0)*(C11_30(x)-C11_20(x))/10.0)*(P>20)*(P<=30) + \
67           (C11_30(x) + (P-30.0)*(C11_HS_40(x)-C11_30(x))/10.0)*(P>30)*(P<=40) + \
68           (C11_LS_40(x) + (P-40.0)*(C11_50(x)-C11_LS_40(x))/10.0)*(P>40)*(P<=50) + \
69           (C11_50(x) + (P-50.0)*(C11_60(x)-C11_50(x))/10.0)*(P>50)*(P<=60)
70
71     C33 = (C33_00(x) + (P-00.0)*(C33_10(x)-C33_00(x))/10.0)*(P>=0)*(P<=10) + \
72           (C33_10(x) + (P-10.0)*(C33_20(x)-C33_10(x))/10.0)*(P>10)*(P<=20) + \
73           (C33_20(x) + (P-20.0)*(C33_30(x)-C33_20(x))/10.0)*(P>20)*(P<=30) + \
74           (C33_30(x) + (P-30.0)*(C33_HS_40(x)-C33_30(x))/10.0)*(P>30)*(P<=40) + \
75           (C33_LS_40(x) + (P-40.0)*(C33_50(x)-C33_LS_40(x))/10.0)*(P>40)*(P<=50) + \
76           (C33_50(x) + (P-50.0)*(C33_60(x)-C33_50(x))/10.0)*(P>50)*(P<=60)
77
78     C44 = (C44_00(x) + (P-00.0)*(C44_10(x)-C44_00(x))/10.0)*(P>=0)*(P<=10) + \
79           (C44_10(x) + (P-10.0)*(C44_20(x)-C44_10(x))/10.0)*(P>10)*(P<=20) + \
80           (C44_20(x) + (P-20.0)*(C44_30(x)-C44_20(x))/10.0)*(P>20)*(P<=30) + \
81           (C44_30(x) + (P-30.0)*(C44_HS_40(x)-C44_30(x))/10.0)*(P>30)*(P<=40) + \
82           (C44_LS_40(x) + (P-40.0)*(C44_50(x)-C44_LS_40(x))/10.0)*(P>40)*(P<=50) + \
83           (C44_50(x) + (P-50.0)*(C44_60(x)-C44_50(x))/10.0)*(P>50)*(P<=60)
84
85     C12 = (C12_00(x) + (P-00.0)*(C12_10(x)-C12_00(x))/10.0)*(P>=0)*(P<=10) + \
86           (C12_10(x) + (P-10.0)*(C12_20(x)-C12_10(x))/10.0)*(P>10)*(P<=20) + \
87           (C12_20(x) + (P-20.0)*(C12_30(x)-C12_20(x))/10.0)*(P>20)*(P<=30) + \
88           (C12_30(x) + (P-30.0)*(C12_HS_40(x)-C12_30(x))/10.0)*(P>30)*(P<=40) + \
89           (C12_LS_40(x) + (P-40.0)*(C12_50(x)-C12_LS_40(x))/10.0)*(P>40)*(P<=50) + \
90           (C12_50(x) + (P-50.0)*(C12_60(x)-C12_50(x))/10.0)*(P>50)*(P<=60)
91
92     C13 = (C13_00(x) + (P-00.0)*(C13_10(x)-C13_00(x))/10.0)*(P>=0)*(P<=10) + \
93           (C13_10(x) + (P-10.0)*(C13_20(x)-C13_10(x))/10.0)*(P>10)*(P<=20) + \

```

```

94         (C13_20(x) + (P-20.0)*(C13_30(x)-C13_20(x))/10.0)*(P>20)*(P<=30) + \
95         (C13_30(x) + (P-30.0)*(C13_HS_40(x)-C13_30(x))/10.0)*(P>30)*(P<=40) + \
96         (C13_LS_40(x) + (P-40.0)*(C13_50(x)-C13_LS_40(x))/10.0)*(P>40)*(P<=50) + \
97         (C13_50(x) + (P-50.0)*(C13_60(x)-C13_50(x))/10.0)*(P>50)*(P<=60)
98
99     C14 = (C14_00(x) + (P-00.0)*(C14_10(x)-C14_00(x))/10.0)*(P>=0)*(P<=10) + \
100         (C14_10(x) + (P-10.0)*(C14_20(x)-C14_10(x))/10.0)*(P>10)*(P<=20) + \
101         (C14_20(x) + (P-20.0)*(C14_30(x)-C14_20(x))/10.0)*(P>20)*(P<=30) + \
102         (C14_30(x) + (P-30.0)*(C14_HS_40(x)-C14_30(x))/10.0)*(P>30)*(P<=40) + \
103         (C14_LS_40(x) + (P-40.0)*(C14_50(x)-C14_LS_40(x))/10.0)*(P>40)*(P<=50) + \
104         (C14_50(x) + (P-50.0)*(C14_60(x)-C14_50(x))/10.0)*(P>50)*(P<=60)
105
106     return np.array([C11, C33, C44, C12, C13, C14])
107
108 def ro_MgFeCO3(P, x):
109     ro_MgCO3 = [3.02173, 3.26650, 3.45206, 3.61758, 3.77494, 3.90723, 4.02806]
110     ##### 00 HS, 10 HS, 20 HS, 30 HS, 40 HS, 40 LS, 50 LS, 60 LS
111     ro_FeCO3 = [3.757, 4.089, 4.353, 4.58, 4.78, 5.311, 5.478, 5.631]
112
113     ro_MgCO3_P = (ro_MgCO3[0]+(P-0.0)/10.0*(ro_MgCO3[1]-ro_MgCO3[0]))*(P>=0)*(P<=10) + \
114         (ro_MgCO3[1]+(P-10.0)/10.0*(ro_MgCO3[2]-ro_MgCO3[1]))*(P>10)*(P<=20) + \
115         (ro_MgCO3[2]+(P-20.0)/10.0*(ro_MgCO3[3]-ro_MgCO3[2]))*(P>20)*(P<=30) + \
116         (ro_MgCO3[3]+(P-30.0)/10.0*(ro_MgCO3[4]-ro_MgCO3[3]))*(P>30)*(P<=40) + \
117         (ro_MgCO3[4]+(P-40.0)/10.0*(ro_MgCO3[5]-ro_MgCO3[4]))*(P>40)*(P<=50) + \
118         (ro_MgCO3[5]+(P-50.0)/10.0*(ro_MgCO3[6]-ro_MgCO3[5]))*(P>50)*(P<=60)
119
120     # HS-LS transition in lines 17-18
121     ro_FeCO3_P = (ro_FeCO3[0]+(P-0.0)/10.0*(ro_FeCO3[1]-ro_FeCO3[0]))*(P>=0)*(P<=10) + \
122         (ro_FeCO3[1]+(P-10.0)/10.0*(ro_FeCO3[2]-ro_FeCO3[1]))*(P>10)*(P<=20) + \
123         (ro_FeCO3[2]+(P-20.0)/10.0*(ro_FeCO3[3]-ro_FeCO3[2]))*(P>20)*(P<=30) + \
124         (ro_FeCO3[3]+(P-30.0)/10.0*(ro_FeCO3[4]-ro_FeCO3[3]))*(P>30)*(P<=40) + \
125         (ro_FeCO3[5]+(P-40.0)/10.0*(ro_FeCO3[6]-ro_FeCO3[5]))*(P>40)*(P<=50) + \
126         (ro_FeCO3[6]+(P-50.0)/10.0*(ro_FeCO3[7]-ro_FeCO3[6]))*(P>50)*(P<=60)
127
128     return (1-x)*ro_MgCO3_P + x*ro_FeCO3_P
129
130     #####
131     ##### Heatmaps #####
132     #####
133
134     if True:
135         pressure = np.linspace(0, 60, 121)
136         composit = np.linspace(0, 1.0, 41)
137         P,X = np.meshgrid(pressure, composit)
138         Cfull = C_MgFeCO3(P,X)
139         C11, C33, C44, C12, C13, C14 = Cfull
140
141         fig, axes = plt.subplots(2,3)
142
143         plt.rcParams.update({'font.size': 9})
144         plt.rcParams.update({'xtick.labelsize': 'small'})
145
146         mapColor = cm.afmhot
147
148         im = axes[0,0].pcolor(P, X, C11, cmap=mapColor, \
149             vmin=abs(C11).min(), vmax=abs(C11).max())
150         fig.colorbar(im, ax=axes[0,0])
151         axes[0,0].set_title("$\mathbf{C_{11}}$")
152         axes[0,0].set_ylabel("x")

```

```
153
154     im = axes[0,1].pcolor(P, X, C33, cmap=mapColor, \
155         vmin=abs(C33).min(), vmax=abs(C33).max())
156     fig.colorbar(im, ax=axes[0,1])
157     axes[0,1].set_title("$\mathbf{C}_{33}$")
158
159     im = axes[0,2].pcolor(P, X, C44, cmap=mapColor, \
160         vmin=abs(C44).min(), vmax=abs(C44).max())
161     fig.colorbar(im, ax=axes[0,2])
162     axes[0,2].set_title("$\mathbf{C}_{44}$")
163
164     im = axes[1,0].pcolor(P, X, C12, cmap=mapColor, \
165         vmin=abs(C12).min(), vmax=abs(C12).max())
166     fig.colorbar(im, ax=axes[1,0])
167     axes[1,0].set_title("$\mathbf{C}_{12}$")
168     axes[1,0].set_ylabel("x")
169     axes[1,0].set_xlabel("pressure (GPa)")
170
171     im = axes[1,1].pcolor(P, X, C13, cmap=mapColor, \
172         vmin=abs(C13).min(), vmax=abs(C13).max())
173     fig.colorbar(im, ax=axes[1,1])
174     axes[1,1].set_title("$\mathbf{C}_{13}$")
175     axes[1,1].set_xlabel("pressure (GPa)")
176
177     im = axes[1,2].pcolor(P, X, C14, cmap=mapColor, \
178         vmin=abs(C14).min(), vmax=abs(C14).max())
179     fig.colorbar(im, ax=axes[1,2])
180     axes[1,2].set_title("$\mathbf{C}_{14}$")
181     axes[1,2].set_xlabel("pressure (GPa)")
182
183     plt.tight_layout()
184
185     plt.savefig('MgFeCO3-Cij-heatmap.pdf')
186     plt.savefig('MgFeCO3-Cij-heatmap.eps')
187     plt.savefig('MgFeCO3-Cij-heatmap.png', dpi=500)
```

B Dispersion relations of calcite, dolomite, and magnesite

Phonon dispersion relations were calculated on a path presented in Figure B.1, with the coordinates of the special points listed in table B.1. The dispersion relation measured by IXS and presented in Chapter 4 were determined for the direction between the Γ point and the F point of the neighboring Brillouin zone, as shown in figure B.1.

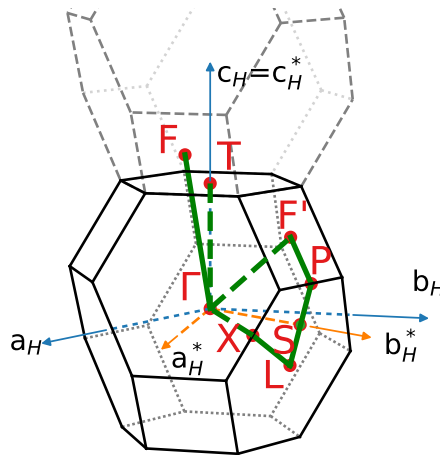


Figure B.1: The first Brillouin zone of calcite, dolomite, and magnesite. The green line shows the path on which phonon dispersion relations were calculated.

Table B.1: Naming and coordinates of special points in the Brillouin zone of rhombohedral carbonates.

label	rhombohedral	hexagonal	label	rhombohedral	hexagonal
T	$(\frac{1}{2} \frac{1}{2} \frac{1}{2})$	$(0 \ 0 \ \frac{3}{2})$	S	$(\frac{3}{16} \ \frac{3}{16} \ -\frac{3}{8})$	$(0 \ \frac{9}{16} \ 0)$
Γ	$(0 \ 0 \ 0)$	$(0 \ 0 \ 0)$	L	$(0 \ 0 \ -\frac{1}{2})$	$(0 \ \frac{1}{2} \ -\frac{1}{2})$
F'	$(\frac{1}{2} \ \frac{1}{2} \ 0)$	$(0 \ \frac{1}{2} \ 1)$	X	$(\frac{3}{8} \ 0 \ -\frac{3}{8})$	$(\frac{3}{8} \ \frac{3}{8} \ 0)$
P	$(\frac{3}{8} \ \frac{3}{8} \ -\frac{1}{4})$	$(0 \ \frac{5}{8} \ \frac{1}{2})$	F	$(1 \ \frac{1}{2} \ \frac{1}{2})$	$(\frac{1}{2} \ 0 \ 2)$

Calcite

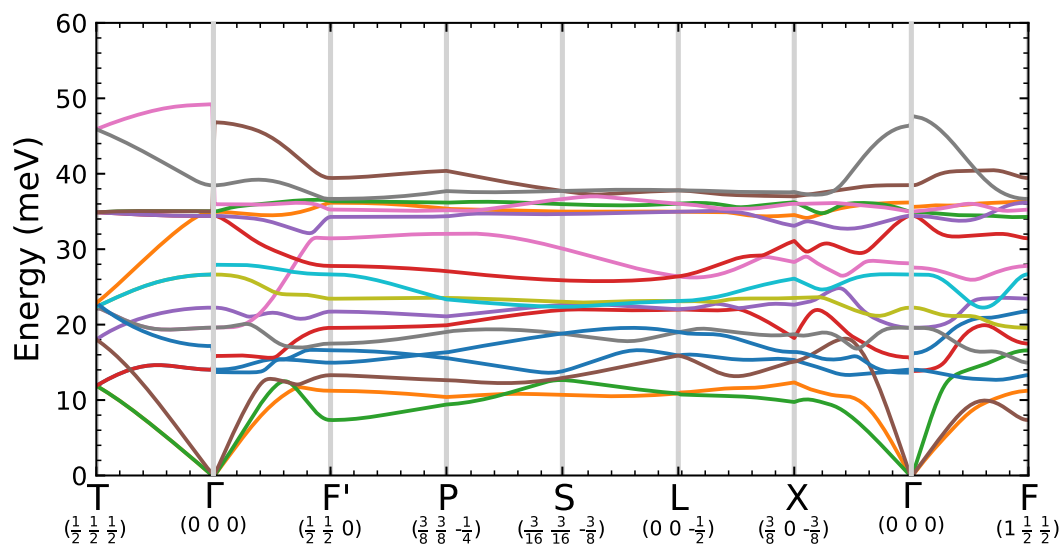


Figure B.2: Low energy phonon dispersion relations in calcite at ambient pressure.

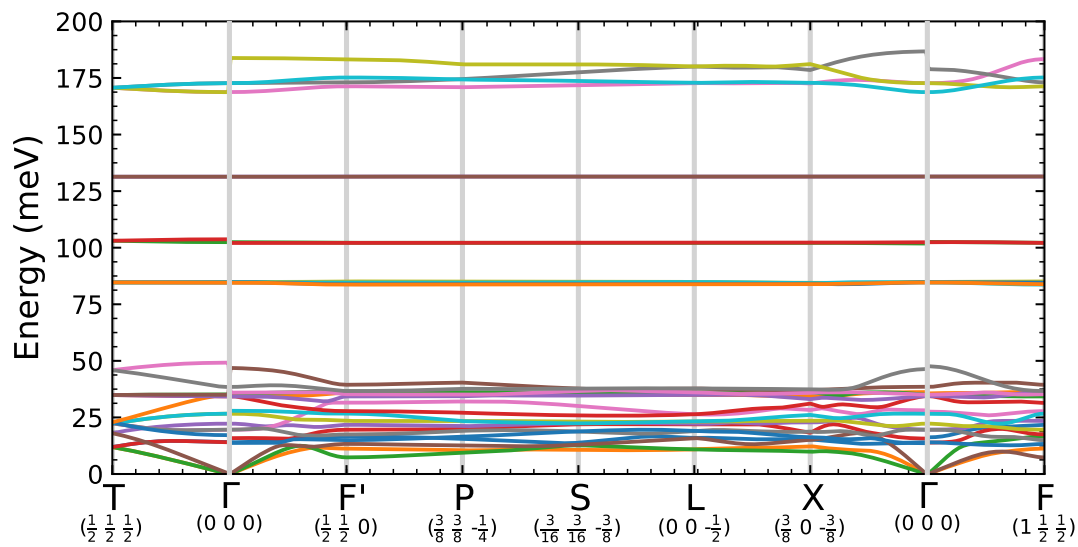


Figure B.3: Phonon dispersion relations in calcite at ambient pressure.

Dolomite

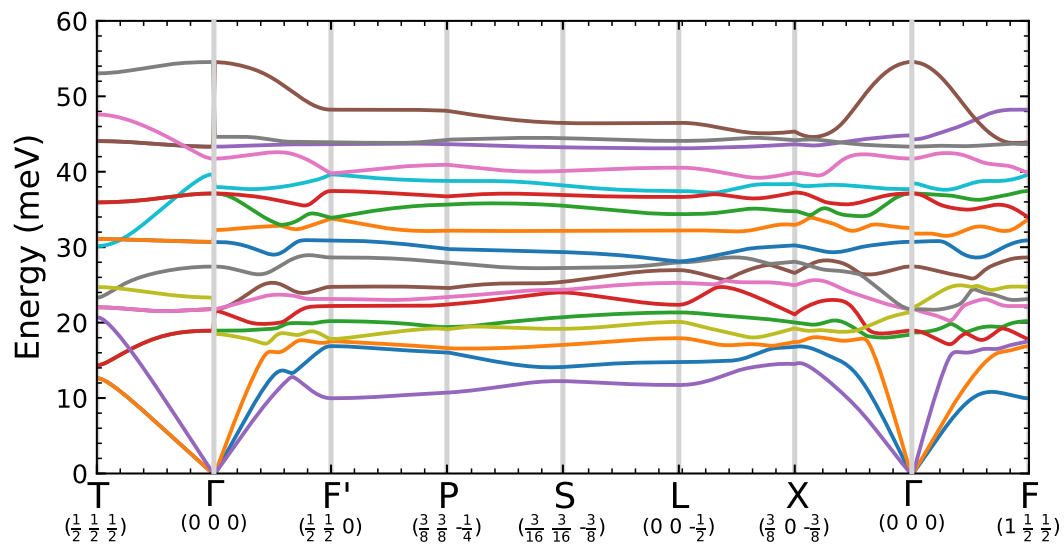


Figure B.4: Low energy phonon dispersion relations in dolomite at ambient pressure.

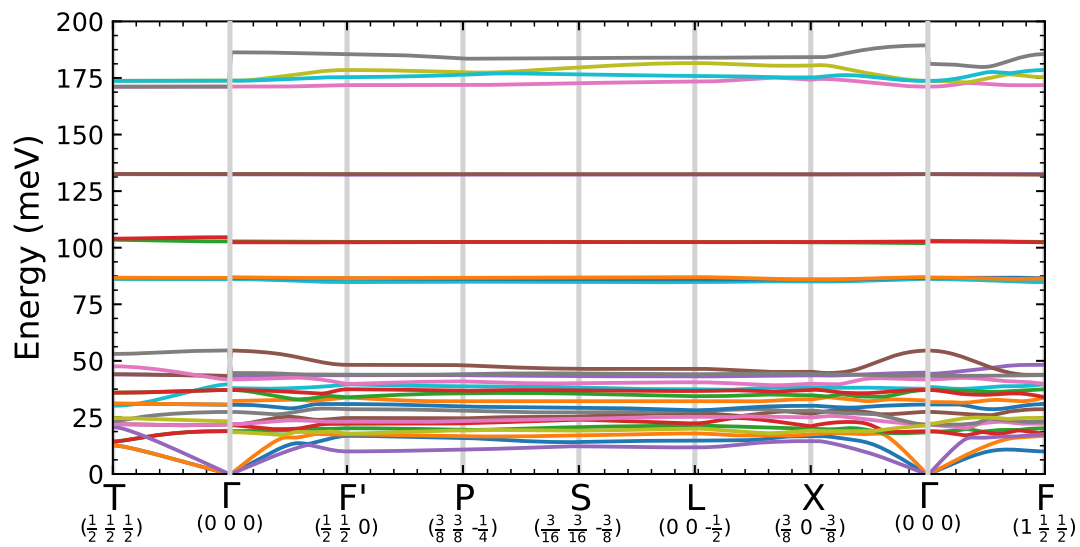


Figure B.5: Phonon dispersion relations in dolomite at ambient pressure.

Magnesite

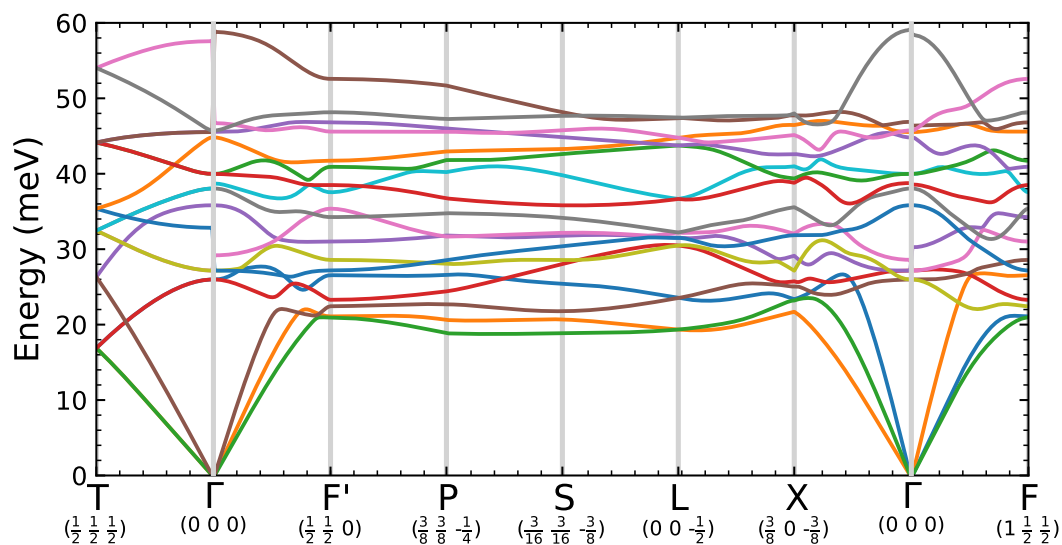


Figure B.6: Low energy phonon dispersion relations in magnesite at ambient pressure.

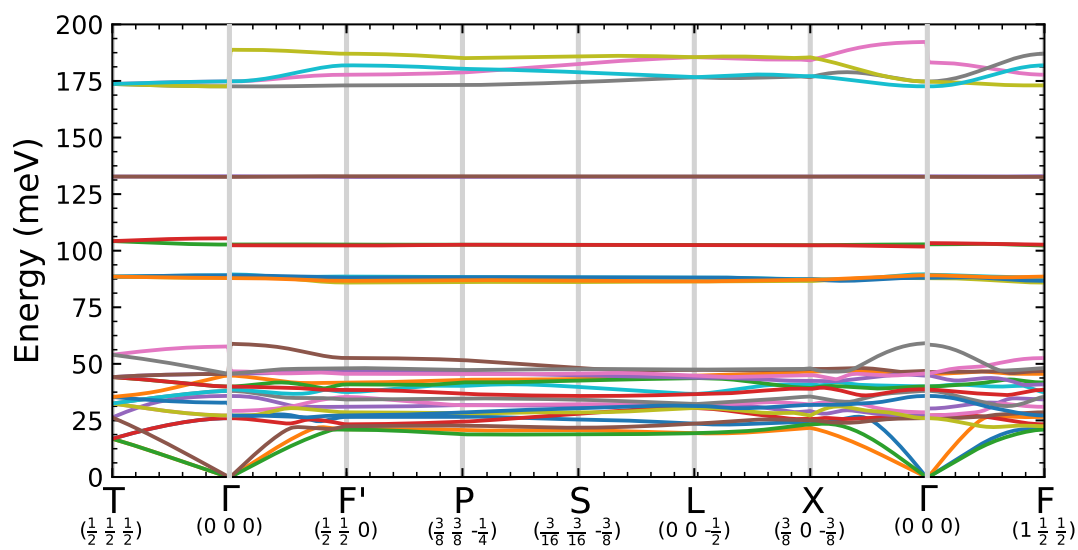


Figure B.7: Phonon dispersion relations in magnesite at ambient pressure.

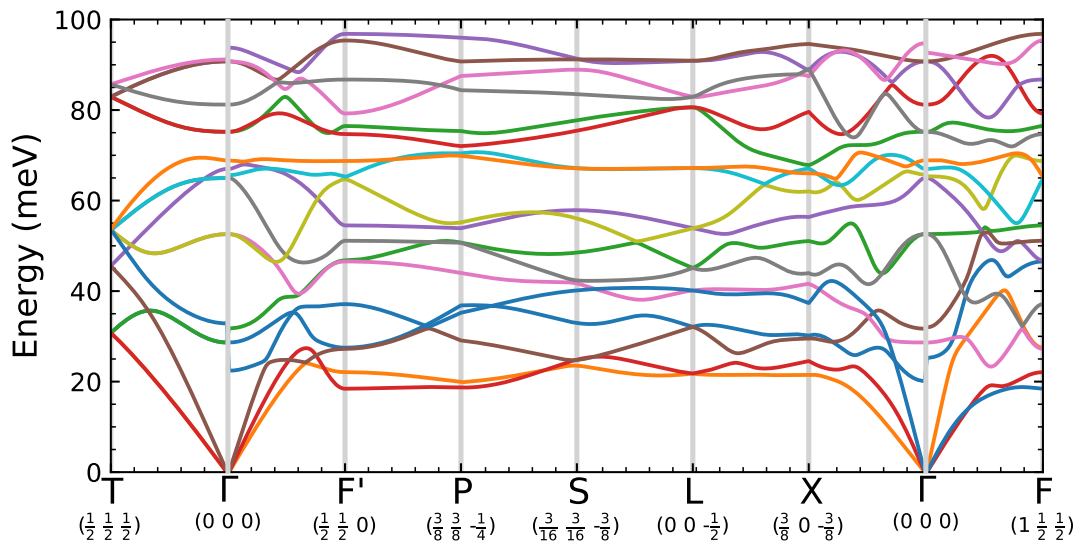


Figure B.8: Low energy phonon dispersion relations in magnesite at 100 GPa.

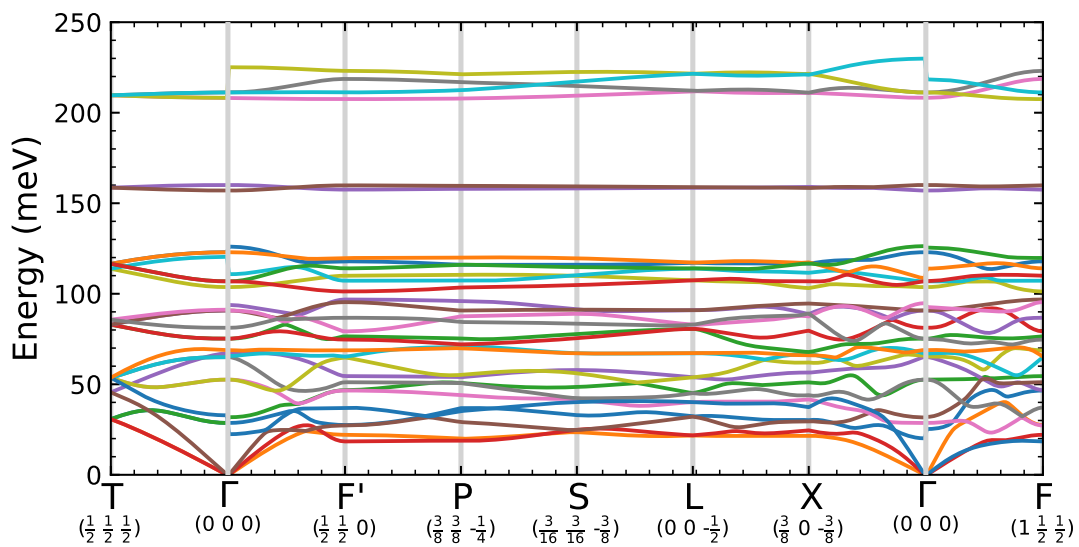


Figure B.9: Phonon dispersion relations in magnesite at 100 GPa.

C Modeling the damping parameter for the high-temperature IXS data

In order to fit the damping parameter measured by IXS and presented in Section 5.6, we have tested few functions that could reproduce the data. First we have fitted a linear function $\gamma_\alpha = a + bT$, to the first N measured points, where we expect only a linear contribution to the phonon width. Then the linear component was subtracted at all temperatures and the residual widths, damping parameter, were fitted with a chosen γ_D function. We have varied the number of points where the linear contribution was expected and tested three different γ_D functions. The results are shown in Table C.1, with representative fits in Figure C.1.

Table C.1: Input and output parameters from the fit of the phonon damping with a chosen function. „N“ denotes the number of point at low temperatures which were chosen to fit the linear contribution. Reorientation time τ was determined at chosen temperatures to test the results. Note that the fitted critical temperature T_C does not correspond to the transition temperature T_V . χ^2 was calculated to quantify the fit reliability.

N	$\tau(300K)$	$\tau(1000K)$	$\tau(1200K)$	T_c	α	$\chi^2(\gamma)$	$\chi^2(\tau)$
$\gamma_D \propto 1/(1 - T/T_0)$							
3	20.7	4.66	0.065	1202.8 (6.3)	-	4.90	31.7
4	24.6	5.45	-0.03	1198.8 (6.4)	-	4.91	25.1
5	29.8	6.50	-0.17	1195.0 (6.5)	-	4.96	19.6
6	36.5	7.84	-0.34	1191.5 (6.6)	-	5.21	18.5
$\gamma_D \propto 1/(1 - T/T_0)^\alpha$							
3	214	4.54	0.467	1491 (102)	4.3 (1.1)	0.258	1.62
4	793	5.51	0.484	1687 (296)	7.1 (3.6)	0.340	2.77
5	13195	7.08	0.506	3019 (4943)	25 (65)	0.608	6.66
$\gamma_D \propto \exp(1/(1 - T/T_0))$							
3	32.1	4.70	0.401	1458 (11)	-	1.90	13.8
4	40.2	5.54	0.395	1445 (13)	-	2.01	10.8
5	51.4	6.64	0.385	1432 (15)	-	2.30	9.93
6	66.3	8.03	0.374	1420 (18)	-	2.86	13.5

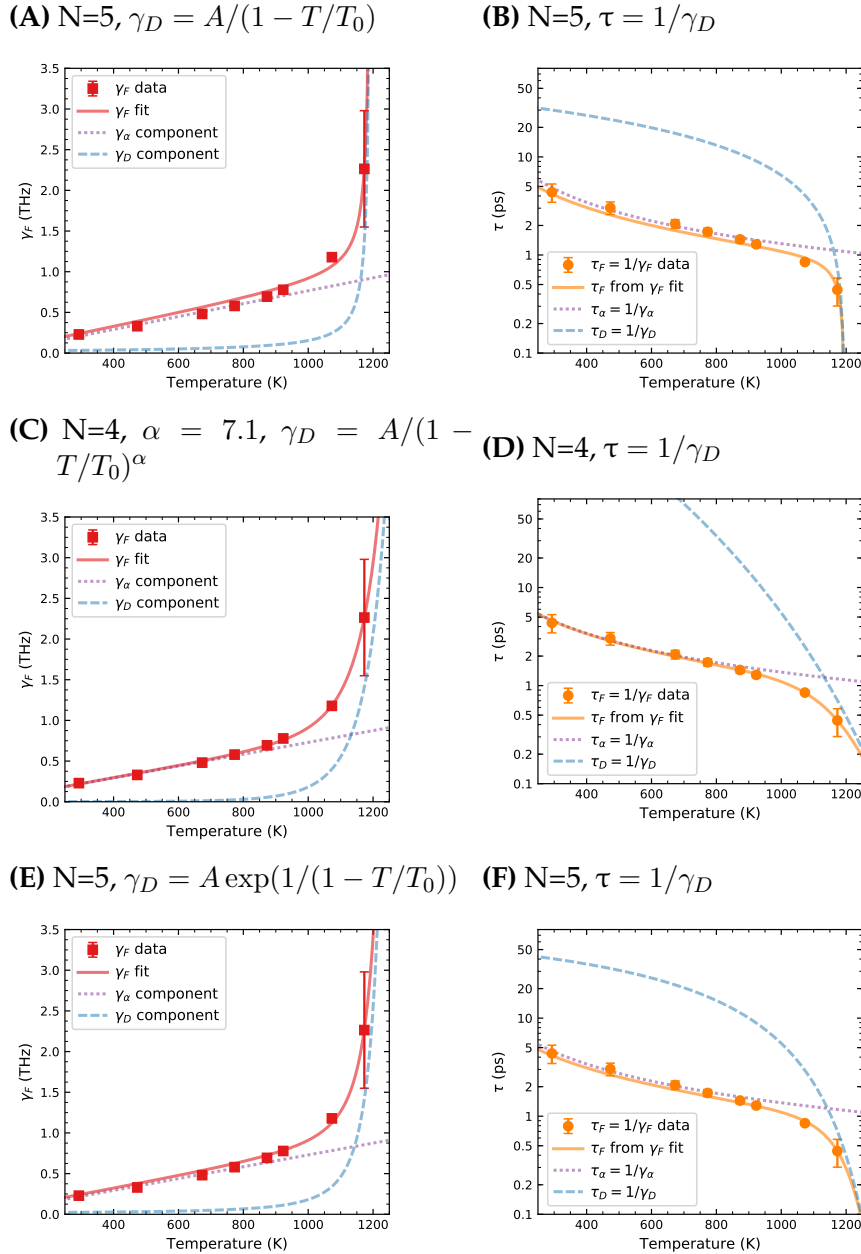


Figure C.1: *F* point phonon (A,C,E) damping coefficient and (B,D,F) lifetime with different functions describing the γ_D component, shown in insets' titles.

Based on the fitted parameters and visual inspection the exponential function $\gamma_D = A \exp(1/(1 - T/T_0))$ with $N=5$ was chosen as the best candidate, as shown in Figures C.1E and C.1F. The reorientation time for the inverse function $\gamma_D = A/(1 - T/T_0)$ were negative at 1200 K. The $\gamma_D = A/(1 - T/T_0)^\alpha$ function with $\alpha = 7.1$ and $N=4$ seems like an equally good candidate, however it involves fitting an additional parameter α . In light of the fact that effectively only three points allow to reliably fit γ_D we chose the exponential function which involves two free parameters. Given the spread of the reorientation time derived from the fits with different models the error for τ is estimated to be around 25%.

Bibliography

- [1] R. M. Hazen and C. M. Schiffries. „Why Deep Carbon?“ In R. Hazen, A. P. Jones, and A. Baross, editors, *Carbon in Earth*, volume 75, chap. 1, pp. 1–6. The Mineralogical Society of America, 2013. doi: 10.2138/rmg.2013.75.1.
- [2] P. B. Kelemen and C. E. Manning. „Reevaluating carbon fluxes in subduction zones, what goes down, mostly comes up“. *Proceedings of the National Academy of Sciences*, vol. 112 (30), pp. E3997–E4006, 2015. doi: 10.1073/pnas.1507889112.
- [3] M. Javoy. „The major volatile elements of the Earth: Their origin, behavior, and fate“. *Geophysical Research Letters*, vol. 24 (2), pp. 177–180, 1997. doi: 10.1029/96GL03931.
- [4] R. W. Luth. „Carbon and carbonates in the mantle“. In Y. Fei, C. M. Bertka, and B. O. Mysen, editors, *Mantle Petrology: Field Observations and High Pressure Experimentation: A Tribute to Francis R. (Joe) Boyd*, chap. 6, pp. 297–316. Geochem. Soc. Spec. Publ., 1999.
- [5] S. S. Santos, M. L. Marcondes, J. F. Justo, and L. V. Assali. „Stability of calcium and magnesium carbonates at Earth’s lower mantle thermodynamic conditions“. *Earth and Planetary Science Letters*, vol. 506, pp. 1 – 7, 2019. doi: <https://doi.org/10.1016/j.epsl.2018.10.030>.
- [6] Z. Zhang, Z. Mao, X. Liu, Y. Zhang, and J. Brodholt. „Stability and Reactions of CaCO₃ Polymorphs in the Earth’s Deep Mantle“. *Journal of Geophysical Research: Solid Earth*, 2018. doi: 10.1029/2018JB015654.
- [7] D. K. Rea and L. J. Ruff. „Composition and mass flux of sediment entering the world’s subduction zones: Implications for global sediment budgets, great earthquakes, and volcanism“. *Earth and Planetary Science Letters*, vol. 140 (1), pp. 1 – 12, 1996. doi: 10.1016/0012-821X(96)00036-2.
- [8] E. Seibold and W. Berger. „Sources and Composition of Marine Sediments“, pp. 45–61. Springer International Publishing, Cham, 2017. doi: 10.1007/978-3-319-51412-3-4.
- [9] R. Hazen, R. Downs, A. Jones, and L. Kah. „Carbon Mineralogy and Crystal Chemistry“. In R. Hazen, A. P. Jones, and A. Baross, editors, *Carbon in Earth*, volume 75, chap. 2, pp. 7–46. The Mineralogical Society of America, 2013. doi: 10.2138/rmg.2013.75.2.
- [10] R. Dasgupta and M. M. Hirschmann. „The deep carbon cycle and melting in Earth’s interior“. *Earth Planet. Sci. Lett.*, vol. 298 (1-2), pp. 1–13, 2010. doi: 10.1016/J.EPSL.2010.06.039.

- [11] Y.-W. Chen, J. Wu, and J. Suppe. „Southward propagation of Nazca subduction along the Andes“. *Nature*, vol. 565 (7740), pp. 441–447, 2019. doi: 10.1038/s41586-018-0860-1.
- [12] A. M. G. Ferreira, M. Faccenda, W. Sturgeon, S.-J. Chang, and L. Schardong. „Ubiquitous lower-mantle anisotropy beneath subduction zones“. *Nat. Geosci.*, vol. 12 (4), pp. 301–306, 2019. doi: 10.1038/s41561-019-0325-7.
- [13] G. E. Shephard, K. J. Matthews, K. Hosseini, and M. Domeier. „On the consistency of seismically imaged lower mantle slabs“. *Sci. Rep.*, vol. 7 (1), pp. 10976, 2017. doi: 10.1038/s41598-017-11039-w.
- [14] „USArray“. URL <http://www.usarray.org/>.
- [15] J. Wu, J. Suppe, R. Lu, and R. Kanda. „Philippine Sea and East Asian plate tectonics since 52 Ma constrained by new subducted slab reconstruction methods“. *J. Geophys. Res. Solid Earth*, vol. 121 (6), pp. 4670–4741, 2016. doi: 10.1002/2016JB012923.
- [16] M. K. Savage. „Seismic anisotropy and mantle deformation: What have we learned from shear wave splitting?“ *Rev. Geophys.*, vol. 37 (1), pp. 65–106, 1999. doi: 10.1029/98RG02075.
- [17] A. Donini, S. Palomares-Ruiz, and J. Salvado. „Neutrino tomography of Earth“. *Nat. Phys.*, vol. 15 (1), pp. 37–40, 2019. doi: 10.1038/s41567-018-0319-1.
- [18] M. Born and K. Huang. „Dynamical Theory of Crystal Lattices“. Oxford University Press, 1954.
- [19] M. Dove. „Introduction to lattice dynamics“. Cambridge University Press, 1993.
- [20] W. Cochran. „The dynamics of atoms in crystals“. Structures and properties of solids. Crane, Russak, 1973.
- [21] G. Srivastava. „The Physics of Phonons“. Taylor & Francis, 1990.
- [22] M. Krisch. „Inelastic x-ray scattering“, 2014. URL http://www.esrf.eu/files/live/sites/www/files/events/conferences/2014/ESRF%20ILL%20Summer%20Programme%202014/Presentations/Inelastic%20X-Ray%20Scattering_Krisch.pdf.
- [23] W. Abney and E. Festing. „On the influence of the atomic grouping in the molecules of organic bodies on their absorption in the infra-red region of the spectrum“. *Philosophical Transactions of the Royal Society of London*, vol. 172, pp. 887–918, 1881. doi: 10.1098/rstl.1881.0020.
- [24] L. Brillouin. „Diffusion de la lumière et des rayons X par un corps transparent homogène - Influence de l’agitation thermique“. *Ann. Phys.*, vol. 9 (17), pp. 88–122, 1922. doi: 10.1051/anphys/192209170088.
- [25] C. V. Raman and K. S. Krishnan. „A new type of secondary radiation“. *Nature*, vol. 121 (3048), pp. 501, 1928.
- [26] P. Olmer. „Dispersion des vitesses des ondes acoustiques dans l’aluminium“. *Acta Crystallographica*, vol. 1 (2), pp. 57–63, 1948. doi: 10.1107/S0365110X48000181.

- [27] B. N. Brockhouse and A. T. Stewart. „Scattering of Neutrons by Phonons in an Aluminum Single Crystal“. *Phys. Rev.*, vol. 100, pp. 756–757, 1955. doi: 10.1103/PhysRev.100.756.
- [28] M. M. Robinson, Y.-X. Yan, E. B. Gamble, L. R. Williams, J. S. Meth, and K. A. Nelson. „Picosecond impulsive stimulated brillouin scattering: Optical excitation of coherent transverse acoustic waves and application to time-domain investigations of structural phase transitions“. *Chemical Physics Letters*, vol. 112 (6), pp. 491 – 496, 1984. doi: 10.1016/0009-2614(84)85764-4.
- [29] B. Dorner, E. Burkel, T. Illini, and J. Peisl. „First measurement of a phonon dispersion curve by inelastic X-ray scattering“. *Zeitschrift für Physik B Condensed Matter*, vol. 69 (2), pp. 179–183, 1987. doi: 10.1007/BF01307274.
- [30] M. Seto, Y. Yoda, S. Kikuta, X. W. Zhang, and M. Ando. „Observation of Nuclear Resonant Scattering Accompanied by Phonon Excitation Using Synchrotron Radiation“. *Phys. Rev. Lett.*, vol. 74, pp. 3828–3831, 1995. doi: 10.1103/PhysRevLett.74.3828.
- [31] A. Baron. „Introduction to High-Resolution Inelastic X-Ray Scattering“, 2018. URL <https://arxiv.org/ftp/arxiv/papers/1504/1504.01098.pdf>.
- [32] „ID28 - inelastic x-ray scattering II“. URL <https://www.esrf.eu/home/UsersAndScience/Experiments/EMD/ID28.html>.
- [33] M. Krisch and F. Sette. „Inelastic X-Ray Scattering from Phonons“. In M. Cardona and R. Merlin, editors, *Light Scattering in Solid IX*, pp. 317–370. Springer Berlin Heidelberg, Berlin, Heidelberg, 2007. doi: 10.1007/978-3-540-34436-0_5.
- [34] A. Bosak, D. Chernyshov, B. Wehinger, B. Winkler, M. L. Tacon, and M. Krisch. „In-between Bragg reflections: thermal diffuse scattering and vibrational spectroscopy with x-rays“. *Journal of Physics D: Applied Physics*, vol. 48 (50), pp. 504003, 2015. URL <http://stacks.iop.org/0022-3727/48/i=50/a=504003>.
- [35] M. Krivoglaz. „Theory of X-Ray and Thermal-Neutron Scattering by Real Crystals“. Plenum Press, 1969.
- [36] „DECTRIS“. URL <https://www.dectris.com/>.
- [37] A. Girard, T. Nguyen-Thanh, S. M. Souliou, M. Stekiel, W. Morgenroth, L. Paolasini, A. Minelli, D. Gambetti, B. Winkler, and A. Bosak. „A new diffractometer for diffuse scattering studies on the ID28 beamline at the ESRF“. *Journal of Synchrotron Radiation*, vol. 26 (1), pp. 272–279, 2019. doi: 10.1107/S1600577518016132.
- [38] „CrysAlisPRO“, 2014. URL <https://www.rigaku.com/en/products/smc/crysalis>.
- [39] M. C. Payne, M. P. Teter, D. C. Allan, T. A. Arias, and J. D. Joannopoulos. „Iterative minimization techniques for ab initio total-energy calculations: molecular dynamics and conjugate gradients“. *Rev. Mod. Phys.*, vol. 64, pp. 1045–1097, 1992. doi: 10.1103/RevModPhys.64.1045.
- [40] P. Hohenberg and W. Kohn. „Inhomogeneous Electron Gas“. *Phys. Rev.*, vol. 136, pp. B864–B871, 1964. doi: 10.1103/PhysRev.136.B864.

- [41] W. Kohn and L. J. Sham. „Self-Consistent Equations Including Exchange and Correlation Effects“. *Phys. Rev.*, vol. 140, pp. A1133–A1138, 1965. doi: 10.1103/PhysRev.140.A1133.
- [42] R. O. Jones. „Density functional theory: Its origins, rise to prominence, and future“. *Rev. Mod. Phys.*, vol. 87, pp. 897–923, 2015. doi: 10.1103/RevModPhys.87.897.
- [43] S. Baroni, S. de Gironcoli, A. Dal Corso, and P. Giannozzi. „Phonons and related crystal properties from density-functional perturbation theory“. *Rev. Mod. Phys.*, vol. 73, pp. 515–562, 2001. doi: 10.1103/RevModPhys.73.515.
- [44] B. Winkler and V. Milman. „Density functional theory based calculations for high pressure research“. *Zeitschrift für Kristallographie – Crystalline Materials*, vol. 229 (2), pp. 112–122, 2014. doi: 10.1515/zkri-2013-1650.
- [45] E. Engel and R. Dreizler. „Density Functional Theory“. Springer-Verlag Berlin Heidelberg, 2011. doi: 10.1007/978-3-642-14090-7.
- [46] L. Landau, L. Pitaevskii, A. Kosevich, and E. Lifshitz. „Theory of Elasticity“, volume 7. Elsevier Science, 2012.
- [47] R. F. S. Hearmon. „The Elastic Constants of Anisotropic Materials“. *Rev. Mod. Phys.*, vol. 18, pp. 409–440, 1946. doi: 10.1103/RevModPhys.18.409.
- [48] W. Voigt. „Lehrbuch der Kristallphysik (mit Ausschluss der Kristalloptik)“. Vieweg+Teubner Verlag, 2014.
- [49] „Form of C_{ij} and S_{ij} matrices in crystallographic systems“. URL https://serc.carleton.edu/NAGTWorkshops/mineralogy/mineral_physics/tensors.html.
- [50] B. Auld. „Acoustic fields and waves in solids“. A Wiley-Interscience publication. Wiley, 1973.
- [51] G. Varughese. „Ultrasonic Investigation of Elastic Properties and Phase Transition in Selected Mixed Sulphate and Sulphamate Crystals“. PhD thesis, Mahatma Gandhi University, 2003.
- [52] R. Dasgupta, M. M. Hirschmann, and A. C. Withers. „Deep global cycling of carbon constrained by the solidus of anhydrous, carbonated eclogite under upper mantle conditions“. *Earth and Planetary Science Letters*, vol. 227 (1–2), pp. 73 – 85, 2004. doi: 10.1016/j.epsl.2004.08.004.
- [53] A. Mattila, T. Pylkkänen, J.-P. Rueff, S. Huotari, G. Vankó, M. Hanfland, M. Lehtinen, and K. Härmäläinen. „Pressure induced magnetic transition in siderite FeCO_3 studied by X-ray emission spectroscopy“. *Journal of Physics: Condensed Matter*, vol. 19 (38), pp. 386206, 2007. doi: 10.1088/0953-8984/19/38/386206.
- [54] B. Lavina, P. Dera, R. T. Downs, V. Prakapenka, M. Rivers, S. Sutton, and M. Nicol. „Siderite at lower mantle conditions and the effects of the pressure-induced spin-pairing transition“. *Geophysical Research Letters*, vol. 36 (23), 2009. doi: 10.1029/2009GL039652.
- [55] S. Fu, J. Yang, and J.-F. Lin. „Abnormal elasticity of single-crystal magnesiosiderite across the spin transition in Earth’s lower mantle“. *Phys. Rev. Lett.*, vol. 118, pp. 036402, 2017. doi: 10.1103/PhysRevLett.118.036402.

- [56] J. Müller, I. Efthimiopoulos, S. Jahn, and M. Koch-Müller. „Effect of temperature on the pressure-induced spin transition in siderite and iron-bearing magnesite: a Raman spectroscopy study“. *European Journal of Mineralogy*, vol. 29 (5), pp. 785–793, 2017. doi: 10.1127/ejm/2017/0029-2645.
- [57] W. Fyfe. „The possibility of d-electron coupling in olivine at high pressures“. *Geochim. Cosmochim. Acta*, vol. 19 (2), pp. 141–143, 1960. doi: 10.1016/0016-7037(60)90046-6.
- [58] M. P. Pasternak, R. D. Taylor, R. Jeanloz, X. Li, J. H. Nguyen, and C. A. McCammon. „High Pressure Collapse of Magnetism in $\text{Fe}_{0.94}\text{O}$: Mössbauer Spectroscopy Beyond 100 GPa“. *Phys. Rev. Lett.*, vol. 79, pp. 5046–5049, 1997. doi: 10.1103/PhysRevLett.79.5046.
- [59] M. P. Pasternak, G. K. Rozenberg, G. Y. Machavariani, O. Naaman, R. D. Taylor, and R. Jeanloz. „Breakdown of the Mott-Hubbard State in Fe_2O_3 : A First-Order Insulator-Metal Transition with Collapse of Magnetism at 50 GPa“. *Phys. Rev. Lett.*, vol. 82, pp. 4663–4666, 1999. doi: 10.1103/PhysRevLett.82.4663.
- [60] J. Badro, G. Fiquet, V. V. Struzhkin, M. Somayazulu, H.-K. Mao, G. Shen, and T. Le Bihan. „Nature of the High-Pressure Transition in Fe_2O_3 Hematite“. *Phys. Rev. Lett.*, vol. 89, pp. 205504, 2002. doi: 10.1103/PhysRevLett.89.205504.
- [61] J.-P. Rueff, C.-C. Kao, V. V. Struzhkin, J. Badro, J. Shu, R. J. Hemley, and H. K. Mao. „Pressure-Induced High-Spin to Low-Spin Transition in FeS Evidenced by X-Ray Emission Spectroscopy“. *Phys. Rev. Lett.*, vol. 82, pp. 3284–3287, 1999. doi: 10.1103/PhysRevLett.82.3284.
- [62] B. Lavina, P. Dera, R. T. Downs, W. Yang, S. Sinogeikin, Y. Meng, G. Shen, and D. Schiferl. „Structure of siderite FeCO_3 to 56 GPa and hysteresis of its spin-pairing transition“. *Phys. Rev. B*, vol. 82, pp. 064110, 2010. doi: 10.1103/PhysRevB.82.064110.
- [63] H. Hsu and S.-C. Huang. „Spin crossover and hyperfine interactions of iron in $(\text{Mg,Fe})\text{CO}_3$ ferromagnesite“. *Physical Review B*, vol. 94 (6), pp. 060404, 2016.
- [64] D. Vasiukov. „Iron electronic states in minerals of the Earth’s mantle“. PhD thesis, Bayreuther Graduiertenschule für Mathematik und Naturwissenschaften (BayNAT), 14 May 2018.
- [65] R. Burns, R. Burns, M. Hochella, R. Liebermann, and A. Putnis. „Mineralogical Applications of Crystal Field Theory“. Cambridge Studies in New Art History and Criticism. Cambridge University Press, 1993.
- [66] P. Gülich and G. H. A. „Spin Crossover in Transition Metal Compounds II“. Topics in Current Chemistry. Springer-Verlag Berlin Heidelberg, 2004. doi: 10.1007/b93641.
- [67] J. Müller, S. Speziale, I. Efthimiopoulos, S. Jahn, and M. Koch-Müller. „Raman spectroscopy of siderite at high pressure: Evidence for a sharp spin transition“. *American Mineralogist*, vol. 101 (12), pp. 2638–2644, 2016. doi: 10.2138/am-2016-5708.
- [68] J. Liu, S. Dorfman, F. Zhu, J. Li, Y. Wang, D. Zhang, Y. Xiao, W. Bi, and E. Alp. „Valence and spin states of iron are invisible in Earth’s lower mantle“. *Nature Communications*, vol. 2018, 2018. doi: 10.1038/s41467-018-03671-5.

- [69] S. Fu, J. Yang, Y. Zhang, T. Okuchi, C. McCammon, H.-I. Kim, S. K. Lee, and J.-F. Lin. „Abnormal Elasticity of Fe-Bearing bridgmanite in the Earth’s Lower Mantle“. *Geophysical Research Letters*, vol. 45 (10), pp. 4725–4732, 2018. doi: 10.1029/2018GL077764.
- [70] D. Antonangeli, J. Siebert, C. M. Aracne, D. L. Farber, A. Bosak, M. Hoesch, M. Krisch, F. J. Ryerson, G. Fiquet, and J. Badro. „Spin crossover in ferropericlase at high pressure: A seismologically transparent transition?“ *Science*, vol. 331 (6013), pp. 64–67, 2011.
- [71] S. S. Lobanov, A. F. Goncharov, and K. D. Litasov. „Optical properties of siderite (FeCO₃) across the spin transition: Crossover to iron-rich carbonates in the lower mantle“. *American Mineralogist*, vol. 100 (5-6), pp. 1059–1064, 2015. doi: 10.2138/am-2015-5053.
- [72] J. Yang, Z. Mao, J. F. Lin, and V. B. Prakapenka. „Single-crystal elasticity of the deep-mantle magnesite at high pressure and temperature“. *Earth Planet. Sci. Lett.*, vol. 392, pp. 292–299, 2014. doi: 10.1016/j.epsl.2014.01.027.
- [73] B. M. French. „Stability relations of siderite (FeCO₃) in the system Fe-C-O“. *American Journal of Science*, vol. 271 (1), pp. 37–78, 1971. doi: 10.2475/ajs.271.1.37.
- [74] V. Cerantola, C. McCammon, I. Kuppenko, I. Kantor, C. Marini, M. Wilke, L. Ismailova, N. Solopova, A. Chumakov, S. Pascarelli, and L. Dubrovinsky. „High-pressure spectroscopic study of siderite (FeCO₃) with a focus on spin crossover“. *American Mineralogist*, vol. 100 (11-12), pp. 2670–2681, 2015. doi: 10.2138/am-2015-5319.
- [75] S. J. Clark, M. D. Segall, C. J. Pickard, P. J. Hasnip, M. I. Probert, K. Refson, and M. C. Payne. „First principles methods using CASTEP“. *Zeitschrift für Kristallographie-Crystalline Materials*, vol. 220 (5/6), pp. 567–570, 2005.
- [76] J. P. Perdew, K. Burke, and M. Ernzerhof. „Generalized Gradient Approximation Made Simple“. *Phys. Rev. Lett.*, vol. 77, pp. 3865–3868, 1996. doi: 10.1103/PhysRevLett.77.3865.
- [77] H. J. Monkhorst and J. D. Pack. „Special points for Brillouin-zone integrations“. *Phys. Rev. B*, vol. 13, pp. 5188–5192, 1976. doi: 10.1103/PhysRevB.13.5188.
- [78] C. Sanchez-Valle, S. Ghosh, and A. D. Rosa. „Sound velocities of ferromagnesian carbonates and the seismic detection of carbonates in eclogites and the mantle“. *Geophysical Research Letters*, vol. 38 (24), pp. L24315, 2011. doi: 10.1029/2011GL049981.
- [79] D. Mainprice, G. Barruol, and W. B. Ismail. „The Seismic Anisotropy of the Earth’s Mantle: from Single Crystal to Polycrystal“, pp. 237–264. American Geophysical Union, 2013. doi: 10.1029/GM117p0237.
- [80] S. Cottaar, T. Heister, I. Rose, and C. Unterborn. „BurnMan: A lower mantle mineral physics toolkit“. *Geochemistry, Geophysics, Geosystems*, vol. 15 (4), pp. 1164–1179, 2014. doi: 10.1002/2013GC005122.
- [81] X. Wang, T. Tsuchiya, and A. Hase. „Computational support for a pyrolitic lower mantle containing ferric iron“. *Nature Geoscience*, vol. 8 (7), pp. 556–559, 2015. doi: 10.1038/ngeo2458.

- [82] L. Stixrude and C. Lithgow-Bertelloni. „Thermodynamics of mantle minerals – I. Physical properties“. *Geophysical Journal International*, vol. 162 (2), pp. 610–632, 2005. doi: 10.1111/j.1365-246X.2005.02642.x.
- [83] P. I. Dorogokupets. „Equation of state of magnesite for the conditions of the Earth’s lower mantle“. *Geochemistry International*, vol. 45 (6), pp. 561–568, 2007. doi: 10.1134/S0016702907060043.
- [84] A. M. Dziewonski and D. L. Anderson. „Preliminary reference Earth model“. *Physics of the earth and planetary interiors*, vol. 25 (4), pp. 297–356, 1981.
- [85] J. Lin, J. Liu, C. Jacobs, and V. Prakapenka. „Vibrational and elastic properties of ferromagnesite across the electronic spin-pairing transition of iron“. *American Mineralogist*, vol. 97 (4), pp. 583–591, 2012. doi: 10.2138/am.2012.3961.
- [86] L. Bayarjargal, C.-J. Fruhner, N. Schrodtr, and B. Winkler. „CaCO₃ phase diagram studied with Raman spectroscopy at pressures up to 50 GPa and high temperatures and DFT modeling“. *Physics of the Earth and Planetary Interiors*, vol. 281, pp. 31 – 45, 2018. doi: 10.1016/j.pepi.2018.05.002.
- [87] M. Isshiki, T. Irifune, K. Hirose, S. Ono, Y. Ohishi, T. Watanuki, E. Nishibori, M. Takata, and M. Sakata. „Stability of magnesite and its high-pressure form in the lowermost mantle“. *Nature*, vol. 427 (6969), pp. 60–63, 2004. doi: 10.1038/nature02181.
- [88] D. M. Hatch and L. Merrill. „Landau description of the calcite-CaCO₃(II) phase transition“. *Phys. Rev. B*, vol. 23, pp. 368–374, 1981. doi: 10.1103/PhysRevB.23.368.
- [89] A. Zucchini, M. Prencipe, D. Belmonte, and P. Comodi. „Ab initio study of the dolomite to dolomite-II high-pressure phase transition“. *European Journal of Mineralogy*, vol. 29 (2), pp. 227–238, 2017. doi: 10.1127/ejm/2017/0029-2608.
- [90] I. Efthimiopoulos, S. Jahn, A. Kuras, U. Schade, and M. Koch-Müller. „Combined high-pressure and high-temperature vibrational studies of dolomite: phase diagram and evidence of a new distorted modification“. *Phys. Chem. Miner.*, vol. 44 (7), pp. 465–476, 2017. doi: 10.1007/s00269-017-0874-5.
- [91] N. A. Solopova, L. Dubrovinsky, A. V. Spivak, Y. A. Litvin, and N. Dubrovinskaja. „Melting and decomposition of MgCO₃ at pressures up to 84 GPa“. *Phys. Chem. Miner.*, vol. 42 (1), pp. 73–81, 2015. doi: 10.1007/s00269-014-0701-1.
- [92] A. R. Oganov, S. Ono, Y. Ma, C. W. Glass, and A. Garcia. „Novel high-pressure structures of MgCO₃, CaCO₃ and CO₂ and their role in Earth’s lower mantle“. *Earth and Planetary Science Letters*, vol. 273 (1-2), pp. 38–47, 2008. doi: 10.1016/J.EPSL.2008.06.005.
- [93] S. S. Lobanov, X. Dong, N. S. Martirosyan, A. I. Samtsevich, V. Stevanovic, P. N. Gavryushkin, K. D. Litasov, E. Greenberg, V. B. Prakapenka, A. R. Oganov, and A. F. Goncharov. „Raman spectroscopy and x-ray diffraction of sp³ CaCO₃ at lower mantle pressures“. *Phys. Rev. B*, vol. 96 (10), pp. 104101, 2017. doi: 10.1103/PhysRevB.96.104101.
- [94] M. Merlini, V. Cerantola, G. D. Gatta, M. Gemmi, M. Hanfland, I. Kupenko, P. Lotti, H. Müller, and L. Zhang. „Dolomite-IV: Candidate structure for a carbonate in

- the Earth's lower mantle". *Am. Mineral.*, vol. 102 (8), pp. 1763–1766, 2017. doi: 10.2138/am-2017-6161.
- [95] E. Boulard, D. Pan, G. Galli, Z. Liu, and W. L. Mao. „Tetrahedrally coordinated carbonates in Earth's lower mantle". *Nat. Commun.*, vol. 6 (1), pp. 6311, 2015. doi: 10.1038/ncomms7311.
- [96] M. Merlini, W. A. Crichton, M. Hanfland, M. Gemmi, H. Müller, I. Kupenko, and L. Dubrovinsky. „Structures of dolomite at ultrahigh pressure and their influence on the deep carbon cycle". *Proceedings of the National Academy of Sciences*, vol. 109 (34), pp. 13509–13514, 2012. doi: 10.1073/pnas.1201336109.
- [97] M. T. Dove, M. E. Hagen, M. J. Harris, B. M. Powell, U. Steigenberger, and B. Winkler. „Anomalous inelastic neutron scattering from calcite". *Journal of Physics: Condensed Matter*, vol. 4 (11), pp. 2761, 1992. doi: 10.1088/0953-8984/4/11/006.
- [98] M. J. Harris, M. T. Dove, I. P. Swainson, and M. E. Hagen. „Anomalous dynamical effects in calcite". *Journal of Physics: Condensed Matter*, vol. 10 (25), pp. L423–L429, 1998. doi: 10.1088/0953-8984/10/25/002.
- [99] W. Heinrich, P. Metz, and W. Bayh. „Experimental investigation of the mechanism of the reaction: 1 tremolite+ 11 dolomite – 8 forsterite+ 13 calcite+ 9 CO₂ + H₂O". *Contributions to Mineralogy and Petrology*, vol. 93 (2), pp. 215–221, 1986.
- [100] S. Chariton. „The elastic properties and the crystal chemistry of carbonates in the deep Earth". PhD thesis, Bayerisches Geoinstitut, 2019.
- [101] Z. Wu and R. E. Cohen. „More accurate generalized gradient approximation for solids". *Phys. Rev. B*, vol. 73, pp. 235116, 2006. doi: 10.1103/PhysRevB.73.235116.
- [102] „ab2tds". URL <http://ftp.esrf.fr/scisoft/AB2TDS/>.
- [103] H. Stanley. „Introduction to Phase Transitions and Critical Phenomena". Oxford University Press, 1971.
- [104] P. Pruzan and D. Gourdain. „Landau-type pressure dependence of the order parameter: application to the ferroelectric-paraelectric pressure-induced transition in KNbO₃". *High Pressure Research*, vol. 24 (1), pp. 129–138, 2004. doi: 10.1080/08957950310001635783a.
- [105] N. Ishizawa, H. Setoguchi, and K. Yanagisawa. „Structural evolution of calcite at high temperatures: Phase V unveiled". *Scientific Reports*, vol. 3, pp. 2832, 2013. doi: 10.1038/srep02832.
- [106] J. Binck, S. Chariton, M. Stekiel, L. Bayarjargal, W. Morgenroth, V. Milman, L. Dubrovinsky, and B. Winkler. „High-pressure, high-temperature phase stability of iron-poor dolomite and the structures of dolomite-IIIc and dolomite-V". *Submitted to Phys. Earth Planet. In.*, 2019.
- [107] R. Minch, D. H. Seoung, L. Ehm, B. Winkler, K. Knorr, L. Peters, L. A. Borkowski, J. B. Parise, Y. Lee, L. Dubrovinsky, and W. Depmeier. „High-pressure behavior of otavite (CdCO₃)". *J. Alloys Compd.*, vol. 508 (2), pp. 251–257, 2010. doi: 10.1016/j.jallcom.2010.08.090.

- [108] V. Cerantola, E. Bykova, I. Kupenko, M. Merlini, L. Ismailova, C. McCammon, M. Bykov, A. I. Chumakov, S. Petitgirard, I. Kantor, V. Svitlyk, J. Jacobs, M. Hanfland, M. Mezouar, C. Prescher, R. Rüffer, V. B. Prakapenka, and L. Dubrovinsky. „Stability of iron-bearing carbonates in the deep Earth’s interior“. *Nat. Commun.*, vol. 8, pp. 15960, 2017. doi: 10.1038/ncomms15960.
- [109] J. Gao, F. Zhu, X.-j. Lai, R. Huang, S. Qin, D.-l. Chen, J. Liu, L.-R. Zheng, and X. Wu. „Compressibility of a natural smithsonite ZnCO_3 up to 50 GPa“. *High Press. Res.*, vol. 34 (1), pp. 89–99, 2014. doi: 10.1080/08957959.2013.868454.
- [110] A. Bouibes and A. Zaoui. „High-pressure polymorphs of ZnCO_3 : Evolutionary crystal structure prediction“. *Sci. Rep.*, vol. 4 (1), pp. 5172, 2015. doi: 10.1038/srep05172.
- [111] R. Dronskowski, S. Kikkawa, and A. Stein. „Handbook of Solid State Chemistry, 6 Volume Set“, volume 2. Wiley, 2017.
- [112] N. Biedermann, S. Speziale, B. Winkler, H. J. Reichmann, M. Koch-Müller, and G. Heide. „High-pressure phase behavior of SrCO_3 : an experimental and computational Raman scattering study“. *Physics and Chemistry of Minerals*, vol. 44 (5), pp. 335–343, 2017. doi: 10.1007/s00269-016-0861-2.
- [113] W. Shi, M. E. Fleet, and S. R. Shieh. „High-pressure phase transitions in Ca-Mn carbonates $(\text{Ca,Mn})\text{CO}_3$ studied by Raman spectroscopy“. *Am. Mineral.*, vol. 97 (5-6), pp. 999–1001, 2012. doi: 10.2138/am.2012.4116.
- [114] M. T. Dove and B. M. Powell. „Neutron diffraction study of the tricritical orientational order/disorder phase transition in calcite at 1260 K“. *Phys. Chem. Miner.*, vol. 16 (5), pp. 503–507, 1989. doi: 10.1007/BF00197019.
- [115] W. Bragg. „The analysis of crystals by the X-ray spectrometer“. *Proceedings of the Royal Society of London A: Mathematical, Physical and Engineering Sciences*, vol. 89 (613), pp. 468–489, 1914. doi: 10.1098/rspa.1914.0015.
- [116] H. E. Boeke. „Die Schmelzerscheinungen und die umkehrbare Umwandlung des Calciumcarbonats“. *Neues Jahrb. Mineral.*, vol. 1, pp. 91–121, 1912.
- [117] P. W. Mirwald. „A differential thermal analysis study of the high-temperature polymorphism of calcite at high pressure“. *Contributions to Mineralogy and Petrology*, vol. 59 (1), pp. 33–40, 1976. doi: 10.1007/BF00375109.
- [118] T. Sakurai and T. Satō. „Temperature Dependence of Vibrational Spectra in Calcite by Means of Emissivity Measurement“. *Phys. Rev. B*, vol. 4, pp. 583–591, 1971. doi: 10.1103/PhysRevB.4.583.
- [119] P. Gillet, C. Biellmann, B. Reynard, and P. McMillan. „Raman spectroscopic studies of carbonates part I: High-pressure and high-temperature behaviour of calcite, magnesite, dolomite and aragonite“. *Physics and Chemistry of Minerals*, vol. 20 (1), pp. 1–18, 1993. doi: 10.1007/BF00202245.
- [120] F. Hippert, E. Geissler, J. Hodeau, E. Lelièvre-Berna, and J. Regnard. „Neutron and X-ray Spectroscopy“. Springer Netherlands, 2006.
- [121] P. G. Klemens. „Anharmonic Decay of Optical Phonons“. *Phys. Rev.*, vol. 148, pp. 845–848, 1966. doi: 10.1103/PhysRev.148.845.

- [122] M. Balkanski, R. F. Wallis, and E. Haro. „Anharmonic effects in light scattering due to optical phonons in silicon“. *Phys. Rev. B*, vol. 28, pp. 1928–1934, 1983. doi: 10.1103/PhysRevB.28.1928.
- [123] G. Lucazeau. „Effect of pressure and temperature on Raman spectra of solids: anharmonicity“. *Journal of Raman Spectroscopy*, vol. 34 (7-8), pp. 478–496, 2003. doi: 10.1002/jrs.1027.
- [124] L. Merrill and W. A. Bassett. „The crystal structure of $\text{CaCO}_3(\text{II})$, a high-pressure metastable phase of calcium carbonate“. *Acta Crystallographica Section B*, vol. 31 (2), pp. 343–349, 1975. doi: 10.1107/S0567740875002774.
- [125] M. Drake and G. Rosenblatt. „Raman spectroscopy in high temperature chemistry“. *NBS Special Publications*, vol. 2, pp. 609–646, 1979. URL http://inis.iaea.org/search/search.aspx?orig_q=RN:12589786.
- [126] R. M. Lynden-Bell and K. H. Michel. „Translation-rotation coupling, phase transitions, and elastic phenomena in orientationally disordered crystals“. *Reviews of Modern Physics*, vol. 66 (3), pp. 721–762, 1994. doi: 10.1103/RevModPhys.66.721.
- [127] J. M. Rowe, J. J. Rush, N. J. Chessler, K. H. Michel, and J. Naudts. „Nature of the Phase Transition in KCN at 168 K“. *Phys. Rev. Lett.*, vol. 40, pp. 455–458, 1978. doi: 10.1103/PhysRevLett.40.455.
- [128] R. Brand, P. Lunkenheimer, and A. Loidl. „Relaxation dynamics in plastic crystals“. *The Journal of Chemical Physics*, vol. 116 (23), pp. 10386–10401, 2002. doi: 10.1063/1.1477186.
- [129] R. M. Lynden-Bell, M. Ferrario, I. R. McDonald, and E. Salje. „A molecular dynamics study of orientational disordering in crystalline sodium nitrate“. *J. Phys. Condens. Matter*, vol. 1 (37), pp. 6523–6542, 1989. doi: 10.1088/0953-8984/1/37/002.
- [130] J. Liu, C.-G. Duan, M. M. Ossowski, W. N. Mei, R. W. Smith, and J. R. Hardy. „Simulation of structural phase transition in NaNO_3 and CaCO_3 “. *Phys. Chem. Miner.*, vol. 28 (8), pp. 586–590, 2001. doi: 10.1007/s002690100191.
- [131] W. W. Schmahl and E. Salje. „X-ray diffraction study of the orientational order/disorder transition in NaNO_3 : Evidence for order parameter coupling“. *Physics and Chemistry of Minerals*, vol. 16 (8), pp. 790–798, 1989. doi: 10.1007/BF00209703.
- [132] S. M. Antao, I. Hassan, W. H. Mulder, and P. L. Lee. „The $R\bar{3}c$ to $R\bar{3}m$ transition in nitrate, NaNO_3 , and implications for calcite, CaCO_3 “. *Phys. Chem. Miner.*, vol. 35 (10), pp. 545–557, 2008. doi: 10.1007/s00269-008-0232-8.
- [133] M. J. Harris. „Diffuse X-ray scattering and the anomalous soft mode in NaNO_3 “. *J. Phys. Condens. Matter*, vol. 5 (32), pp. 5773–5782, 1993. doi: 10.1088/0953-8984/5/32/008.
- [134] M. J. Harris, M. E. Hagen, M. T. Dove, and I. P. Swainson. „Inelastic neutron scattering, phonon softening, and the phase transition in sodium nitrate,“. *J. Phys. Condens. Matter*, vol. 10 (30), pp. 6851–6861, 1998. doi: 10.1088/0953-8984/10/30/022.
- [135] S. Yoshida and Y. Tsujimi. „Brillouin scattering of the order-disorder type phase transition in NaNO_3 “. *Phys. B Condens. Matter*, vol. 219–220, pp. 596–598, 1996. doi: 10.1016/0921-4526(95)00823-3.

- [136] M. Stekiel, T. Nguyen-Thanh, S. Chariton, C. McCammon, A. Bosak, W. Morgenroth, V. Milman, K. Refson, and B. Winkler. „High pressure elasticity of FeCO_3 - MgCO_3 carbonates“. *Physics of the Earth and Planetary Interiors*, vol. 271 (C), pp. 57 – 63, 2017. doi: <https://doi.org/10.1016/j.pepi.2017.08.004>.
- [137] S. Chariton, C. McCammon, D. M. Vasiukov, M. Stekiel, A. Kantor, V. Cerantola, I. Kuppenko, T. Fedotenko, E. Koemets, M. Hanfland, A. I. Chumakov, and D. Leonid. „Seismic detectability of carbonates in the deep Earth: a Nuclear Inelastic Scattering study“. *Accepted in Am. Min.*, 2019.
- [138] M. Stekiel, A. Girard, T. Nguyen-Thanh, A. Bosak, V. Milman, and B. Winkler. „Phonon-driven phase transitions in calcite, dolomite, and magnesite“. *Phys. Rev. B*, vol. 99 (5), pp. 054101, 2019. doi: 10.1103/PhysRevB.99.054101.
- [139] J. Poonoosamy, F. Brandt, M. Stekiel, P. Kegler, M. Klinkenberg, B. Winkler, V. Vinograd, D. Bosbach, and G. Deissmann. „Zr-containing layered double hydroxides: Synthesis, characterization, and evaluation of thermodynamic properties“. *Applied Clay Science*, vol. 151, pp. 54–65, 2018.
- [140] B. Petermüller, C. Neun, M. Stekiel, D. Zimmer, M. Tribus, K. Wurst, B. Winkler, and H. Huppertz. „Synthesis, Crystal Structure, and Compressibilities of $\text{Mn}_{3-x}\text{Ir}_5\text{B}_{2+x}$ ($0 \leq x \leq 0.5$) and Mn_2IrB_2 “. *Chemistry—A European Journal*, vol. 24 (55), pp. 14679–14685, 2018.
- [141] A. Girard, H. Taniguchi, S. Souliou, M. Stekiel, W. Morgenroth, A. Minelli, A. Kuwabara, A. Bosak, and B. Winkler. „Competing structural instabilities in Bi_2SiO_5 “. *Physical Review B*, vol. 98 (13), pp. 134102, 2018.
- [142] A. Girard, M. Stekiel, D. Spahr, W. Morgenroth, B. Wehniger, V. Milman, A. Mirone, A. Minelli, L. Paolasini, A. Bosak, et al. „Structural, elastic and vibrational properties of celestite, SrSO_4 , from synchrotron x-ray diffraction, thermal diffuse scattering and Raman scattering“. *Journal of Physics: Condensed Matter*, vol. 31 (5), pp. 055703, 2018.
- [143] A. Girard, M. Stekiel, W. Morgenroth, H. Taniguchi, V. Milman, A. Bosak, and B. Winkler. „High-pressure compressibility and electronic properties of bismuth silicate Bi_2SiO_5 from synchrotron experiments and first-principles calculations“. *Physical Review B*, vol. 99 (6), pp. 064116, 2019.
- [144] A. Girard, V. Ilakovac, M. Stekiel, W. Morgenroth, H. Berger, T. Yoshikazu, T. Hasegawa, A. Bosak, and B. Winkler. „Soft-phonon driven hexagonal-orthorhombic phase transition in BaVS_3 “. *Phys. Rev. B*, vol. 99, pp. 144104, 2019. doi: 10.1103/PhysRevB.99.144104.

List of Figures

1.1	Estimates of the different carbon fluxes and storages.	2
1.2	Seismic tomography measurements allow to determine the 3D velocity profile of the Nazca plate subducted under South America.	3
2.1	Post-processing applied for the reconstruction of the DS intensity on the (HOL) reciprocal plane in smithsonite.	14
2.2	Independent elastic moduli for different crystal systems.	16
3.1	Iron coordination in siderite and its electronic structure.	20
3.2	Elastic properties of $\text{Mg}_{0.35}\text{Fe}_{0.65}\text{CO}_3$	22
3.3	FeCO_3 single crystals loaded in diamond-anvil cells for high pressure IXS measurements.	25
3.4	Calculated phonon dispersion relations of FeCO_3 at 45 GPa.	26
3.5	IXS spectra of FeCO_3 measured at high pressures	27
3.6	Effective bulk moduli, $C = \rho V_{\text{exp}}^2$, of FeCO_3 measured along selected directions at 55 GPa, compared to the calculated values	27
3.7	Elastic moduli of FeCO_3 at high pressure.	28
3.8	Elastic moduli of MgCO_3 at high pressure	29
3.9	Elastic moduli of $\text{Mg}_{1-x}\text{Fe}_x\text{CO}_3$ calculated in this study and measured by other authors	30
3.10	Heat-maps representing the elasticity of $\text{Mg}_{1-x}\text{Fe}_x\text{CO}_3$ carbonate for all compositions and pressures up to 60 GPa	30
3.11	Mean sound velocities of $\text{Mg}_{1-x}\text{Fe}_x\text{CO}_3$ carbonate with different composition, as well as velocity anisotropies of compressional and shear waves	31
3.12	Sound velocities and shear wave splitting of the lower mantle carbonate $\text{Mg}_{0.85}\text{Fe}_{0.15}\text{CO}_3$	35
4.1	Phase diagrams of calcite, dolomite, and magnesite	38
4.2	Crystal structures of calcite, dolomite, and magnesite	38
4.3	Brillouin zone of rhombohedral carbonates	39
4.4	Calcite and dolomite DAC loadings for high-pressure IXS measurements	41

4.5	Diffuse scattering signal reconstructed on the (H0L) plane of various carbonates measured at the side-station of ID28 and reconstructed from DFT calculations	44
4.6	Measured and calculated IXS spectra of calcite, dolomite, magnesite and smithsonite along the Γ - F branch	45
4.7	Measured and calculated dispersion curves of rhombohedral carbonates	46
4.8	Dispersion of the TA Γ - F branch measured at high-pressures in calcite and dolomite	47
4.9	High-pressure IXS spectra of calcite and dolomite at various pressures	47
4.10	Pressure dependence of the energy of the TA F -point phonon in calcite and dolomite	48
4.11	The eigenvector of the soft F -point phonon in calcite and dolomite together with the atomic displacement due to the corresponding structural transitions, calcite to calcite-II and dolomite to dolomite-II	49
4.12	Calculated phonon dispersion relations for magnesite at ambient pressure and 100 GPa. Eigenvector of the softening F -point phonon at ambient pressure and 100 GPa.	51
4.13	Calculated dispersion relations of the TA phonons for siderite at ambient pressure and 45 GPa in the high-spin and low-spin state of iron	53
4.14	Correlation maps for parameters presented in Table 4.2	54
5.1	Crystal structure of calcite, calcite-IV, and calcite-V	58
5.2	The potential barrier for adapting the alternate orientation for CO_3 groups in calcite and the inverse-site (alternate orientation site) occupation and potential along the O1-O2-O1' arc	59
5.3	Side view cut of the diamond sample chamber just after loading and during heating	60
5.4	Photos of the diamond chamber	61
5.5	Diamond chamber sample environment for the high temperature IXS experiment with calcite, mounted at ID28 of the ESRF	62
5.6	Intensity maps measured at various temperatures reconstructed on high symmetry planes in the reciprocal space	64
5.7	Intensity maps measured at various temperatures by Ishizawa et al. [105]	65
5.8	Intensity along the line between the (-300) and (0012) reflections, measured at various temperatures	66
5.9	IXS spectra measured at the F point at different temperatures, together with the modeled spectrum	67
5.10	Temperature dependence of the soft phonon energy and γ parameter determined by employing different models for measured spectra	68
5.11	Dispersion of the Γ - F branch at high temperatures in calcite	69

5.12	Characteristic of the F -point phonon at high-temperature from the report of Harris et al. [98].	71
5.13	Temperature dependence of the F -point damping coefficient γ_F and lifetime τ_F	73
5.14	Scalar product of the Γ - F acoustic phonons eigenvectors and the vector describing the rotation of the CO_3 groups	75
5.15	Comparison of the reorientation frequency in CaCO_3 and NaNO_3	76
B.1	The first Brillouin zone of calcite, dolomite, and magnesite. The green line shows the path on which phonon dispersion relations were calculated.	87
B.2	Low energy phonon dispersion relations in calcite at ambient pressure.	88
B.3	Phonon dispersion relations in calcite at ambient pressure.	88
B.4	Low energy phonon dispersion relations in dolomite at ambient pressure.	89
B.5	Phonon dispersion relations in dolomite at ambient pressure.	89
B.6	Low energy phonon dispersion relations in magnesite at ambient pressure.	90
B.7	Phonon dispersion relations in magnesite at ambient pressure.	90
B.8	Low energy phonon dispersion relations in magnesite at 100 GPa.	91
B.9	Phonon dispersion relations in magnesite at 100 GPa.	91
C.1	Various fits to the temperature dependence of the F -point damping coefficient γ_F and lifetime τ_F	94
M.2	Places I have visited during the time of my PhD	115

List of Tables

2.1	Experimental methods for investigating lattice dynamics in order of the first reported application.	9
3.1	Details of the diamond-anvil cell loadings prepared for high pressure IXS measurements on FeCO_3	24
4.1	Summary of methods used to investigate lattice dynamics of carbonates .	40
4.2	Selected properties of carbonates and their cations, that could correlate with the transition to the carbonate-II phase	54
B.1	Naming and coordinates of special points in the Brillouin zone of rhombohedral carbonates.	87
C.1	Input and output parameters from the fit of the phonon damping with a chosen function. „N“ denotes the number of point at low temperatures which were chosen to fit the linear contribution. Reorientation time τ was determined at chosen temperatures to test the results. Note that the fitted critical temperature T_C does not correspond to the transition temperature T_V . χ^2 was calculated to quantify the fit reliability.	93

Publications

List of own publications connected to this study:

Chapter 3

- [136] M. Stekiel, T. Nguyen-Thanh, S. Chariton, C. McCammon, A. Bosak, W. Morgenroth, V. Milman, K. Refson and B. Winkler. „High pressure elasticity of FeCO₃–MgCO₃ carbonates“. *Phys. Earth Planet. In.*, **271 (C)**, 57–63, 2017. doi: 10.1016/j.pepi.2017.08.004.
- [137] S. Chariton, C. McCammon, D.M. Vasiukov, M. Stekiel, A. Kantor, V. Cerantola, I. Kупenko, T. Fedotenko, E. Koemets, M. Hanfland, A.I. Chumakov and L. Dubrovinsky. „Seismic detectability of carbonates in the deep Earth: a Nuclear Inelastic Scattering study“. Accepted in *American Mineralogist*, 2019.

Chapter 4

- [138] M. Stekiel, A. Girard, T. Nguyen-Thanh, A. Bosak, V. Milman, and B. Winkler. „Phonon-driven phase transitions in calcite, dolomite, and magnesite“. *Physical Review B*, **99**, 054101, 2019. doi: 10.1103/PhysRevB.99.054101
- [106] J. Binck, S. Chariton, M. Stekiel, L. Bayarjargal, W. Morgenroth, V. Milman, L. Dubrovinsky, and B. Winkler. „High-pressure, high-temperature phase stability of iron-poor dolomite and the structures of dolomite-IIIc and dolomite-V“. Submitted to *Phys. Earth Planet. In.*, 2019.

Chapter 5

M. Stekiel, A. Girard, M. Butiuto, A. Useinov, A. Bosak, and B. Winkler. Phonon coupling to the rotational disorder in calcite at high temperatures. *In preparation*

Other publications:

- [139] J. Poonosamy, F. Brandt, M. Stekiel, P. Kegler, M. Klinkenberg, B. Winkler, V. Vinograd, D. Bosbach, and G. Deissmann. „Zr-containing layered double hydroxides: Synthesis, characterization, and evaluation of thermodynamic properties“, *Appl. Clay Sci.* **151**, 54–65, 2018. doi: 10.1016/j.clay.2017.10.013.
- [140] B. Petermüller, C. Neun, M. Stekiel, D. Zimmer, M. Tribus, K. Wurst, B. Winkler, and H. Huppertz. „Synthesis, Crystal Structure, and Compressibilities of $\text{Mn}_{3-x}\text{Ir}_5\text{B}_{2+x}$ ($0 \leq x \leq 0.5$) and Mn_2IrB_2 “, *Chem. Eur. J.* **24**, 14679–14685, 2018. doi: 10.1002/chem.201803235.
- [141] A. Girard, H. Taniguchi, S.M. Souliou, M. Stekiel, W. Morgenroth, A. Minelli, A. Kuwabara, A. Bosak, and B. Winkler. „Competing structural instabilities in Bi_2SiO_5 “, *Phys. Rev. B* **98**, 134102, 2018. doi: 10.1103/PhysRevB.98.134102.
- [142] A. Girard, M. Stekiel, D. Spahr, W. Morgenroth, B. Wehinger, V. Milman, A. Mirone, A. Minelli, L. Paolasini, A. Bosak, and B. Winkler. „Structural, elastic and vibrational properties of celestite, SrSO_4 , from synchrotron x-ray diffraction, thermal diffuse scattering and Raman scattering“, *J. Phys.: Condens. Matter* **31**, 055703, 2018. doi: 10.1088/1361-648X/aaf0ef.
- [37] A. Girard, T. Nguyen-Thanh, S.M. Souliou, M. Stekiel, W. Morgenroth, L. Paolasini, A. Minelli, D. Gambetti, B. Winkler, A. Bosak. „A new diffractometer for diffuse scattering studies on the ID28 beamline at the ESRF“, *J. Synchrotron Rad.* **26**, 272-279, 2019. doi: 10.1107/S1600577518016132.
- [143] A. Girard, M. Stekiel, W. Morgenroth, H. Taniguchi, V. Milman, A. Bosak, and B. Winkler. „High-pressure compressibility and electronic properties of bismuth silicate Bi_2SiO_5 from synchrotron experiments and first-principles calculations“, *Phys. Rev. B* **99**, 064116, 2019. doi: 10.1103/PhysRevB.99.064116.
- [144] A. Girard, V. Ilakovac, M. Stekiel, W. Morgenroth, H. Berger, T. Yoshikazu, T. Hasegawa, A. Bosak, and B. Winkler. „Soft-phonon driven hexagonal-orthorhombic phase transition in BaVS_3 “. *Phys. Rev. B* **99**, 144104, 2019. doi: 10.1103/PhysRevB.99.144104.

Acknowledgements

I consider this work as a summary of efforts of many people. I am very grateful for the opportunity of having this position as it allowed me to meet a lot of interesting people, make friends all around the world, understand myself, and visit many amazing places. Travelling and discovering is my passion, I'm very happy to have visited all the cities summarized in Figure M.2.

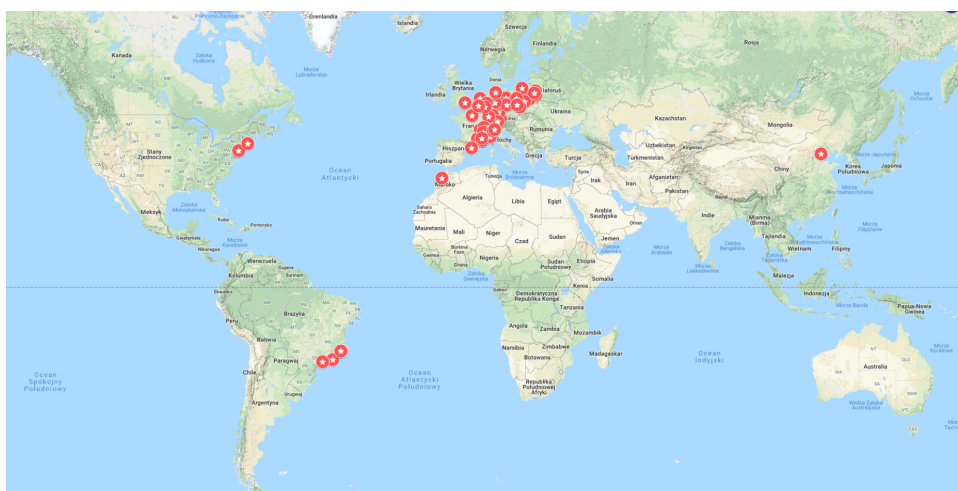


Figure M.2: Places I have visited during the time of my PhD.

I would also like to share some more personal acknowledgments and thank you notes, starting with my supervisors, Björn Winkler and Alexei Bosak. Thank you for your support and eagerness to share your knowledge.

All the current and past members of the Frankfurt group, Wolfgang, Bayra, Eiken, Javier, Nadine, Johannes, Thomas, Rita, Dominik Z., Christopher, Chris, Jannes, Dominik S., Katja, Julia, Boon, David and the workshop, thank you for the hand-on support and sharing the basic skills that allowed me to do my job.

The staff of the ID28 beamline in Grenoble and my friends, Adrien, Michaela, Tra, Arianna, Luigi and Dennis, as well as other ESRF-connected co-workers, Björn, Alessandro and many others.

Many other collaborators who are hard to classify into one of the mentioned groups, members of the CarboPaT group, staff of other beamlines I have done my

measurements at, and all the temporal friends I have met at the conferences. Each one of you gave a minor or major input in this work, I am grateful for you input and sharing your knowledge.

All my friends who helped me dealing with the social aspect of that work, sharing their time and will to help. Thank you Bruno, my best friend from Frankfurt. Thank you my friends from Grenoble, Edoardo, Alessandro, Andrea, Laura, Caterina, Giovanni, Filippo, Susanna, Edoardo, Anna, Emilio, and Jurij. Thank you my friends from Poland, Łukasz, Kinga, Kasjan, Maciek, Ania, Michał, Maciek, Asia, Łukian and the group of beje.

At last, to the people who supported me the most. My parents and family. You were a huge motivation for undertaking this PhD project, you proved to be fantastic supporters too. Thank you for your love and caring. Laura, you are truly my best and beloved friend. You kept me sane during the worst times, I will be always grateful for that, and so many more things.

M. H. H. H.

Curriculum Vitae

Michał Stękiel

PERSONAL INFORMATION

Birth: 19.01.1991 Warsaw, Poland
Mail: michal.stekiel@gmail.com



EDUCATION

- Aug. 2015 - May 2019 *Doctor of Philosophy*
^aGoethe University, Frankfurt, Germany;
^bEuropean Synchrotron Research Facility, Grenoble, France
supervisor: prof. B. Winkler^a, dr A. Bosak^b
Understanding phase transitions in carbonates by investigation of their lattice dynamics
- Aug. 2013 - July 2015 *Master of Science*
Faculty of Physics, University of Warsaw
supervisor: prof. R. Przeniosło
Analysis of crystal and magnetic structure of α -Fe₂O₃ and α -Cr₂O₃
- Oct. 2010 - July 2013 *Bachelor of Science*
Faculty of Physics, University of Warsaw
supervisor: prof. R. Przeniosło
Neutron diffraction of crystals with trigonal symmetry in external magnetic field
- Sep. 2007 - June 2010 *High school*
XIV Liceum Ogólnokształcące, Warsaw, Poland
Mathematics-physics specialization

Sep. 2004 - June 2007

Middle school

Gimnazjum nr 5, Warsaw, Poland

Mathematics-physics specialization

Sep. 1998 - June 2004

Primary school

Szkoła podstawowa nr 202, Warsaw, Poland